WAVE FIELD AUTOFOCUSING AND APPLICATIONS TO MULTIDIMENSIONAL DECONVOLUTION AND IMAGING WITH INTERNAL MULTIPLES

by

Filippo Broggini

A thesis submitted to the Faculty and the Board of Trustees of the Colorado School of Mines in partial fulfillment of the requirements for the degree of Doctor of Philosophy (Geophysics).

Golden, Colorado

Date _____

Signed: _____
Filippo Broggini

Signed: _____
Dr. Roelof K. Snieder
Thesis Advisor

Golden, Colorado

Date _____

Signed: _____
Dr. Terence K. Young
Professor and Head
Department of Geophysics

ABSTRACT

One of the most challenging tasks of exploration geophysics is to build a quantitatively accurate image of the structures inside the Earth from reflection data measured at the Earth's surface. When the subsurface is structurally complicated, accurate images are needed to locate energy sources, such as hydrocarbon reservoirs. Conventional migration algorithms rely on the single-scattering assumption. This restrictive assumption requires that the recorded data do not include waves that have bounced multiple times between layers before reaching the receivers. Standard imaging algorithms incorrectly image the multiple reflections as ghost reflectors and these artifacts can mislead the interpreters in locating potential energy sources. The objective of this thesis is to investigate a new method in reflection seismology for building ghost-free images of the subsurface. The goal is to take advantage of multiply-scattered waves in order to produce more correct images in complicated geological subsurface environments. The method I propose, defined as wave field *autofocusing*, is based on inverse methods originally used in quantum scattering. The first part of this thesis presents the connection between such inverse methods and Green's function retrieval for a one-dimensional medium. I emphasize that the importance of these inversion methods is linked to the retrieval of the wave field propagating in an unknown medium and not to the retrieval of the impedance profile of the same medium. Based on this connection, I extend the method to two-dimensional media and apply it to multidimensional deconvolution to obtain a ghost-free image, hence presenting ad advantage over standard imaging techniques. Then, using the unitarity of the scattering matrix, I show the consistency between the new approach (requiring data on only one side of the medium) and existing methods that require measurement on a closed boundary, such as seismic interferometry. In the last part of this thesis, I test the robustness of the proposed method with respect to errors in the background model used to estimate the first-arriving waves (a required input for the autofocusing process).

TABLE OF CONTENTS

LIST OF FIGURES AND TABLES

ACKNOWLEDGMENTS

Fernando Pessoa, the famous Portugese poet, once wrote that "... Life is what we make of it. Travel is the traveler. What we see isn't what we see but what we are." This quote perfectly describes the five years I spent here at the Center for Wave Phenomena. The Ph.D degree is not just about this thesis manuscript (the final destination), but it is about my growth as a person and scientist (the travel and the traveler). This has been possible only because, quoting Sir Isaac Newton, "I was standing on the shoulders of giants[1]". The tallest (figuratively and literally) of these giants is my advisor and mentor Dr. Roel Snieder. His patience and support helped me overcome difficult research situations and finish this dissertation. I could not have imagined having a better advisor and mentor than Roel. He never failed to entertain me and the other students with his witty jokes. I hope that our scientific relationship will eventually become a friendhsip and last for a long time after I leave Colorado.

In addition, I would like to express my gratitude to Prof. Kees Wapenaar of Delft University of Technology. His insights and suggestions tremendously helped my research achieve new and important results.

I thank the wonderful staff of CWP and the Geophysics Department, Pamela Kraus, Barbara McLenon, Michelle Szobody, Dawn Umpleby, and Shingo Ishida, for their constant help and support. I am particulary grateful to Diane Witters for her help in improving my writing skills, and to John Stockwell for listening to and answering all my "quick questions".

I am grateful to my fellow CWP students for being great companions during all these years. It has been a pleasure and a privilege to discuss my research and ideas with them, and I am confident that they will become my peers and colleagues during my future career.

[1]I waited five years to use this quote!

I thank the members of my thesis committee, Prof. Jeff Andrews-Hanna, Prof. John Berger, Prof. Paul Martin, and Prof. Paul Sava, for their insights and guidance which improved my research and course work. I am especially thankful to Prof. Paul Sava for introducing me to the importance of reproducible research and for reminding me that coding skills are fundamental in our research. I am also grateful to Prof. Paul Martin for his wonderful classes and for showing me that mathematics is a beautiful subject. My sincere thanks also goes to Prof. Terry Young and to the other CWP faculty, Prof. Dave Hale, Prof. Ilya Tsvankin, Prof. Norm Bleistein, Prof. Ken Larner, for their advice and profound scientific knowledge. I am also indebted to Dr. Joost van der Neut, Dr. Jan Thorbecke, and Prof. Evert Slob of Delft University of Technology for working with me on the challenging aspects of my research.

I thank the CWP sponsors for their financial support and their representatives for the constructive feedback I received during meetings and conferences. I feel privileged to have had the chance to share my research with such brilliant scientists.

Last but not least, I thank my family and relatives in Italy, and my friends everywhere in the world. I am especially thankful to my parents, Dante and Giuseppina, for their continuous encouragement and support, and to my friends for being always present when I needed it the most.

To my grandparents.

"*Sometimes life's going to hit you in the head with a brick. Don't lose faith. I'm convinced that the only thing that kept me going was that I loved what I did. You've got to find what you love, and that is as true for work as it is for your lovers.*"

Steve Jobs

CHAPTER 1
GENERAL INTRODUCTION

One of the main goals of exploration geophysics is to retrieve the location and amplitude of the discontinuities between media with different properties inside the subsurface from reflection data measured at the Earth's surface. This is a challenging task because a quantitatively accurate image of the structures inside the Earth is needed to locate energy sources, such as hydrocarbon reservoirs.

Seismic imaging is the branch of geophysics that encompasses all the techniques dedicated to creating representations of the structures inside the Earth. Standard imaging techniques, such as one-way downward continuation (Claerbout, 1985) and reverse-time migration (RTM) (Baysal et al., 1983), rely on the single scattering assumption. This restrictive assumption requires that the recorded data do not include multiply-scattered waves, i.e. waves bouncing multiple times between layers before reaching the receivers at the acquisition surface. The accuracy of seismic imaging greatly depends on the accuracy of the techniques that remove the multiply-scattered waves from the recorded data (Berkhout and Verschuur, 1997; Jakubowicz, 1998; ten Kroode, 2002; Weglein et al., 1997). Especially in structurally complicated media, the current removal techniques do not perform optimally and standard imaging algorithms incorrectly image the multiple reflections as ghost reflectors. These artifacts can mislead the interpreters in locating potential hydrocarbon reservoirs. Additionally, standard imaging techniques depend on the availability of an accurate background velocity model (Etgen et al., 2009). If such a model includes errors in the velocities, the multiple reflections cause stronger artifacts in the final image.

To overcome the influence of the multiply-scattered waves and background velocity model, I propose an alternative approach to create a more accurate image of the subsurface. This new approach is based on the retrieval of the Green's function from data acquired at the

surface. The Green's function $G(\mathbf{x}, \mathbf{x}_\mathrm{I}, t)$, defined as the response recorded at the acquisition surface due to an impulsive source located in the interior of the subsurface (Figure 1.1a), can be used to downward continue the wave field from the recording surface to the interior by virtue of the representation theorem (Aki and Richards, 2002). The Green's function $G(\mathbf{x}, \mathbf{x}_\mathrm{I}, t)$ is composed of downgoing $G^+(\mathbf{x}, \mathbf{x}_\mathrm{I}, t)$ and upgoing $G^-(\mathbf{x}, \mathbf{x}_\mathrm{I}, t)$ components which are coupled by the inhomogeneities of the medium (Wapenaar, 1996); see Figure 1.1b where source-receiver reciprocity has been applied. At a constant depth level, these one-way (downgoing and upgoing) Green's functions are related by

$$G^-(\mathbf{x}_\mathrm{I}, \mathbf{x}_s, t) = \int_{-\infty}^{\infty} \left[R(\mathbf{x}_\mathrm{I}, \mathbf{x}, t) * G^+(\mathbf{x}, \mathbf{x}_s, t)\right]_{z=z_i} \mathrm{d}x, \tag{1.1}$$

where $R(\mathbf{x}_\mathrm{I}, \mathbf{x}, t)$ is the reflection response to downgoing waves at $z = z_i$ (an arbitrary depth level) of a truncated medium below $z = z_i$; $\mathbf{x}_s$ is at $z = 0$; and $\mathbf{x}_r$ is at $z = z_i$. The truncated medium is equal to the true medium (the subsurface) below the depth level $z = z_i$ and is homogeneous above $z = z_i$. The reflectivity $R(\mathbf{x}_\mathrm{I}, \mathbf{x}, t)$ can be resolved from equation 1.1 by multidimensional deconvolution (MDD) (Wapenaar et al., 2011b) which is a technique that provides a numerical solution for integral equations in the form of equation 1.1. An image is built by evaluating $R(\mathbf{x}_\mathrm{I}, \mathbf{x}_\mathrm{I}, t = 0)$ at every image point in the subsurface. Multidimensional deconvolution acknowledges the multidimensional nature of the seismic wave field; hence the internal multiples contribute to the restoration of the amplitudes of the reflectors and do not cause artifacts in the image. I emphasize that the internal multiples are used to construct images with more correct amplitudes, while other methods aim to remove the internal multiples before the imaging step (Berkhout and Verschuur, 1997; Jakubowicz, 1998; ten Kroode, 2002; Weglein et al., 1997). The challenge is now to retrieve the Green's function originating from an image point and then decompose it in its downgoing and upgoing components. If receivers were present at every image point, seismic interferometry (Curtis et al., 2006; Schuster, 2009; Wapenaar et al., 2005; Weaver and Lobkis, 2001) would provide the solution to reconstruct the Green's wave field propagating between two receivers with one

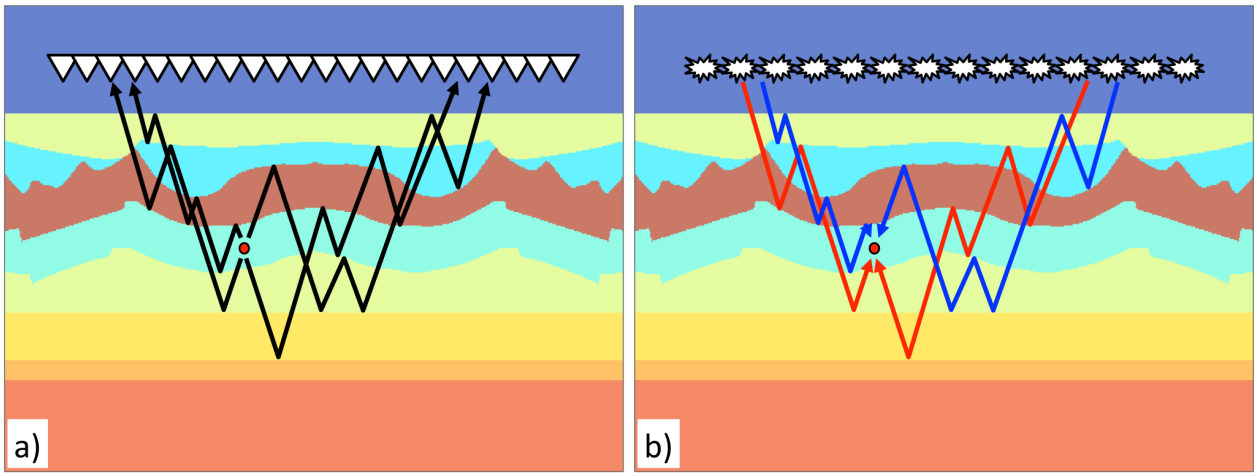

Figure 1.1: a) Total wave field from the imaging point located at $\mathbf{x}_{\mathrm{I}}$ (indicated by the red dot) and recorded at the acquisition surface. b) Decomposed wave fields. The solid blue rays correspond to the downgoing component $G^{+}(\mathbf{x}_{\mathrm{I}}, \mathbf{x}, t)$. The solid red rays correspond to the upgoing component $G^{-}(\mathbf{x}_{\mathrm{I}}, \mathbf{x}, t)$.

of the receivers acting as if it were a source (the image point). Unfortunately, the placement of receivers at every image point is not practically feasible. In this thesis, I introduce a new method that uses 1) reflection data measured at the acquisition surface (including multiply-scattered waves) and 2) a background velocity model (as in standard imaging techniques) to retrieve the total Green's function propagating from an image point to the receivers at the surface and to decompose it in its downgoing and upgoing components. The new approach is based on exact inversion methods for applications in quantum scattering, e.g. Agranovich and Marchenko (1963) and Lamb (1980). In the 1980's, these inversion methods were initially applied to exploration geophysics with the goal of retrieving the impedance profile of the subsurface (Berryman and Greene, 1980; Newton, 1981), but their application was restricted to layered media. I take advantage of the same inverse scattering methods, but with a different goal: Green's function retrieval. This is one of the main insights that contributed to the development of my thesis.

1.1 Thesis overview

The objective of this thesis is to provide solutions for developing a method to create an image of the subsurface which is not affected by artifacts due to the presence of multiply-scattered waves in the data, and to an erroneous background velocity model.

In **Chapter 2**, I investigate the connection between different *scattering principles* in a one-dimensional medium, namely, inverse scattering (Chadan and Sabatier, 1989; Colton and Kress, 1998; Gladwell, 1993), Green's function reconstruction (Larose et al., 2006; Wapenaar et al., 2005), focusing (Rose, 2001, 2002b), imaging (Claerbout, 1985; Sava and Hill, 2009), and the optical theorem (Heisenberg, 1943; Newton, 1976; Rodberg and Thaler, 1967). These subjects, usually studied as independent problems, are defined as scattering principles because they are all related, in different ways, to a scattering process. After recognizing that the equations which rule these principles present common features, I show that the different scattering principles have a common starting point in a representation theorem for the homogeneous Green's function.

The insights obtained from these connections lead to the work presented in **Chapter 3**, where I show that we can make use of inverse methods of quantum scattering (Agranovich and Marchenko, 1963; Lamb, 1980) to retrieve the Green's function originating from a virtual source location inside an unknown one-dimensional acoustic medium. This approach allows one to obtain the same virtual source response as with seismic interferometry (Curtis et al., 2006; Schuster, 2009; Wapenaar et al., 2005; Weaver and Lobkis, 2001), but without the need to have a receiver at the virtual source location. Hence, the new approach goes beyond seismic interferometry.

Chapter 4 is devoted to the generalization to two dimensions of the method discussed in Chapter 3, and to its application to imaging. Following joint work with Prof. Kees Wapenaar from Delft University of Technology (Wapenaar et al., 2012a), I analyze the new method for a layered configuration characterized by variable-density and constant-velocity. In its two-dimensional extension, the proposed method is not fully model-independent because, in

addition to the reflection data measured at the surface, it requires an estimate of the first arriving wave traveling from the virtual source location to receivers located at the acquisition surface (Wapenaar et al., 2013a). Using the method of stationary-phase, I show that the Green's wave field originating from a virtual source location inside an unknown medium is correctly retrieved. Additionally, I decompose the reconstructed Green's function into its downgoing and upgoing components, and use these decomposed wave fields to create a ghost-free image of the subsurface.

Two-sided Green's function representations, such as seismic interferometry, allow the retrieval of the Green's function originating from any location inside the medium. Because these equations require measurements on a closed boundary, they are denoted as *two-sided* integral equations. As previously mentioned, practical constraints prevent the placement of receivers at depth inside the Earth, and hence the acquisition of measurements on a closed boundary. The recently-developed integral equations discussed in Chapters 3 and 4 overcome this problem because they require data on only one side of the medium. I refer to this new approach as *one-sided* Green's function representation. In **Chapter 5**, I show the connection between the one-sided and two-sided Green's function representations, where the unitarity of the scattering matrix plays an important role (Rodberg and Thaler, 1967).

In **Chapter 6**, I apply the new method for data-driven Green's function retrieval to a modified version of the Amoco dataset (Etgen and Regone, 1998). The retrieved downgoing and upgoing components of the Green's functions are used to create different images of the reflectors present in the model. The images created with crosscorrelation and multidimensional deconvolution show an improvement over standard imaging (Claerbout, 1985), and they are free of artifacts due to multiply-scattered waves. Multidimensional deconvolution (MDD) (Wapenaar et al., 2011b) correctly handles the internal multiples and retrieves more accurate amplitudes of the reflectors. Finally, I show that the combination of autofocusing and multidimensional deconvolution produces an artifact-free image when an erroneous velocity model is used to estimate the first-arriving waves (a required input for the autofocusing

process). To conclude, I summarize the thesis and suggest some future work in **Chapter 7**.

Chapters 2-6 of the thesis have been published in, submitted to, or soon will be submitted to peer-reviewed journals:

- **F. Broggini** and R. Snieder, Connection of scattering principles: a visual and mathematical tour, *European Journal of Physics* (2012): 33, 593-613;
- **F. Broggini**, R. Snieder, and Kees Wapenaar, Focusing the wavefield inside an unknown 1D medium - Beyond seismic interferometry, *Geophysics* (2012): 77 (5), A25-A28;
- **F. Broggini**, Kees Wapenaar, Joost van der Neut, and Roel Snieder, Data-driven Green's function Reconstruction and Application to Imaging with Multidimensional Deconvolution, submitted to *Inverse Problems*;
- **F. Broggini**, Kees Wapenaar, Roel Snieder, and Evert Slob, Relationship between one-sided and two-sided Green's function representations, in preparation for *Geophysical Journal International*;
- **F. Broggini**, Roel Snieder, and Kees Wapenaar, Wave field autofocusing and imaging with multidimensional deconvolution: numerical examples for reflection data with internal multiples, in preparation for *Geophysics*.

In addition to the publications included in this thesis, I have also contributed to the following publications:

- Wapenaar K., **F. Broggini**, and R. Snieder, Creating a virtual source inside a medium from reflection data: heuristic derivation and stationary-phase analysis, *Geophysical Journal International* (2012) vol. 190 (2) pp. 1020-1024;
- Wapenaar K., **F. Broggini**, E. Slob, and R. Snieder, Three-Dimensional Single-Sided Marchenko Inverse Scattering, Data-Driven Focusing, Green's Function Retrieval, and their Mutual Relations, *Phys. Rev. Lett.* (2013) vol. 110 (8) pp. 084301;

- Slob E., K. Wapenaar, **F. Broggini**, and R. Snieder, Seismic reflector imaging while eliminating internal multiples using Marchenko-type equations, submitted to *Geophysics*.

CHAPTER 2

CONNECTION OF SCATTERING PRINCIPLES: A VISUAL AND MATHEMATICAL TOUR

Filippo Broggini[1,2] **and Roel Snieder**[1]

Published in *European Journal of Physics* (2012): 33, 593-613

2.1 Abstract

Inverse scattering, Green's function reconstruction, focusing, imaging, and the optical theorem are subjects usually studied as separate problems in different research areas. We show a physical connection between the principles because the equations that rule these *scattering principles* have a similar functional form. We first lead the reader through a visual explanation of the relationship between these principles and then present the mathematics that illustrates the link between the governing equations of these principles. Throughout this work, we describe the importance of the interaction between the causal and anti-causal Green's functions.

2.2 Introduction

Inverse scattering, Green's function reconstruction, focusing, imaging, and the optical theorem are subjects usually studied in different research areas such as seismology (Aki and Richards, 2002), quantum mechanics (Rodberg and Thaler, 1967), optics (Born and Wolf, 1999), non-destructive evaluation of material (Shull, 2002), and medical diagnostics (Epstein, 2003).

Inverse scattering (Chadan and Sabatier, 1989; Colton and Kress, 1998; Gladwell, 1993) is the problem of determining the perturbation of a medium (e.g., of a constant velocity

[1]Center for Wave Phenomena, Colorado School of Mines, Golden, CO 80401, USA
[2]Principal researcher and author

medium) from the field scattered by this perturbation. In other words, one aims to reconstruct the properties of the perturbation (represented by the scatterer in Figure 2.1) from a set of measured data. Inverse scattering takes into account the nonlinearity of the inverse problem, but it also presents some drawbacks: it is improperly posed from the point of view of numerical computations (Dorren et al., 1994), and it requires data recorded at locations usually not accessible due to practical limitations.

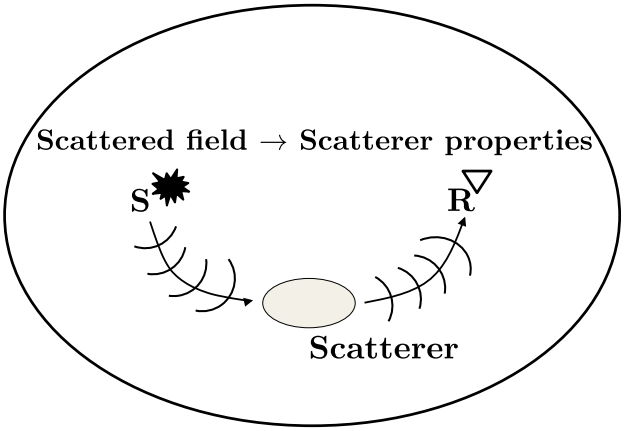

Figure 2.1: Inverse scattering is the problem of determining the perturbation of a medium from its scattered field.

Green's function reconstruction (Larose et al., 2006; Wapenaar et al., 2005) is a technique that allows one to reconstruct the response between two receivers (represented by the two triangles at locations $\mathbf{R}_A$ and $\mathbf{R}_B$ in Figure 2.2) from the cross-correlation of the wavefield measured at these two receivers which are excited by uncorrelated sources surrounding the studied system. In the seismic community, this technique is also known as either the *virtual source method* (Bakulin and Calvert, 2006) or *seismic interferometry* (Curtis et al., 2006; Schuster, 2009). The first term refers to the fact that the new response is reconstructed as if one receiver had recorded the response due to a *virtual* source located at the other receiver position; the second indicates that the recording between the two receivers is reconstructed through the "interference" of all the wavefields recorded at the two receivers excited by the surrounding sources.

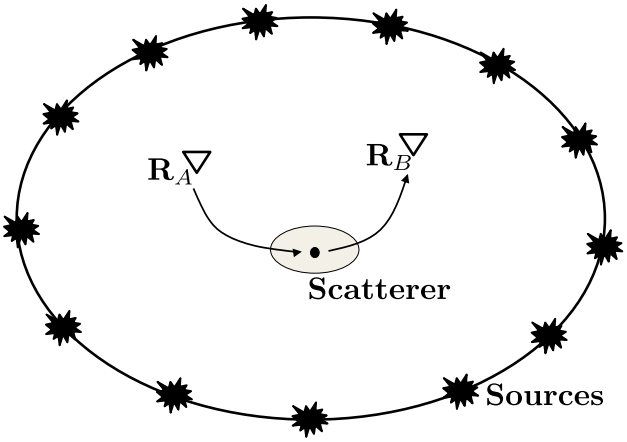

Figure 2.2: Green's function reconstruction allows one to reconstruct the response between two receivers (represented by the two triangles at locations $\mathbf{R}_A$ and $\mathbf{R}_B$).

In this paper, the term *focusing* (Rose, 2001, 2002b) refers to the technique of finding an incident wave that collapses to a spatial delta function $\delta(x - x_0)$ at the location x_0 and at a prescribed time t_0 (i.e., the wavefield is focused at x_0 at t_0) as illustrated in Figure 2.3. In a one-dimensional medium, we deal with a one-sided problem when observations from only one side of the perturbation are available (e.g., due to the practical consideration that we can only record reflected waves); otherwise, we call it a two-sided problem when we have access to both sides of the medium and account for both reflected and transmitted waves.

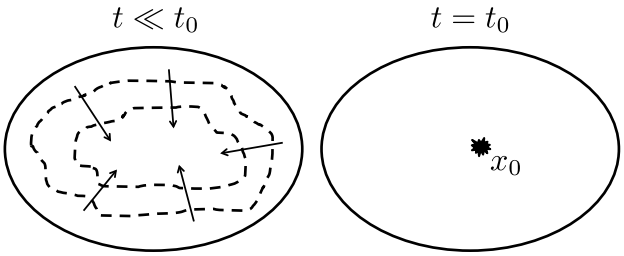

Figure 2.3: Focusing refers to the technique of finding an incident wavefield (represented by the dashed lines) that collapses to a spatial delta function $\delta(x - x_0)$ at the location x_0 and at a prescribed time t_0.

In seismology, the term *imaging* (Claerbout, 1985; Sava and Hill, 2009) refers to techniques that aim to reconstruct an image of the subsurface (Figure 2.4). Geologists and

geophysicists use these images to study the structure of the interior of the Earth and to locate energy resources such as oil and gas. Migration methods (Biondi, 2006; Bleistein et al., 2001) are the most widely used imaging techniques and their accuracy depends on the knowledge of the velocity in the subsurface. Migration methods involve a single scattering assumption (i.e., the Born approximation) because these methods do not take into account the multiple reflections that the waves experience during their propagation inside the Earth; hence the data needs to be preprocessed in a specific way before such methods can be applied.

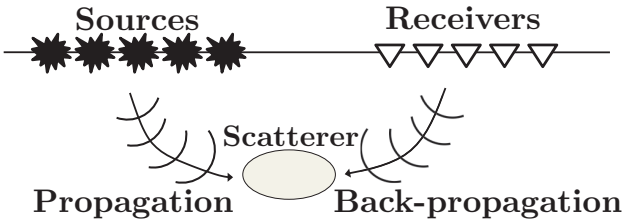

Figure 2.4: Imaging refers to techniques that aim to reconstruct an image of the subsurface.

The ordinary form of the *optical theorem* (Newton, 1976; Rodberg and Thaler, 1967) relates the power extinguished from a plane wave incident on a scatterer to the scattering amplitude in the forward direction of the incident field (Figure 2.5). The scatterer casts a "shadow" in the forward direction where the intensity of the beam is reduced and the forward amplitude is then reduced by the amount of energy carried by the scattered wave. The *generalized optical theorem*, as originally formulated by Heisenberg (1943), is an extension of the previous theorem and it deals with the scattering amplitude in all the directions; hence it contains the ordinary form as a special case. This theorem relates the difference of two scattering amplitudes to an inner product of two other scattering amplitudes. The *generalized optical theorem* provides constraints on the scattering amplitudes in many scattering problems (Carney et al., 2004; Marston, 2001). Since these theorems are an expression of energy conservation, they are valid for any scattering system that does not involve attenuation (i.e., no dissipation of energy).

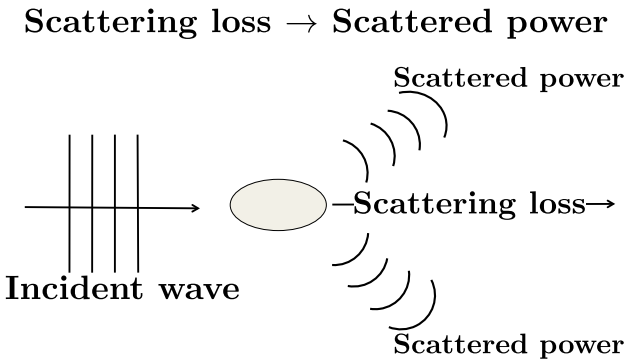

Figure 2.5: The optical theorem relates the power extinguished from a plane wave incident on a scatterer to the scattering amplitude in the forward direction of the incident field.

In this tutorial, we refer to the five subjects discussed above as *scattering principles* because they are all related, in different ways, to a *scattering* process. These principles are usually studied as independent problems but they are related in various ways; hence, understanding their connections offers insight into each of the principles and eventually may lead to new applications. This work is motivated by a simple idea: because the equations that rule these *scattering principles* have a similar functional form (see Table 2.1), there should be a physical connection that could lead to better comprehension of these principles and to possible applications.

Table 2.1: Principles and their governing equations in a simplified form. G is the Green's function, f is the scattering amplitude, and $*$ indicates complex conjugation.

	Principle	**Equation**
1	Inverse Scattering	$u - u^* = \int u^* f$
2	Green's function reconstruction	$G - G^* = \int GG^*$
3	Optical theorem	$f - f^* = \int ff^*$
4	Imaging	$I = \int GG^*$

To investigate these potential connections, we follow two different paths to provide maximum clarity and physical insights. We first show the relationship between different scattering

principles using figures which lead the reader toward a visual understanding of the connections between the principles; then we illustrate and derive the mathematics that shows the link between the governing equations of some of these principles.

2.3 Visual tour

In this section, we lead the reader through a visual understanding of the connections between different scattering principles.

2.3.1 Introduction of time-space diagrams

Before presenting the main results included in this section, we introduce and explain the time-space diagrams that appear in this tutorial. This particular visual representation is borrowed from the seismological community, where these time-space diagrams (called seismic sections) show the motion of the ground recorded by suitable receivers. Wavefields are represented as wiggle traces displaying travel time versus distance. We consider propagation and scattering of waves in a one-dimensional acoustic medium. The field equation governing the wave motion is $Lu(x,t) = 0$, where the acoustic wave equation differential operator is $L \equiv \rho(x)\frac{\partial}{\partial x}(\rho(x)^{-1}\frac{\partial}{\partial x}) - c(x)^{-2}\frac{\partial^2}{\partial t^2}$ (Fokkema and van den Berg, 1993), when the velocity and density of the medium are described by $c(x)$ and $\rho(x)$, respectively. To record the wavefield propagating inside the one-dimensional medium, we imagine to have receivers in the medium itself. As illustrated in Figure 2.6a, the white triangles correspond to receivers placed along the one-dimensional medium. We use a time-space finite difference code with absorbing boundary condition to simulate the propagation of the one-dimensional waves and to produce the numerical examples shown in this section.

We first consider a homogeneous medium with constant velocity $c(x)$ and density $\rho(x)$ shown in Figures 2.6c and 2.6d, respectively. We assume that a source injects energy at $x = 2$ km with the source function described in Figure 2.6b and measure the wavefield at every receiver. In this case,the wavefield is for $t > 0$ given by $u(x,t) = f(t - |x - x_s|/c) + f(t + |x - x_s|/c)$, where $f(t)$ is the source function shown in Figure 2.6b and x_s is the

source position. The wavefield $u(x,t)$ is shown in the time-space diagrams of Figures 2.6e and 2.6f. We show two different visualizations of $u(x,t)$ to facilitate the understanding of our wiggle representation. Figure 2.6g illustrates a close-up of a superposition of the two representations. Each vertical line (called trace) of Figure 2.6f shows the wavefield measured by the receivers illustrated in Figure 2.6a. When the wavefield $u(x,t)$ assumes positive values, the area below $u(x,t)$ is filled to indicate such positive values in contrast to negative ones (as shown with the source function in Figure 2.6b). The advantage of the wiggle traces over the contour plots is that one can better discern details of the waveforms. Causality ensures that the wavefield is non zero only in the region $ct > |x - x_{source}|$ delimited by the first arrival (i.e., the direct waves). If we inject the source function of Figure 2.7a, we obtain the wavefield shown in Figure 2.7b. A similar diagram, for the same velocity and density profile, can be obtained for $t > 0$ if we simultaneously inject the same source at the locations $x = 0$ and $x = 4$ km, as shown in Figure 2.7c. Note that the two incident wavefields, emanating from $x = 0$ and $x = 4$ km, create a focus at $x = 2$ km at $t = 0$ s. The time-space diagram of Figure 2.7c is similar to the light cones described in special relativity (Ohanian and Ruffini, 1994).

This particular time-space diagram is easily created because the medium is homogeneous, but in a more complicated medium this is not trivial. We now consider another one-dimensional medium with velocity $c_s(x)$ and density $\rho_s(x)$ described in Figures 2.7d and 2.7e, respectively. In this case, the medium is not homogeneous; in fact, velocity and density are discontinuous. The incident wavefield emanates from $x = 2$ km, propagates toward the discontinuity in the model, interacts with it, and generates transmitted and reflected scattered waves. The computed wavefield $u(x,t)$ is presented in the time-space diagram of Figure 2.7f and the generation of the transmitted and reflected scattered waves is clearly visible at $x = 3$ km, corresponding to the step in the velocity and density profiles (Figures 2.7d and 2.7e). The heterogeneity has two effects. First, there are now reflected waves within the "light cone", as indicated by the arrow in Figure 2.7f. Second, the arrival time of the

waves is crooked because of the changes in velocity.

2.3.2 Main results

After this brief introduction regarding our visual notation, we can proceed to the core of this section. Figure 2.8 illustrates a scattering experiment in a more complicated one-dimensional acoustic medium where an impulsive source is placed at the position $x = 1.44$ km in the model shown in Figure 2.9. The incident wavefield, a spatial delta function, propagates toward the discontinuities in the model, interacts with them, and generates outgoing scattered waves. The computed wavefield is shown in the time-space diagram of Figure 2.8 and it represents the causal Green's function of the system G^+.

Due to practical limitations, we usually are not able to place a source inside the medium we want to probe, which raises the following question: Is it possible to create the wavefield illustrated in Figure 2.8 without having a real source at the position $x = 1.44$ km? An initial answer to such a question is given by the Green's function reconstruction. This technique allows one to reconstruct the wavefield that propagates between a virtual source and other receivers located inside the medium (Wapenaar et al., 2005). We remind the reader that this technique yields a combination of the causal wavefield and its time-reversed version (i.e., anti-causal), because the reconstructed wavefield is propagating between a receiver and a *virtual source*. Without a real (physical) source, one must have non-zero incident waves to create waves that emanate from a receiver. In the next section we introduce a mathematical argument to explain the interplay of the causal and anti-causal Green's functions. The fundamental steps to reconstruct the Green's function are (Curtis et al., 2006)

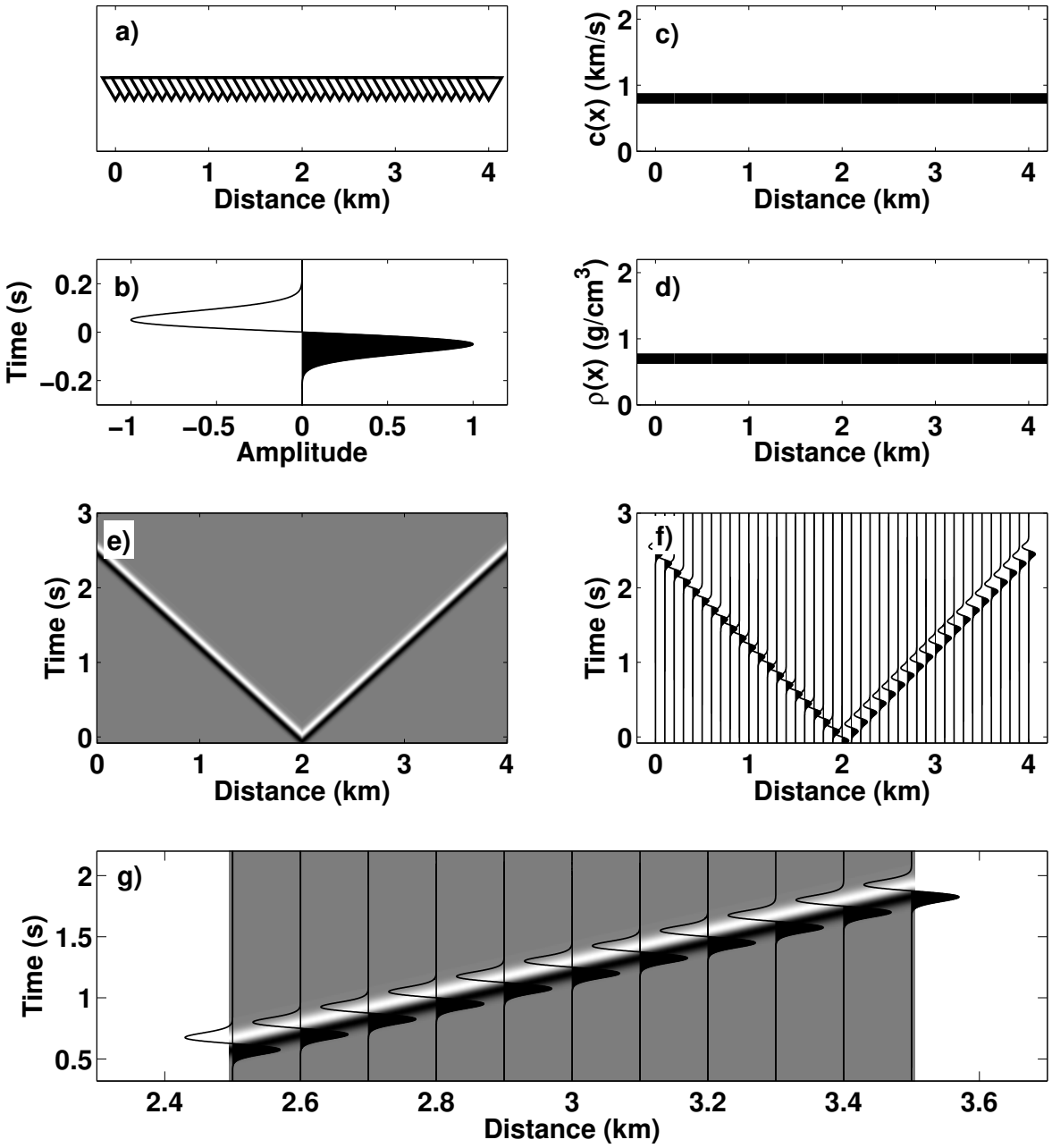

Figure 2.6: (a) The white triangles correspond to receivers in the one-dimensional medium with a spacing of 100 m. (b) Time dependence of the source function. (c) Velocity profile $c(x)$. (d) Density profile $\rho(x)$. (e) and (f) Time-space diagrams for a source at $x = 2$ km. The traces are recorded by the receivers shown in panel (a). (g) Close-up of of the superposition of the time-space diagrams of panels (e) and (f).

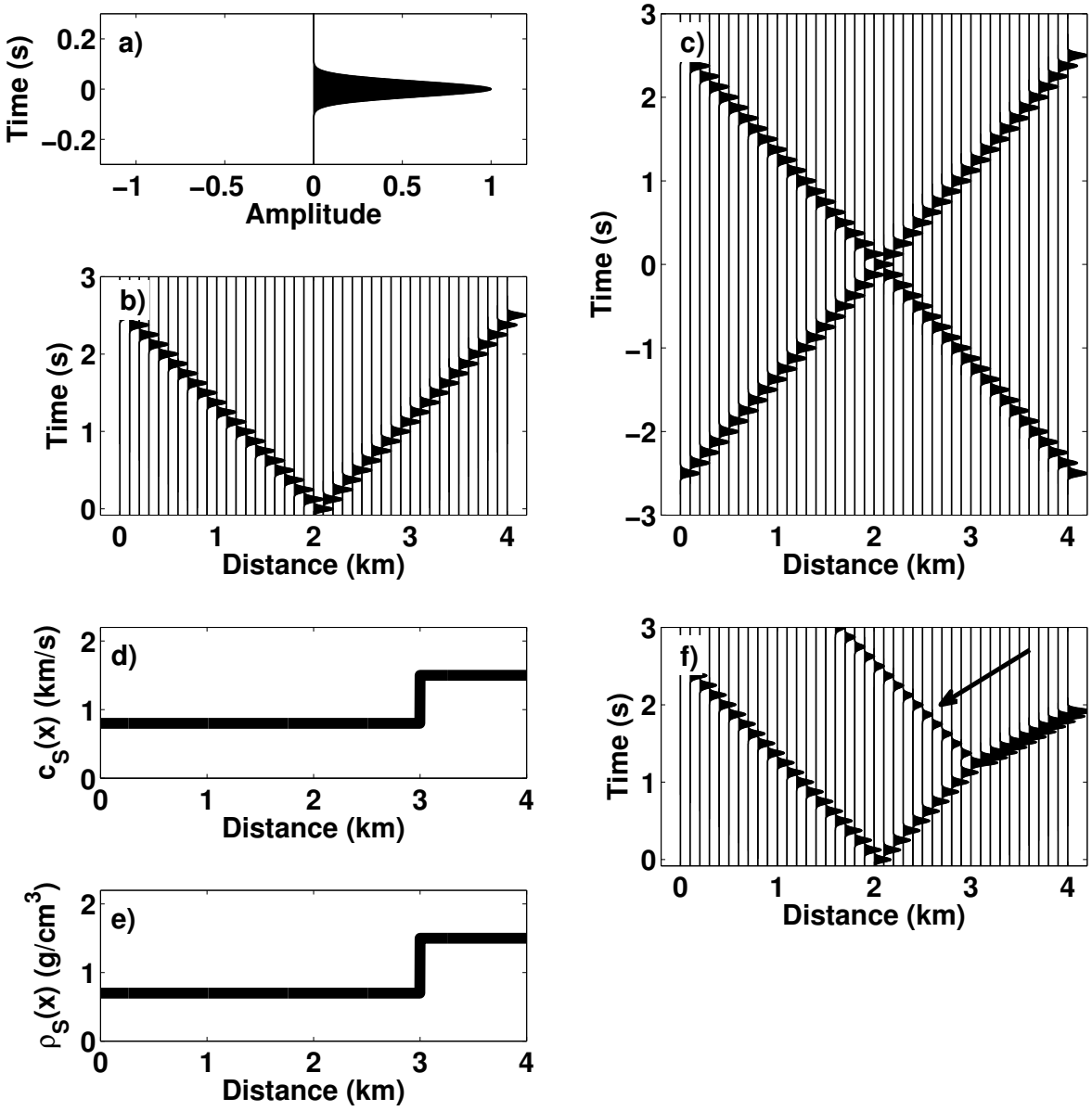

Figure 2.7: (a) Time dependence of the source signal. (b) Time-space diagram for a source at $x = 2$ km. The traces are recorded by the receivers shown in Figure 2.6a. (c) Time-space diagram when two sources are simultaneously present at $x = 0$ and $x = 4$ km. (d) Velocity profile $c_s(x)$. (e) Density profile $\rho_s(x)$. (f) Time-space diagram when a source is present at $x = 2$ km in a medium described by $c_s(x)$ and $\rho_s(x)$. The traces are recorded by the receivers shown in Figure 2.6a. The arrow indicates the reflected waves.

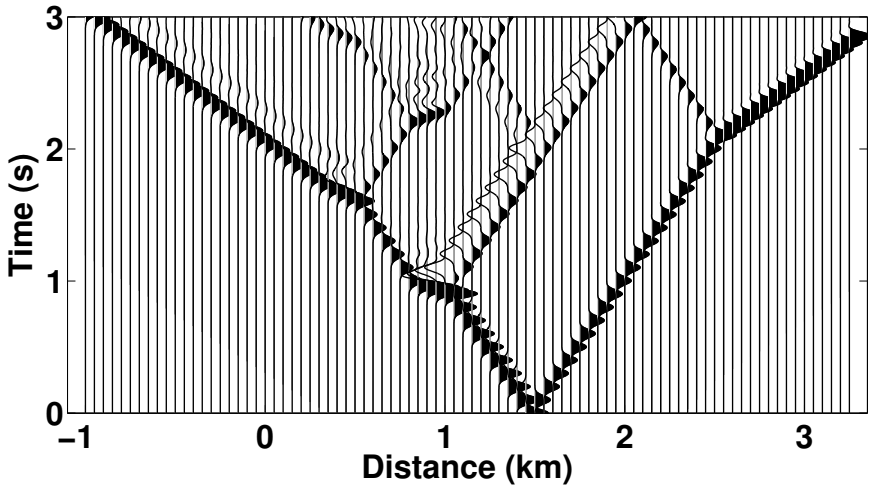

Figure 2.8: Scattering experiment with a source located at $x = 1.44$ km in the model shown in Figure 2.9. The traces are recorded by receivers located in the model with a spacing of 40 m.

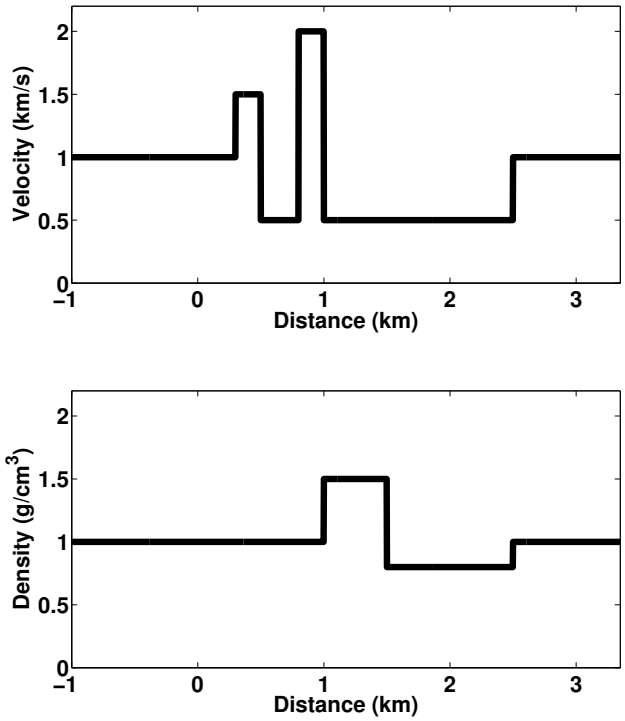

Figure 2.9: Velocity and density profiles of the one-dimensional model. The perturbation in the velocity is located between $x = 0.3 - 2.5$ km and $c_0 = 1$ km/s. The perturbation in the density is located between $x = 1.0 - 2.5$ km and $\rho_0 = 1$ g/cm^3.

1. measure the wavefields $G^+(x, x_{sl}, t)$ and $G^+(x, x_{sr}, t)$ at a receiver located at x (x varies from -1 km to 3 km) excited by impulsive sources located at both sides of the perturbation x_{sl} and x_{sr} (a total of two sources in 1D) as shown in Figure 2.10;

2. cross-correlate $G^+(x, x_{sl}, t)$ with $G^+(x_{vs}, x_{sl}, t)$, where $x_{vs} = 1.44$ km and vs stands for *virtual source*;

3. cross-correlate $G^+(x, x_{sr}, t)$ with $G^+(x_{vs}, x_{sr}, t)$;

4. sum the results computed at the two previous points to obtain $G^+(x, x_{vs}, t)$;

5. repeat this for a receiver located at a different x.

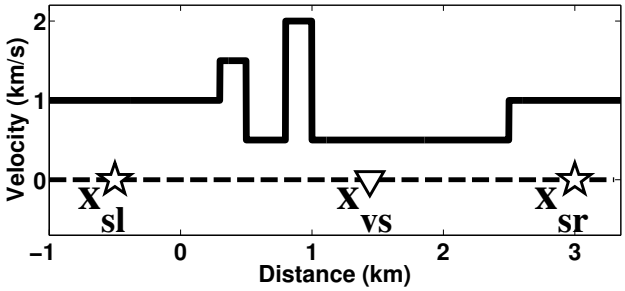

Figure 2.10: Diagram showing the locations of the real and virtual sources for seismic interferometry. x_{sl} and x_{sr} indicate the two real sources. x_{vs} shows the virtual source location.

The causal part of wavefield estimated by the Green's function reconstruction technique is shown in Figure 2.11 and it is consistent with the result of the scattering experiment produced with a real source located at $x = 1.44$ km, shown in Figure 2.8.

We thus have two different ways to reconstruct the same wavefield, but often we are not able to access a certain portion of the medium we want to study and hence we can't place any sources or receivers inside it. We next assume that we only have access to scattering data $R(t)$ measured on the left side of the perturbation, i.e. the reflected impulse response measured at $x = 0$ km due to an impulsive source placed at $x = 0$ km. This further limitation raises another question: Can we reconstruct the same wavefield shown in Figure 2.8 having knowledge only of the scattering data $R(t)$? Since there are neither real sources nor receivers

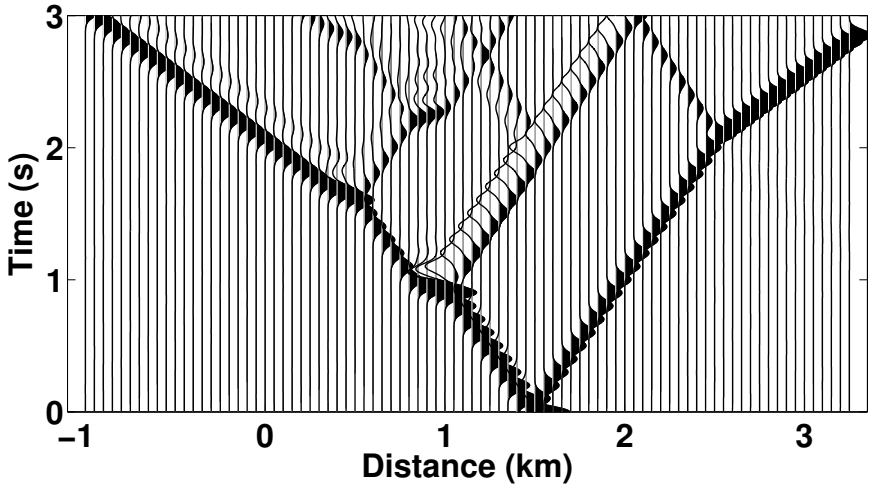

Figure 2.11: Causal part of the wavefield estimated by the Green's function reconstruction technique when the receiver located at $x = 1.44$ km acts as a virtual source.

inside the perturbation, we speculate that the reconstructed wavefield consists of a causal and an anti-causal part, as shown in Figure 2.14.

For this one-dimensional problem, the answer to this question is given by Rose (2001, 2002a). He shows that we need a particular incident wave in order to collapse the wavefield to a spatial delta function at the desired location after it interacts with the medium, and that this incident wave consists of a spatial delta function followed by the solution of the Marchenko equation, as illustrated in Figure 2.12.

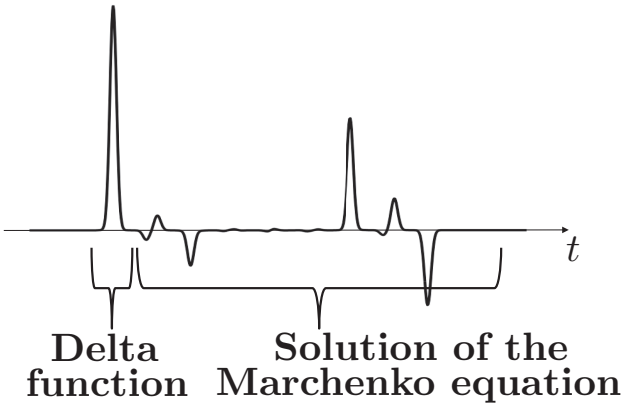

Figure 2.12: Incident wave that focuses at location $x = 1.44$ km and time $t = 0$ s, built using the iterative process discussed by Rose (2001).

The Marchenko integral equation (Chadan and Sabatier, 1989; Lamb, 1980) is a fundamental relation of one-dimensional inverse scattering theory. It is an integral equation that relates the reflected scattering amplitude $R(t)$ to the incident wavefield $u(t, t_f)$ which will create a focus in the interior of the medium and ultimately gives the perturbation of the medium. The one-dimensional form of this equation is

$$0 = R(t + t_f) + u(t, t_f) + \int_{-\infty}^{t_f} R(t + t')u(t', t_f)dt', \tag{2.1}$$

where t_f is a parameter that controls the focusing location. We solve the Marchenko equation, using the iterative process described in detail in Rose (2002a), and construct the particular incident wave that focuses at location $x = 1.44$ km, as shown in Figure 2.8. After seven steps of the iterative process, we inject the incident wave in the model from the left at $x = -1$ km and compute the time-space diagram shown in the top panel of Figure 2.13: it shows the evolution in time of the wavefield when the incident wave is the particular wave computed with the iterative method. The bottom panel of Figure 2.13 shows a cross-section of the wavefield at the focusing time $t = 0$ s: the wavefield vanishes everywhere except at location $x = 1.44$ km; hence the wavefield focuses at this location. Note that the time derivative of the wavefield (i.e., the velocity) is not focused at $x = 1.44$ km, hence also the energy is not focused at this location. We can thus create a focus at a location inside the perturbation without having a source or a receiver at such a location and without any knowledge of the medium properties; we only have access to the reflected impulse response measured on the left side of the perturbation. With an appropriate choice of sources and receivers, this experiment can be done in practice (e.g., in a laboratory).

Figure 2.13 however does not resemble the wavefield shown in Figures 2.8 and 2.11. But if we denote the wavefield in Figure 2.13 as $w(x, t)$ and its time-reversed version as $w(x, -t)$, we obtain the wavefield shown in Figure 2.14 by adding $w(x, t)$ and $w(x, -t)$. With this process, we effectively go from one-sided to two-sided illumination because in Figure 2.14 waves are incident on the scatterer from both sides for $t < 0$ s. Burridge (1980) shows

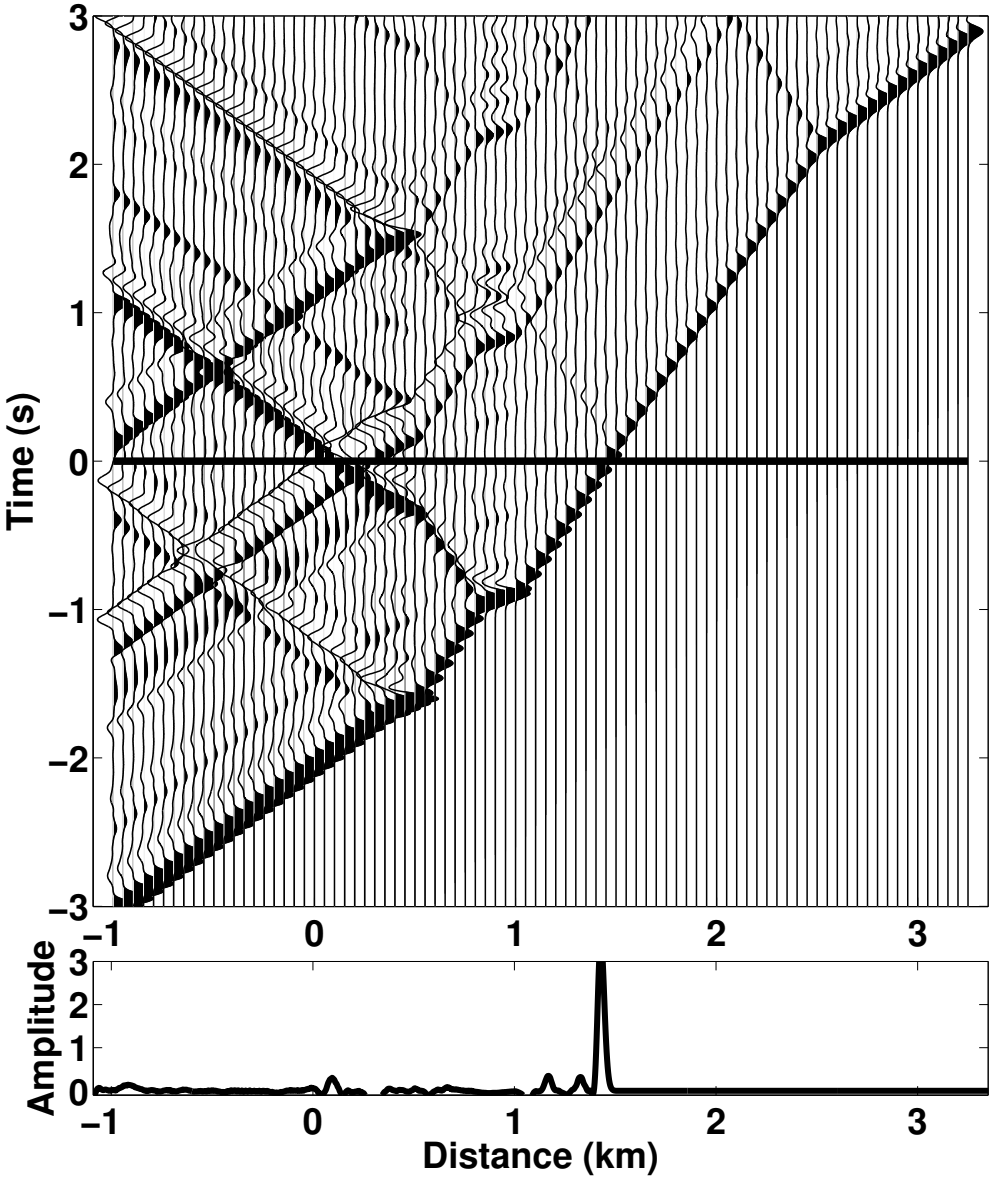

Figure 2.13: Top: After seven steps of the iterative process described in Rose (2002a), we inject at $x = -1$ km the particular incident wave in the model and compute the time-space diagram. Bottom: cross-section of the wavefield at $t = 0$ s.

similar diagrams and explains how to combine such diagrams using causality and symmetry properties. The upper cone in Figure 2.14 corresponds to the causal Green's function and the lower cone represents the anti-causal Green's function; the relationship between the two Green's functions is a key element in the next section, where we introduce the homogeneous Green's function G_h. Note that the wavefield in Figure 2.14, with a focus in the interior of the medium, is based on reflected data recorded at the left side of the heterogeneity only. We did not use a source or receiver in the medium, and did not know the medium. All necessary information is encoded in the reflected waves. Note that a small amount of energy is present outside the two cones. This is due to numerical inaccuracies in our solution of the Marchenko equation.

The extension of the iterative process in two dimensions still needs to be investigated; but we conclude this section with a conjecture illustrated in Figure 2.15. An incident plane wave created by an array of sources is injected in the subsurface where it is distorted due to the variations of the velocity inside the overburden (i.e., the portion of the subsurface that lies above the scatterer). Since we do not know the characteristics of the wavefield when it interacts with the region of the subsurface that includes the scatterer, it is difficult to reconstruct the properties of the scatterer without knowing the medium. Hence, following the insights gained with the one-dimensional problem, we would like to create a special incident wave that, after interacting with the overburden, collapses to a point in the subsurface creating a buried source, as illustrated in Figure 2.16. In this case, assuming that the medium around the scatterer is homogeneous, we would know the shape of the wavefield that probes the scatterer and partially remove the effect of the overburden, which would facilitate accurate imaging of the scatterer.

2.4 Review of scattering theory

We review the theory for the scattering of acoustic waves in a one dimensional medium (also called *line*) with a constant density (in contrast with the previous section where we also considered variable density), where the scatterer is represented by a perturbation of

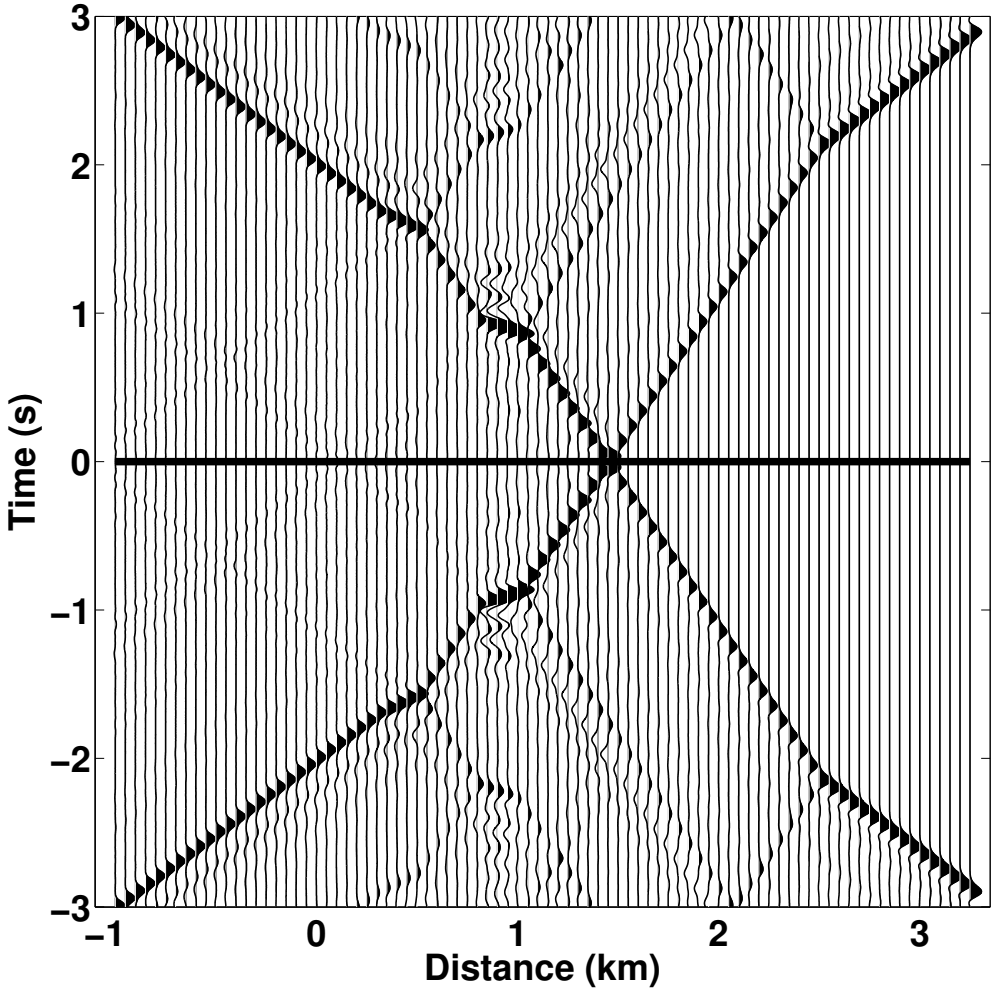

Figure 2.14: Wavefield that focuses at $x = 1.44$ km at $t = 0$ s without a source or a receiver at this location. This wavefield consists of a causal ($t > 0$) and an anti-causal ($t < 0$) part.

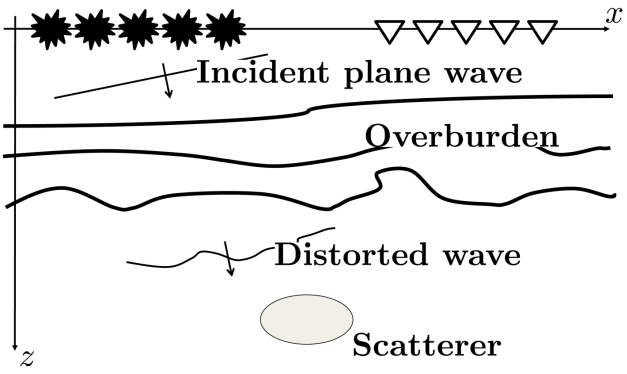

Figure 2.15: An incident plane wave created by an array of sources is injected in the subsurface. This plane wave is distorted due to the variations in the velocity inside the overburden (i.e., the portion of the subsurface that lies above the scatterer). When the wavefield arrives in the region that includes the scatterer, we do not know its shape.

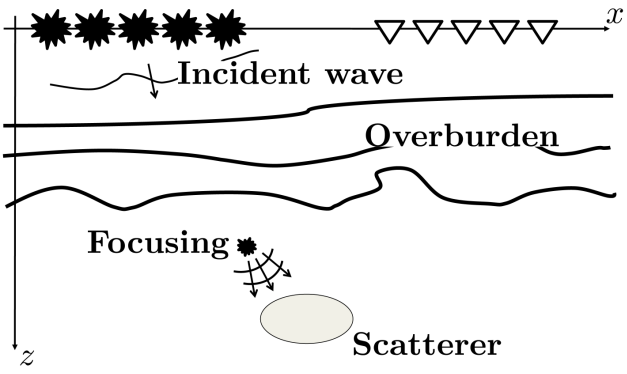

Figure 2.16: Focusing of the wavefield "at depth". A special incident wave, after interacting with the overburden, collapses to a point in the subsurface creating a buried source.

a constant velocity profile. Here, we introduce the wave equation and Green's functions that are used in the next section of the paper. Figure 2.17 shows the geometry of the scattering problem. The perturbation $c_s(x)$ is superposed on a constant velocity profile c_0. The following theory is developed in the frequency domain because it simplifies the derivations (e.g., convolution becomes a multiplication and derivatives become multiplications by $-i\omega$). We also show the time domain version of some of the following equations because they are more intuitive and allow us to understand the important role played by time-reversal. The Fourier transform convention is defined by $\hat{f}(t) = \int f(\omega) \exp(-i\omega t) d\omega$ and $f(\omega) = (2\pi)^{-1} \int \hat{f}(t) \exp(i\omega t) dt$. Throughout this work, when we deal with a one-dimensional problem, the direction of propagation n assumes only two values, 1 and -1, which correspond to waves propagating to the right and to the left (Figure 2.17), respectively.

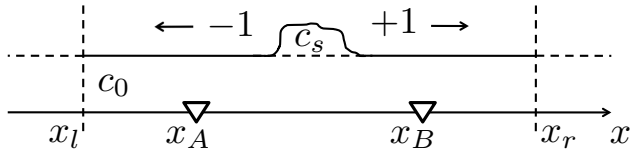

Figure 2.17: Geometry of the problem for the scattering of acoustic waves in a one dimensional medium with constant density. x_A, x_B, x_l and x_r are the coordinates of the receivers (represented by the triangles) and the left and right bounds of our domain, respectively. The perturbation c_s is superposed on a constant velocity profile c_0.

The equation that governs the motion of the waves in an unperturbed medium with constant velocity c_0 is the constant-density acoustic homogeneous wave equation

$$L_0(x, \omega) u_0(n, x, \omega) = 0, \tag{2.2}$$

where u_0 is the displacement wavefield propagating in the n direction and the differential operator is

$$L_0(x, \omega) \equiv \left[\frac{d^2}{dx^2} + \frac{\omega^2}{c_0^2} \right]. \tag{2.3}$$

The solution of equation 2.2 is $u_0(n,x,\omega) = \exp(inx\omega/c_0)$ and its time-domain version is $\hat{u}_0(n,x,t) = \delta(t - nx/c_0)$, which is a delta function that propagates with velocity c_0 in the direction n representing a physical solution to the wave equation. The unperturbed Green's function satisfies the equation

$$L_0(x,\omega)G_0^{\pm}(x,x',\omega) = -\delta(x-x'), \tag{2.4}$$

and, in the acoustic one-dimensional case, its frequency-domain expression is (Snieder, 2004):

$$G_0^{\pm}(x,x',\omega) \equiv \pm\frac{i}{2k}e^{\pm ik|x-x'|}, \tag{2.5}$$

where $k \equiv \omega/c_0$. The $^+$ and $^-$ superscripts of the Green's function represent the causal and anti-causal Green's function with outgoing or ingoing boundary conditions (Oristaglio, 1989), respectively. In the time domain, causality implies that

$$\hat{G}_0^{\pm}(x,x',t) = 0 \qquad \pm t < |x-x'|/c_0. \tag{2.6}$$

Physically, the time-domain Green's function $\hat{G}_0^{+}(x,x',t)$ represents the displacement at a point x at time t due to a point source of unit amplitude applied at x' at time $t = 0$; while $\hat{G}_0^{-}(x,x',t)$ gives the displacement at x that is annihilated by a point source at x' at $t = 0$.

Next, we consider the interaction of the wavefield u_0 with the perturbation $c_s(x)$ (see Figure 2.17). This interaction produces a scattered wavefield $u_{sc}^{\pm}$; hence, the total wavefield can be represented as $u^{\pm} = u_0 + u_{sc}^{\pm}$. The $^+$ and $^-$ superscripts in the total wavefield indicate an initial and a final condition of the wavefield in the time domain, respectively:

$$\hat{u}^{\pm}(n,x,t) \to \hat{u}_0(n,x,t) \qquad t \to \mp\infty. \tag{2.7}$$

Physically, condition 2.7 with plus sign means that the wavefield u^+, at early times, corresponds to the initial wavefield u_0 propagating forward in time in the n direction. The causal and anti-causal wavefields u^+ and u^- are related by time-reversal; in fact, each is the *time-reversed* version of the other $u^-(t) = u^+(-t)$. In the frequency domain, time-reversal corresponds to complex conjugation: $u^-(\omega) = u^{+*}(\omega)$. Their *time-reversal* relationship is better understood by comparing Figures 2.18a and 2.18b, which are valid for the velocity

model of Figure 2.9. Figure 2.18b is obtained by reversing the time axis of Figure 2.18a. We produced both figures using the same velocity model we used in the Visual Tour section of this paper (Figure 2.9). In Figure 2.18a, the initial wavefield is a narrow Gaussian impulse injected at -1.5 km; while, in Figure 2.18b, the initial wavefield corresponds to the wavefield at $t = 6$ s in Figure 2.18a and it coalesces to an outgoing Gaussian pulse.

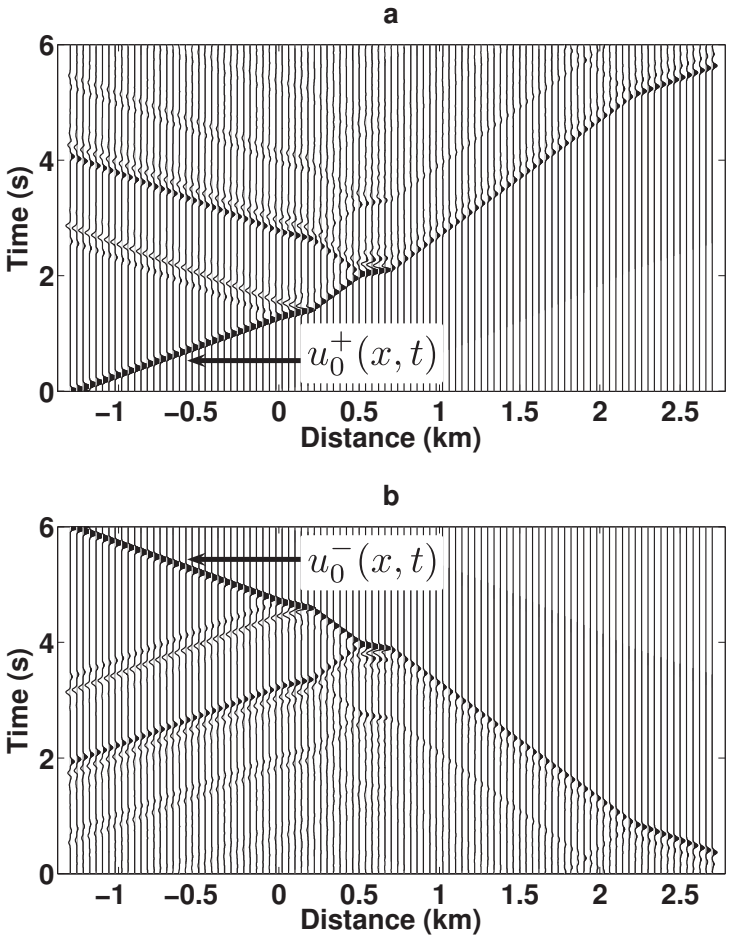

Figure 2.18: Panel **a** shows the causal wavefield u^+ originated by a narrow Gaussian impulse injected at -1.5 km in velocity model of Figure 2.9. Panel **b** shows the anticausal wavefield u^-. Note that each panel is the *time-reversed* version of the other.

The total wavefield $u^{\pm}$ satisfies the wave equation

$$L(x,\omega)u^{\pm}(n,x,\omega) = 0, \tag{2.8}$$

where the differential operator is

$$L(x,\omega) \equiv \left[\frac{d^2}{dx^2} + \frac{\omega^2}{c(x)^2}\right]. \tag{2.9}$$

The velocity varies with position, $c(x) = c_0 + c_s(x)$, as illustrated in Figure 2.17. Using the operator L, we define the perturbed Green's function as the function that satisfies the equation

$$L(x,\omega)G^{\pm}(x,x',\omega) = -\delta(x-x'), \tag{2.10}$$

with the same boundary conditions as equation 2.5. The Green's function $G^{\pm}$ takes into account all the interactions with the perturbation and hence it corresponds to the full wavefield propagating between the points x' and x, due to an impulsive source at x'.

2.5 Mathematical tour

In this part of the paper, we lead the reader through a mathematical tour and show that the different scattering principles have a common starting point, i.e., the following fundamental equation that reveals the connections between them:

$$\begin{aligned} &G^{+}(x_A,x_B) - G^{-}(x_A,x_B) \\ &\quad = \sum_{x'=x_l,x_r} m\left[G^{-}(x',x_A)\frac{d}{dx}G^{+}(x,x_B)|_{x=x'} - G^{+}(x',x_B)\frac{d}{dx}G^{-}(x,x_A)|_{x=x'}\right] \end{aligned} \tag{2.11}$$

with

$$m = \begin{cases} -1 & \text{if } x' = x_l, \\ +1 & \text{if } x' = x_r, \end{cases} \tag{2.12}$$

where x_A, x_B, x_l and x_r (see Figure 2.17) are the coordinates of the receivers located at x_A and x_B and the left and right bounds of our domain, respectively. Equation 2.11 (derived in Appendix A) shows a relation between the causal and anti-causal Green's function and we refer to this expression, throughout the paper, as the representation theorem for the *homogeneous* Green's function $G_h \equiv G^{+} - G^{-}$ (Oristaglio, 1989), which satisfies the wave equation 2.10 when its source term is set equal to zero. G^{+} and G^{-} both satisfy the same wave

equation 2.10 because the differential operator L is invariant to time-reversal ($LG^+ = -\delta$ and $LG^- = -\delta$); hence, their difference is source free: $L(G^+ - G^-) = 0$. The fact that $G^+ - G^-$ satisfies a homogeneous equation suggests that a combination of the causal and anti-causal Green's functions is needed to focus the wavefield at a location where there is no real source. This fact has been illustrated in the previous section when we reconstructed the same wavefield using the Green's function reconstruction technique and the inverse scattering theory (see Figures 2.11 and 2.14); in both cases we obtained a combination of the two Green's functions.

For the remainder of this paper, to be consistent with Budreck and Rose (1990, 1991, 1992), we use the superscripts $^+$ and $^-$ to indicate the causal and anti-causal behavior of wavefields and Green's functions; and, for brevity, we omit the dependence on the angular frequency ω.

2.5.1 Newton-Marchenko equation and generalized optical theorem

In this section, we show that equation 2.11 is the starting point to derive a Newton-Marchenko equation and a generalized optical theorem. In other words, we demonstrate how lines 1 and 3 of Table 2.1 are linked to G_h. The Newton-Marchenko equation differs from the Marchenko equation because it requires both reflected and transmitted waves as data (Newton, 1980). In contrast to the Marchenko equation 3.2, the Newton-Marchenko equation can be extended to two and three dimensions. The Marchenko and the Newton-Marchenko equations deal with the one-sided and two-sided problem, respectively. Following the work of Budreck and Rose (1990, 1991, 1992), we manipulate equation 2.11 and show how to derive the equations that rule these two principles. Before starting with our derivation, we introduce some useful equations:

$$\begin{aligned} u^{\pm}(n,x) &= u_0(n,x) + u^{\pm}_{sc}(n,x) \\ &= u_0(n,x) + \int dx' G^{\pm}_0(x,x') L^{'}(x') u^{\pm}(n,x'), \end{aligned} \tag{2.13}$$

$$u^{\pm}(n,x) = u_0(n,x) + \int dx' G^{\pm}(x,x') L^{'}(x') u_0(n,x'), \tag{2.14}$$

$$G^{\pm}(n,x,x') = G_0^{\pm}(n,x,x') + \int dx'' G^{\pm}(x,x'') L^{'}(x'') G_0^{\pm}(n,x'',x'), \tag{2.15}$$

$$f(n,n') = -\int dx' e^{-nikx'} L^{'}(x') u^{+}(n',x'), \tag{2.16}$$

where $L'(x) \equiv L(x) - L_0(x)$ describes the influence of the scatterer (perturbation). Equations 2.13, 2.14, and 2.15 are three different Lippmann-Schwinger equations (Rodberg and Thaler, 1967); they are a reformulation of the scattering problem using linear integral equations with a Green's function kernel. In particular, equation 2.13 shows that the total field is the summation of the incident wave $u_0(n,x)$ and the scattered wave $u_{sc}^{\pm}(n,x)$. The integral approach is also well suited for the study of inverse problems (Colton and Kress, 1998). Equation 2.16 represents the scattering amplitude (Rodberg and Thaler, 1967) for an incident wave traveling in the n direction and that is scattered in the n' direction. We insert equation 2.15 into 2.11, simplify considering the fact that $x_r > x_A, x'', x_B$ and $x_l < x_A, x'', x_B$, and use expression 2.14:

$$\begin{aligned} &G^{+}(x_A,x_B) - G^{-}(x_B,x_A) \\ &\quad = \left(\frac{i}{2k}\right)\left(-\frac{i}{2k}\right)[\, iku^{-}(+1,x_A)u^{+}(-1,x_B) + iku^{+}(-1,x_B)u^{-}(+1,x_A) \\ &\quad +iku^{-}(-1,x_A)u^{+}(+1,x_B) + iku^{+}(+1,x_B)u^{-}(-1,x_A)\,]\,. \end{aligned} \tag{2.17}$$

In a more compact form this can be written as

$$G^{+}(x_A,x_B) - G^{-}(x_B,x_A) = \left(\frac{i}{2k}\right) \sum_{n=-1,1} u^{-}(n,x_A) u^{+}(-n,x_B). \tag{2.18}$$

Equation 2.18 is the starting point to derive a Newton-Marchenko equation; we show the full derivation in Appendix B and write the final result:

$$u^{+}(+1,x_A) - u^{-}(+1,x_A) = -\frac{i}{2k} \sum_{n=-1,1} u^{-}(n,x_A) f(n,x_B), \quad x_B > x_A, x'', \tag{2.19}$$

and

$$u^{+}(-1,x_A) - u^{-}(-1,x_A) = -\frac{i}{2k}\sum_{n=-1,1} u^{-}(n,x_A) f(n,-x_B), \quad x_B < x_A, x''. \tag{2.20}$$

The system of coupled equations 2.19 and 2.20 is our representation of the one-dimensional Newton-Marchenko equation (Newton, 1980). Recognizing that $u^{-} = u^{*}$, equations 2.19 and 2.20 correspond to line 1 of Table 2.1.

Next, following a similar derivation that led to equations 2.19 and 2.20, we insert expression

$$u^{\pm}(n,x) = u_0(n,x) + \int dx' G_0^{\pm}(x,x') L^{'}(x') u^{\pm}(n,x') \tag{2.21}$$

into equation 2.19, we use the relation $u^{-}(n,x) = u^{+*}(-n,x)$ and equation 2.16, and we finally obtain a generalized optical theorem:

$$f(-n,n) + f^{*}(-n,n) = -\sum_{n'=-1,1} f(-n,n') f^{*}(n,n'), \tag{2.22}$$

where $f(n,n')$ represents the scattering amplitude (Rodberg and Thaler, 1967) and n' assumes the value -1 or $+1$ (see line 3 of Table 2.1). The obtained results are exact because in this one-dimensional framework we do not use any far-field approximations.

2.5.2 Green's function reconstruction and the optical theorem

Starting from the three-dimensional version of equation 2.11, Snieder et al. (2008) showed the connection between the generalized optical theorem and the Green's function reconstruction. Following their three-dimensional formulation, we illustrate the same result for the one-dimensional problem and show the connection between lines 2 and 3 of Table 2.1. In this part of the paper we show the results and leave the mathematical derivation to Appendix C. The expression for the one-dimensional Green's function reconstruction is

$$\frac{i}{2k}\left[\, G^{+}(x_A,x_B) - G^{-}(x_A,x_B) \,\right] = \sum_{x'=x_l,x_r} G^{+}(x_A,x') G^{-}(x_B,x'); \tag{2.23}$$

where the Green's function excited by a point source at x_B recorded at x_A can be separated in an incident and a scattered part and is given by

$$G^{\pm}(x_A, x_B) = \underbrace{\mp\frac{i}{2k}e^{\pm ik|x_B - x_A|}}_{direct} \underbrace{\mp\frac{i}{2k}e^{\pm ik|x_B|}f(n,n')e^{ik|x_A|}}_{scattered}. \tag{2.24}$$

Unlike the three-dimensional case, we obtain two different results depending on the configuration of the system. In the first case (Figure 2.19a), the ordinary optical theorem is derived:

$$f(n,n) + f^*(n,n) = -\sum_{n'=-1,1} |f(n,n')|^2; \tag{2.25}$$

in the second case (Figure 2.19b), we obtain a generalized optical theorem

$$f(-n,n) + f^*(-n,n) = -\sum_{n'=-1,1} f(-n,n')f^*(n,n'), \tag{2.26}$$

where n assumes the value -1 or $+1$.

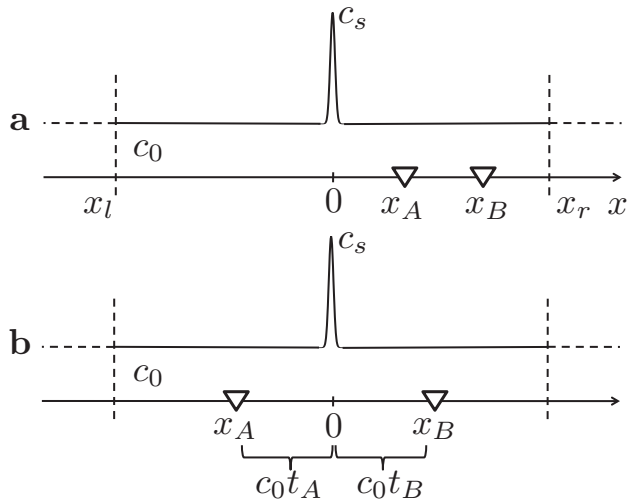

Figure 2.19: Configurations of the system used to show the connection between the Green's function reconstruction and the optical theorem. In both cases, the receivers x_A and x_B are located outside the scatterer c_s, which is located at $x = 0$.

The above expressions of the optical theorem in one dimension agree with the work of Hovakimian (2005) and differ from their three-dimensional counterpart because they contain the real part of the scattering amplitude instead of the imaginary part: $2\Re f(n,n) \equiv f(n,n)+$

$f^*(n,n)$, where $\Re$ indicates the real part. We note that the ordinary form of the optical theorem 2.25 also follows from its generalized form 2.26 (the former is a special case of the latter). Furthermore, equation 2.26 is equivalent to the expression for the optical theorem derived in the previous section, equation 2.22. This is not surprising because both equations 2.26 and 2.22 have been derived from the same fundamental equation 2.11.

2.6 Conclusions

In the Visual Tour section, we described the connection between different scattering principles, showing that there are three distinct ways to reconstruct the same wavefield. A physical source, the Green's function reconstruction technique, and inverse scattering theory allow one to create the same wavestate (see Figure 2.8) originated by an impulsive source placed at a certain location x_s ($x = 1.44$ km in our examples). Green's function reconstruction tells us how to build an estimate of the wavefield without knowing the medium properties, if we have a receiver at the same location x_s of the real source and sources surrounding the scattering region. Inverse scattering goes beyond and allows us to focus the wavefield inside the medium (at location x_s) without knowing its properties, using only data recorded at one side of the medium. We showed that the interaction between causal and anti-causal wavefields is a key element to focus the wavefield where there is no real source; in fact $G_h = G^+ - G^-$, which satisfies the homogeneous wave equation 2.10, is a superposition of the causal and anti-causal Green's functions.

We speculate that many of the insights gained in our one-dimensional framework are still valid in higher dimensions. An extension of this work in two or three dimensions would give us the theoretical tools for many useful practical applications. For example, if we knew how to create the three-dimensional version of the incident wavefield shown in Figure 2.12, we could focus the wavefield to a point in the subsurface to simulate a source at depth and to record data at the surface (Figure 2.16); these kind of data are of extreme importance for full waveform inversion techniques (Brenders and Pratt, 2007) and imaging of complex structures, e.g. under salt bodies in seismic exploration (Sava and Biondi, 2004). Furthermore, we could

possibly concentrate the energy of the wavefield inside a hydrocarbon reservoir to fracture the rocks and improve the production of oil and gas (Beresnev and Johnson, 1994).

In the second part of this tutorial, the Mathematical Tour, we demonstrated that the representation theorem for the homogeneous Green's function G_h , equation 2.11, constitutes a theoretical framework for various scattering principles. We showed that all the principles and their equations (see Table 2.1) rely on G_h as a starting point for their derivation. As mentioned above, the fundamental role played by the combination of the causal and anti-causal Green's functions has been evident throughout all the Mathematical Tour: it is this combination that allows one to focus the wavefield to a location where neither a real source nor a receiver can be placed.

2.7 Acknowledgments

The authors would like to thank the members of the Center for Wave Phenomena and an anonymous reviewer for their constructive comments. This work was supported by the sponsors of the Consortium Project on Seismic Inverse Methods for Complex Structures at the Center for Wave Phenomena.

CHAPTER 3

FOCUSING THE WAVEFIELD INSIDE AN UNKNOWN 1D MEDIUM - BEYOND SEISMIC INTERFEROMETRY

Filippo Broggini[1,2], **Roel Snieder**[1], **and Kees Wapenaar**[3]

Published in *Geophysics* (2012): 77 (5), A25-A28

3.1 Abstract

With seismic interferometry one can retrieve the response to a virtual source inside an unknown medium, if there is a receiver at the position of the virtual source. In this letter, using inverse scattering theory, we demonstrate that for a 1D medium the requirement of having an actual receiver inside the medium can be circumvented, going beyond seismic interferometry. In this case, the wavefield can be focused inside an unknown medium with independent variations in velocity and density using reflection data only.

3.2 Introduction

There are different ways to reconstruct the wavefield excited by a hypothetical source in the interior of an unknown medium. First, with seismic interferometry (Curtis et al., 2006; Schuster, 2009; Wapenaar et al., 2005; Weaver and Lobkis, 2001) it is possible to retrieve the response to a virtual source inside the medium, with a receiver at the position where the virtual source is to be created, assuming the medium is surrounded by uncorrelated sources. The medium parameters need not be known. Second, in this paper we show that, with one-dimensional inverse scattering theory (Chadan and Sabatier, 1989; Colton and Kress, 1998; Gladwell, 1993), the response to a virtual source inside the medium can be obtained from reflected waves recorded at one side of the medium. We demonstrate that,

[1]Center for Wave Phenomena, Colorado School of Mines, Golden, CO 80401, USA
[2]Principal researcher and author
[3]Delft University of Technology, Department of Geoscience and Engineering, Delft, The Netherlands

in one-dimensional media, this is possible without knowing the medium parameters. This is fascinating because it allows one to obtain the same virtual source response as with seismic interferometry (including all multiples), but without the need to have a receiver at the virtual source location. An essential element of this approach is to build an incident wave that is designed to collapse onto a point inside the medium at a specified time. The reconstructed wavefield can be used to illuminate the medium under a complicated overburden, and the extracted Green's function can be used for imaging.

In this paper, the term focusing (Rose, 2001, 2002b) refers to the technique of finding an incident wave that collapses to a spatial delta function $\delta(z - z_0)$ at the location z_0 and at a prescribed time t_0 (i.e., the wavefield is focused at z_0 at t_0). In a one-dimensional medium, we deal with a one-sided problem when observations from only one side of the perturbation are available (e.g., due to the practical consideration that we can only record reflected waves); otherwise, we call it a two-sided problem when we have access to both sides of the medium and account for both reflected and transmitted waves.

3.3 Wavefield focusing

Figure 3.1 shows the velocity and density profiles of a one-dimensional acoustic medium. Note that velocity and density vary independently in depth. We simulate a numerical scattering experiment where an impulsive source is placed at the position $z = 2.44$ km. The acoustic wave equation is $LG(z, z_{VS}, t) = -\delta(z - z_{VS})\frac{\partial}{\partial t}\delta(t)$, with the differential operator $L \equiv \rho(z)\frac{\partial}{\partial z}(\rho(z)^{-1}\frac{\partial}{\partial z}) - c(z)^{-2}\frac{\partial^2}{\partial t^2}$. Here $z_{VS} = 2.44$ km and the initial condition is $G(z, z_{VS}, t < 0) = 0$. The incident wavefield propagates toward the discontinuities in the model, interacts with them, and generates scattered waves. We use a time-space finite-difference code with absorbing boundary conditions to simulate the propagation of the one-dimensional waves and to produce the numerical examples shown in this section. For computational purposes, the source function $-\delta(z - z_{VS})\frac{d}{dt}\delta(t)$ is convolved with a band-limited wavelet $s(t)$. The computed wavefield shown in Figure 3.2 represents the causal Green's function of the system, G, convolved with $s(t)$. Causality ensures that the wavefield is non-

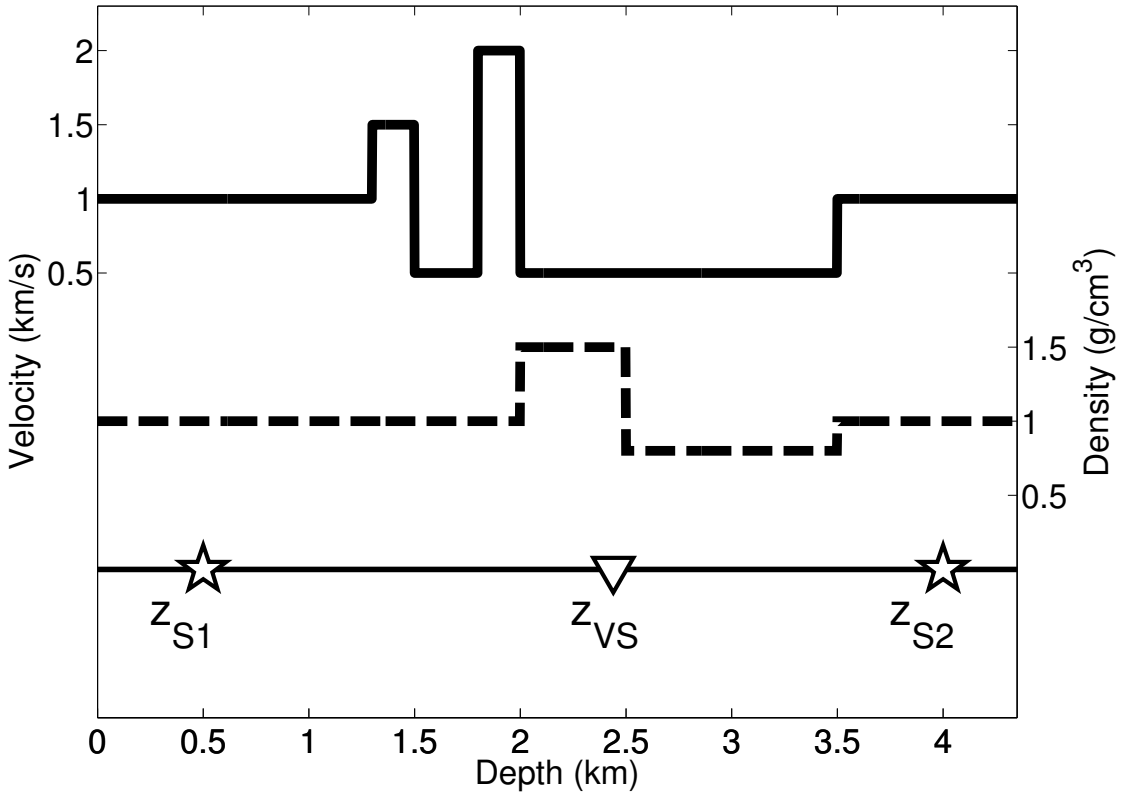

Figure 3.1: Top: Velocity profile of the one-dimensional model (solid line). The perturbation in the velocity is located between $z = 1.3 - 3.5$ km and $c_0 = 1$ km/s. Middle: Density profile of the one-dimensional model (dashed line). The perturbation in the density is located between $z = 2.0 - 3.5$ km and $\rho_0 = 1$ g/cm^3. Bottom: Locations of the real and virtual sources for seismic interferometry. z_{S1} and z_{S2} indicate the two real sources. z_{VS} shows the virtual source location.

zero only in the region delimited by the first arrivals (i.e., the direct waves) and we refer to it as the *causal region*.

Due to practical limitations in field experiments, we usually are not able to place a source inside the medium we want to probe. However, when there are receivers inside the medium, seismic interferometry allows us to determine the wavefield, as if there was a source at the position of any of the receivers, e.g. at $z = 2.44$ km. This technique allows one to reconstruct the wavefield that propagates between a virtual source and other receivers located inside the medium (Wapenaar et al., 2005). This technique yields a combination of the causal wavefield G and its time-reversed version G^a (i.e., anti-causal). This is due to

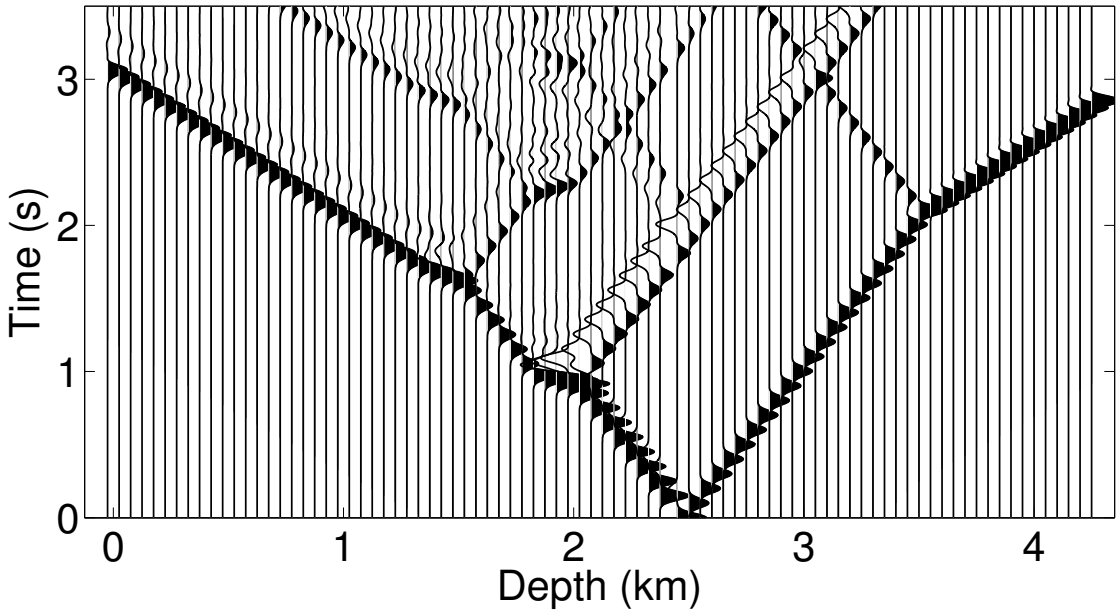

Figure 3.2: Response to a source located at $z = 2.44$ km. The traces are recorded by receivers located at each location in the model (shown in Figure 3.1) with a spacing of 40 m. Waves are emanating from the line $t = 0$ s only at $z = 2.44$ km.

the fact that the reconstructed wavefield propagates between a receiver and a virtual source. Conceptually speaking, without a real (physical) source, one must have non-zero incident waves on a receiver to create waves that emanate from that receiver. The fundamental equation to reconstruct the Green's function is (Wapenaar and Fokkema, 2006)

$$\begin{aligned} &G(z, z_{VS}, t) + G(z, z_{VS}, -t) \\ &\quad \propto \sum_{z'=z_{S1}, z_{S1}} G(z, z', t) * G(z_{VS}, z', -t), \end{aligned} \tag{3.1}$$

where $z_{VS} = 2.44$ km, and z_{S1} and z_{S2} are the coordinates of impulsive sources located at both sides of the perturbation (a total of two sources in 1D) as shown at the bottom of Figure 3.1. Between z_{S1} and z_{S2}, the causal part of the wavefield estimated by this Green's function reconstruction technique is consistent with the wavefield shown in Figure 3.2.

We thus have two different ways to obtain the same wavefield, but often we cannot place any sources or receivers inside the medium. We next assume that we only have access to reflected waves $R(t)$ measured above the perturbation, i.e. the reflected impulse response

measured at $z = 0$ km due to an impulsive source placed at $z = 0$ km. This limitation raises another question: Can we reconstruct the same wavefield shown in Figure 3.2 having knowledge only of the reflected waves $R(t)$? For this one-dimensional problem, the answer to this question is given by the Marchenko equation (Chadan and Sabatier, 1989; Lamb, 1980). Its solution provides a particular incident wave that collapses the wavefield to a spatial delta function at the desired location after it interacts with the medium, and this incident wave consists of a delta function added to the solution of the Marchenko equation (Rose, 2001, 2002a).

The Marchenko integral equation is a fundamental relation of one-dimensional inverse scattering theory. It is an integral equation that relates the reflected waves $R(t)$ to the incident wavefield $u(t, t_f)$ which creates a focus in the interior of the medium and ultimately gives the perturbation of the medium. The one-dimensional form of this equation is

$$0 = R(t + t_f) + u(t, t_f) + \int_{-\infty}^{t_f} R(t + t')u(t', t_f)dt' \text{ for } t \geq -t_f, \tag{3.2}$$

where t_f is the one-way travel time from $z = 0$ to the focusing location. We numerically solve the Marchenko equation and construct the particular incident wave that focuses at $t = 0$ s at a location specified by $t_f = 3$ s. Any appropriate numerical method to solve integral equations can be used to compute the unknown wavefield $u(t, t_f)$ (e.g., an iterative method). Note that solving Equation 3.2 does not require any knowledge of the medium: all that is needed is the reflection response $R(t)$ and the one-way travel time t_f, which specifies the location of the focus. Next, we inject the particular incident wave $\delta(t + t_f) + u(-t, t_f)$ at $z = 0$ km and compute the time-space diagram shown in the top panel of Figure 3.3: this shows the wavefield when the incident wave is injected at $z = 0$ into the model. We define this wavefield as $K(z, t)$. The time-space diagram shown in Figure 3.3 is computed using the true model, but this is done only to illustrate the physics of the focusing process. The bottom panel of Figure 3.3 shows a cross-section of the wavefield at time $t = 0$ s: the wavefield vanishes except at location $z = 2.44$ km. For this particular model, $t_f = 3$ s

corresponds to spatial focusing at the same location where we placed the virtual source in Figure 3.1. We emphasize that this method is data driven, hence the true model is not needed to build the particular incident wavefield.

Figure 3.3 does not yet resemble the wavefield shown in Figure 3.2. In fact, in Figure 3.3 waves cross the solid line at $t = 0$ s for locations $z \leq 2.44$ km, while in Figure 3.2 waves cross the same solid line only at the virtual source location $z = 2.44$ km. However, denoting as $K(z, -t)$ the time-reversed version of $K(z, t)$, we obtain the wavefield shown in Figure 3.4 by adding $K(z, t)$ and $K(z, -t)$. With this summation, we create the response to a virtual source located at $z_{VS} = 2.44$ km, namely $G(z, z_{VS}, t) + G(z, z_{VS}, -t)$ (convolved with $s(t)$). This step is the main result of this paper. Note that the trace at $z = 0$, $K(0, t)+K(0, -t)$, has been obtained without any information about the model. As in Figure 3.3, the remainder of Figure 3.4 is based on the true model and is only shown to explain the physics of the focusing process. In Figure 3.4, the wavefield outside the causal region is zero because the portion of $K(z, t)$ outside the causal region is antisymmetric in time and hence cancels in the sum $K(z, t) + K(z, -t)$. With this process, we effectively go from one-sided to two-sided illumination because in Figure 3.4 waves are incident onto the focusing location from both sides for $t < 0$ s. The incident waves are non zero for $-6s < t < -3s$, but to facilitate a comparison with Figure 3.2 this time interval is not completely included in the figure. According to Figure 3.4, we create a focus at a location inside the inhomogeneous medium without having a source or a receiver at such a location and without any knowledge of the medium properties; we only have access to the reflected impulse response measured above the perturbation. With an appropriate choice of sources and receivers, this experiment can be done in practice, e.g., in an acoustics laboratory (Rose, 2002a). Burridge (1980) shows diagrams similar to Figures 3.3 and 3.4 and explains how to combine such diagrams using causality and symmetry properties. The wavefield for positive times $t > 0$ (causal region) in Figure 3.4 corresponds to the causal Green's function G and the wavefield for negative times $t < 0$ represents the anti-causal Green's function G^a (defining the anti-causal region).

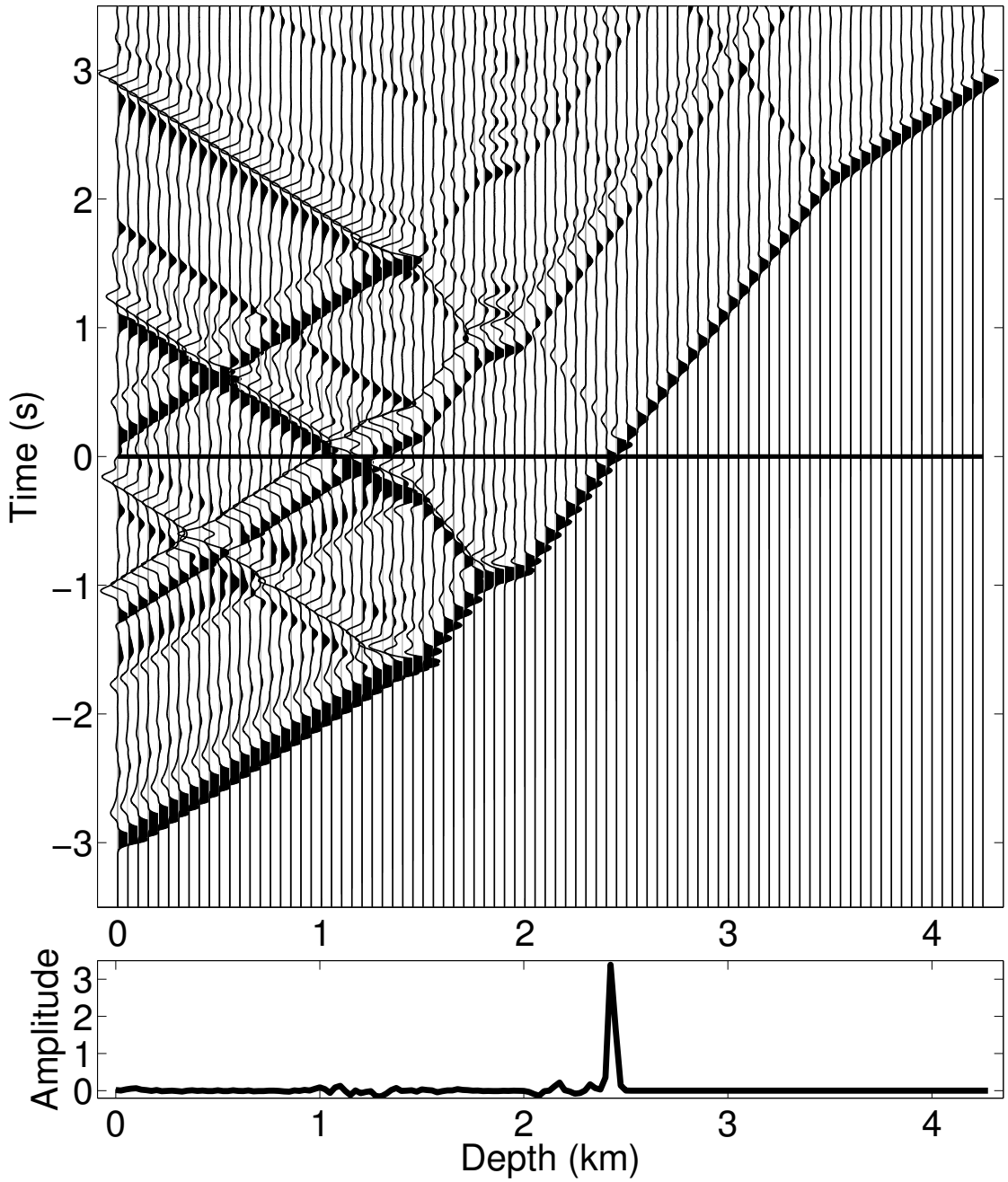

Figure 3.3: Top: At $z = 0$ km, we inject the particular incident wave in the model and compute the time-space diagram by forward modeling. We denote this wavefield as $K(z, t)$. Waves cross the solid line at $t = 0$ s for locations $z \leq 2.44$ km. Note that the waves continue to propagate after 3 s. Bottom: cross-section of the wavefield at $t = 0$ s.

A small amount of energy is outside of the causal and anti-causal regions due to numerical inaccuracies in our solution of the Marchenko equation (this is also visible in the bottom panel of Figures 3.3 and 3.4). The causal part of the trace at $z = 0$ km is the virtual source response $G(0, z_{VS}, t)$ that we obtained without using the model.

The anti-causal Green's function G^a follows from G by time-reversal, hence it satisfies $LG^a = -\delta(z - z_{VS})\frac{\partial}{\partial(-t)}\delta(-t) = \delta(z - z_{VS})\frac{\partial}{\partial t}\delta(t)$, where we used that L is invariant to time-reversal. Adding the differential equations for G and G^a shows that $G + G^a$ satisfies the homogeneous equation: $L(G + G^a) = -\delta(z - z_{VS})\frac{\partial}{\partial t}\delta(t) + \delta(z - z_{VS})\frac{\partial}{\partial t}\delta(t) = 0$. The term *homogeneous* suggests that the sum of G and G^a is source free. Hence, to focus the wavefield at the virtual source location, there must be a particular incident wavefield coming from another location. In fact, the knowledge that $G + G^a$ satisfies a homogeneous equation suggests that a combination of the causal and anti-causal Green's functions is needed to focus the wavefield at a location where there is no real source (i.e., source free), as shown in Figure 3.4. Oristaglio (1989) shows a similar result, although he derives the difference (instead of the sum) of the causal and anti-causal Green's functions due to a different definition of the Green's functions.

3.4 Discussion

In the previous section, we use the one-way travel time t_f to determine the depth z_{VS} of the virtual source. In other words, the wavefield focuses at the virtual source location z_{VS} after it has propagated inside the medium for a length of time equal to t_f. In order to directly choose a prescribed focusing location z_{VS} (and not a prescribed one-way travel time t_f), we need to know the average velocity of the medium between the surface and the depth of the focusing location. However, no information about either the density or the details of the velocity profile is required.

This method also works when density and velocity vary independently. This fact is a new contribution because the previous inverse scattering theory of Rose (2001, 2002b) and others (Aktosun and Rose, 2002) does not deal with simultaneous changes in density and

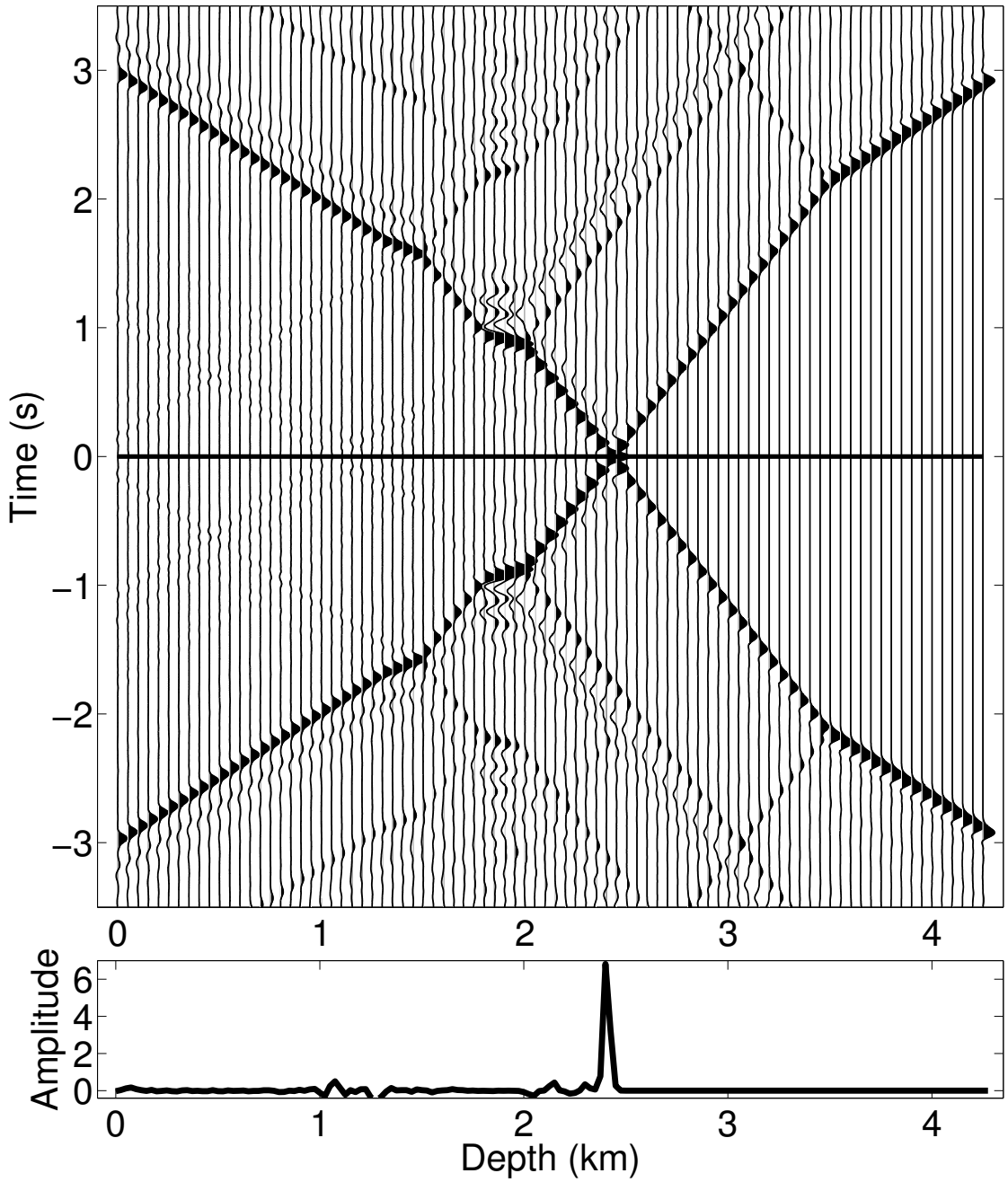

Figure 3.4: Top: Wavefield that focuses at $z = 2.44$ km at $t = 0$ s without a source or a receiver at this location. This wavefield corresponds to $K(z,t) + K(z,-t)$ and consists of a causal ($t > 0$) and an anti-causal ($t < 0$) region. Bottom: cross-section of the wavefield at $t = 0$ s.

velocity, because one cannot retrieve two independent quantities from one time series of reflected waves. We also add another step beyond the work of Rose by forming the sum $K(z,t) + K(z,-t)$, which ensures that the wavefield vanishes outside the causal and anti-causal regions and creates the response of the virtual source. We show that the interaction between causal and anti-causal wavefields is a key element to focus the wavefield where there is no real source.

We are currently investigating the application of the central ideas of this work to wave propagation in two and three dimensions (Wapenaar et al., 2011a). This extension allows us to focus the wavefield to a point in the subsurface to simulate a source at depth and to record data at the surface. This kind of application will be helpful for full waveform inversion (Brenders and Pratt, 2007) and subsalt imaging (Sava and Biondi, 2004), where waves that have traversed a strongly inhomogeneous overburden are of extreme importance. We speculate that focusing the wavefield at a prescribed location in two- and three-dimensional media requires an estimate of the primary traveltimes from the virtual source location to the receivers (e.g., using a macro model). Wapenaar et al. (2012a) give a first mathematical proof for a two-dimensional medium with density variations only.

3.5 Conclusions

There are three distinct ways to reconstruct the same physical wave state. A physical source, seismic interferometry, and inverse scattering theory allow one to create the same wave state that focuses at a certain location z_{VS}. Seismic interferometry tells us how to build an estimate of the wavefield without knowing the medium properties, if we have a receiver at the same location z_{VS} of the real source in the scattering experiment of Figure 3.2 and sources surrounding the medium. Inverse scattering goes beyond this as it allows us to focus the wavefield inside the medium without knowing its properties, using only reflected waves $R(t)$ recorded at one side of the medium.

3.6 Acknowledgments

The authors thank the members of the Center for Wave Phenomena, Kasper van Wijk, Andrew Curtis, and two anonymous reviewers for their constructive comments. This work was supported by the sponsors of the Consortium Project on Seismic Inverse Methods for Complex Structures at the Center for Wave Phenomena.

CHAPTER 4

DATA-DRIVEN GREEN'S FUNCTION RECONSTRUCTION AND APPLICATION TO IMAGING WITH MULTIDIMENSIONAL DECONVOLUTION

Filippo Broggini[1,2], **Kees Wapenaar**[3], **Joost van der Neut**[3], **and Roel Snieder**[1]

Submitted to *Inverse Problems*

4.1 Abstract

We discuss an iterative method that allows one to reconstruct the Green's function originating from a virtual source located inside a medium using reflection data measured only at the acquisition surface. In addition to the reflection response, we require an estimate of the traveltimes corresponding to the direct arrivals. However, no detailed information about the heterogeneities in the medium is needed. The iterative scheme generalizes the Marchenko equation for inverse scattering to the seismic reflection problem. We analyse the method for a simple layered medium using physical arguments based on the stationary-phase method and show that the retrieved Green's wave field correctly contains the multiples due to the inhomogeneities present in the medium. Additionally, a variant of the iterative scheme allows us to decompose the reconstructed wave field into its downgoing and upgoing components. These wave fields are then used to create a ghost-free image of the medium with either crosscorrelation or multidimensional deconvolution, presenting an advantage over standard prestack migration.

4.2 Introduction

One of the main goals of seismic imaging is to retrieve the location and amplitude of reflectors in the subsurface from reflection data acquired on the surface of the earth. This

[1]Center for Wave Phenomena, Colorado School of Mines, Golden, CO 80401, USA
[2]Principal researcher and author
[3]Delft University of Technology, Department of Geoscience and Engineering, Delft, The Netherlands

is an important and challenging task because an accurate image of the structures inside the earth is needed to locate hydrocarbon reservoirs.

We discuss a new approach to reconstruct the full Green's function originating from a virtual source located inside a medium using only reflection data measured at the acquisition surface. Existing methods, such as seismic interferometry (Bakulin and Calvert, 2006; Schuster, 2009), allow one to retrieve this Green's wave field without any knowledge of the medium itself. Despite their advantages, these methods present two major drawbacks: 1) they require a receiver at the location of the virtual source in the subsurface and 2) they assume the medium is surrounded by sources. Our approach removes these constraints and is based on an extension of the one-dimensional theory proposed by Broggini et al. (2011; 2012b) and Broggini and Snieder (2012) which was based on earlier work by Rose (2002a). They show that, given the reflection response of a one-dimensional layered medium, it is possible to reconstruct the response to a virtual source inside the medium, without having a receiver at the virtual source location and without knowing the medium. Wapenaar et al. (2013a) generalized this to three-dimensional media. This new method consists of an iterative algorithm that transforms the reflection response (at the acquisition surface) of an arbitrary medium into the wave field generated by a virtual source inside the unknown medium. This can be interpreted as a redatuming process. Apart from requiring the reflection data measured at the surface, the proposed method also requires an estimate of the traveltimes of the first arriving wave travelling from the virtual source location to receivers located at the acquisition surface. These traveltimes are a key element of the method because they specify the location of the virtual source in the subsurface. Consequently, the proposed method is not fully model-independent. However, we do not require any more knowledge of the medium parameters than standard primary imaging schemes. As in seismic interferometry (Curtis et al., 2006; Schuster, 2009), our goal is to retrieve the response to a virtual source inside an unknown medium, removing the imprint of a complex subsurface. This is helpful in situations where waves have traversed a strongly inhomogeneous overburden, e.g., subsalt

(Sava and Biondi, 2004) and near-surface imaging (Keho and Kelamis, 2012).

Following the approach of Wapenaar et al. (2012a), we analyse the iterative method for a layered configuration with three parallel dipping reflectors characterized by variable-density and constant-velocity. We use physical arguments based on the stationary-phase method to show that the method converges and allows for the reconstruction of the wave field originating from the virtual source location. Then, we show that a variant of the iterative scheme allows us to decompose the reconstructed Green's function into its downgoing and upgoing components. Finally, these decomposed wave fields are used to create a ghost-free image of the subsurface. This image is constructed using either simple crosscorrelations or multi-dimensional deconvolution and is compared to standard prestack migration (Claerbout, 1985).

4.3 Stationary-phase analysis

We discuss the proposed iterative scheme for a simple two-dimensional configuration. We use a geometrical approach to the method of stationary phase to solve the Rayleigh-like integrals which yield the reflected response to an arbitrary incident field. We explain each step of the iterative procedure and emphasize the physical arguments that support our expectations for the method to converge to the virtual-source response.

4.3.1 Configuration

We consider a model characterized by three parallel dipping reflectors in a lossless, constant-velocity, variable-density medium as shown in Figure 4.1. The proposed iterative scheme is, however, not restricted to a medium where the velocity does not vary in space (Wapenaar et al., 2013a). We choose this particular configuration because well-known analytical equations describe the wave fields propagating in constant velocity media. The velocity of the medium is equal to $c = 2000$ m/s. We denote spatial coordinates as $\mathbf{x} = (x, z)$. The acquisition surface is located at $z = 0$ m and does not correspond to an actual reflector, hence it does not cause reflections. The reflector at the top is described by the equation

$z = z_1 - ax$ with $z_1 = 800$ m and $a = 1/7$. The black dot denotes the position of the virtual source, with coordinates $\mathbf{x}_{VS} = (x_{VS}, z_{VS}) = (0, 1500)$ m. The middle and bottom reflector are characterized by the same dipping angle. For this reason, all mirror images of the virtual source are located on a line orthogonal to the reflectors. All the points on this line satisfy the relation $z = z_{VS} + x/a$. The first, second, and third reflectors cross this line at $\mathbf{x}_1 = (-98, 814)$ m, $\mathbf{x}_2 = (-42, 1206)$ m, and $\mathbf{x}_3 = (35, 1745)$ m, respectively. The densities in the four layers are $\rho_1 = \rho_3 = 1000$ kg/m^3, $\rho_2 = 5000$ kg/m^3, and $\rho_4 = 3000$ kg/m^3, respectively. When a downgoing wave reaches one of the boundaries separating layers with different density, it gives rise to reflected and transmitted waves. The reflection and transmission coefficients are defined by $r_n = (\rho_{n+1} - \rho_n)/(\rho_{n+1} + \rho_n)$ and $\tau_n^+ = 1 + r_n$, respectively, where $n = 1, 2, 3$ denotes the layer. Similarly, the reflection and transmission coefficients for upgoing waves are $-r_n$ and $\tau_n^- = 1 - r_n$. Since the velocity is constant in this particular configuration, the reflection and transmission coefficients hold not only for normal incidence but for all the angles of incidence. Note that the large contrast between the density of the layers causes strong multiple reflections.

4.3.2 Primary arrivals

We define the Green's function $G(\mathbf{x}, \mathbf{x}_S, t)$ as a wave field that satisfies the wave equation $LG = -\rho\delta(\mathbf{x} - \mathbf{x}_S)\frac{\partial\delta(t)}{\partial t}$, with $L = \rho\nabla\cdot(\rho^{-1}\nabla) - c^{-2}\frac{\partial^2}{\partial t^2}$. According to de Hoop (1995), the Green's function corresponds to the response to an impulsive point source of volume injection rate located at $\mathbf{x}_S$. Figure 4.2 shows the total field originated by a real source located at $\mathbf{x}_{VS}$, i.e., $G(\mathbf{x}, \mathbf{x}_{VS}, t) * s(t)$, where $s(t)$ is a Ricker wavelet with a central frequency of 15 Hz and $*$ denotes temporal convolution. It is essential that $s(t)$ is zero phase. This is the reference wave field that we want to reconstruct. Using the Fourier convention $\hat{F}(\omega) = \int_{-\infty}^{+\infty} f(t)\exp(-j\omega t)\mathrm{d}t$, the frequency domain Green's function $\hat{G}(\mathbf{x}, \mathbf{x}_S, \omega)$ obeys the equation $\hat{L}\hat{G} = -j\omega\rho\delta(\mathbf{x} - \mathbf{x}_S)$, with $\hat{L} = \rho\nabla\cdot(\rho^{-1}\nabla) + \omega^2/c^2$. Here j is the imaginary unit and ω denotes the angular frequency. We decompose the Green's function in its direct and scattered components, $\hat{G} = \hat{G}^d + \hat{G}^s$.

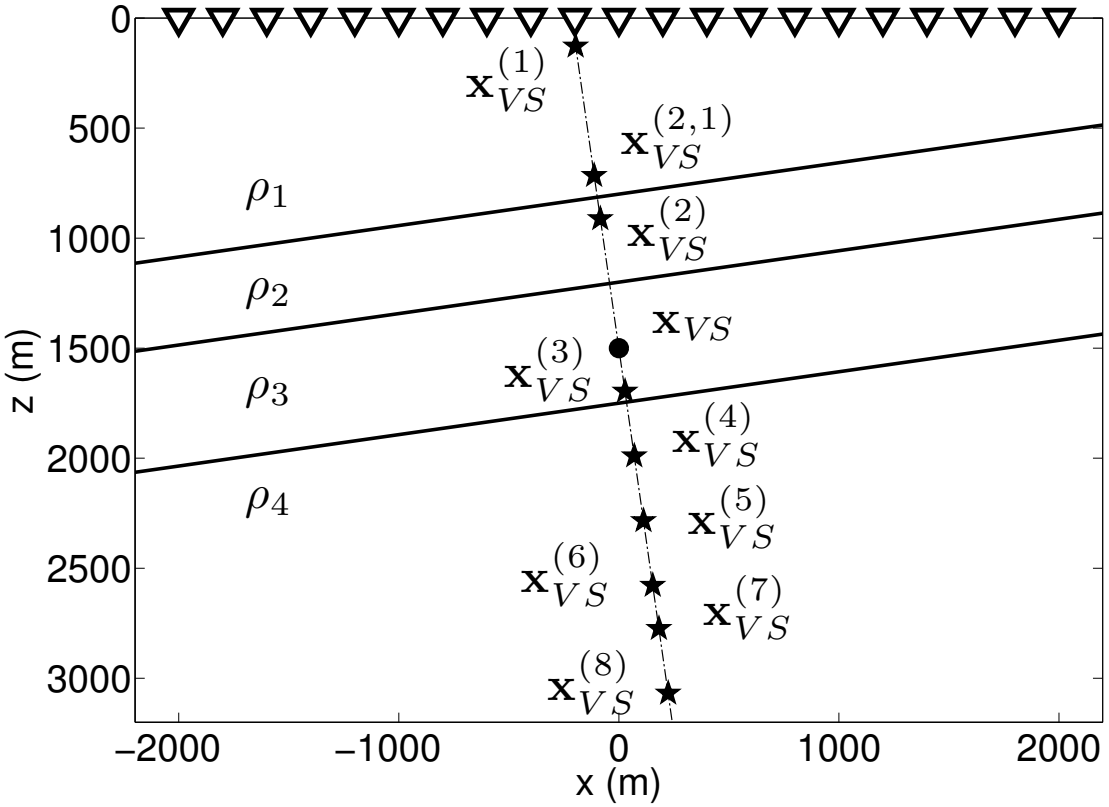

Figure 4.1: Configuration with three dipping reflectors. The black dot indicates the location of the virtual source $\mathbf{x}_{VS}$. The black star shaped symbols indicate the locations of the mirror images of the virtual source. $\mathbf{x}_{VS}^{(2,1)}$ is the mirror image of $\mathbf{x}_{VS}^{(2)}$ with respect to the first reflector. The white triangles denotes the receivers at $z = 0$. The virtual source and its mirror images lie on the line $z = z_{VS} + x/a$, with $z_{VS} = 1500$ m and $a = 1/7$.

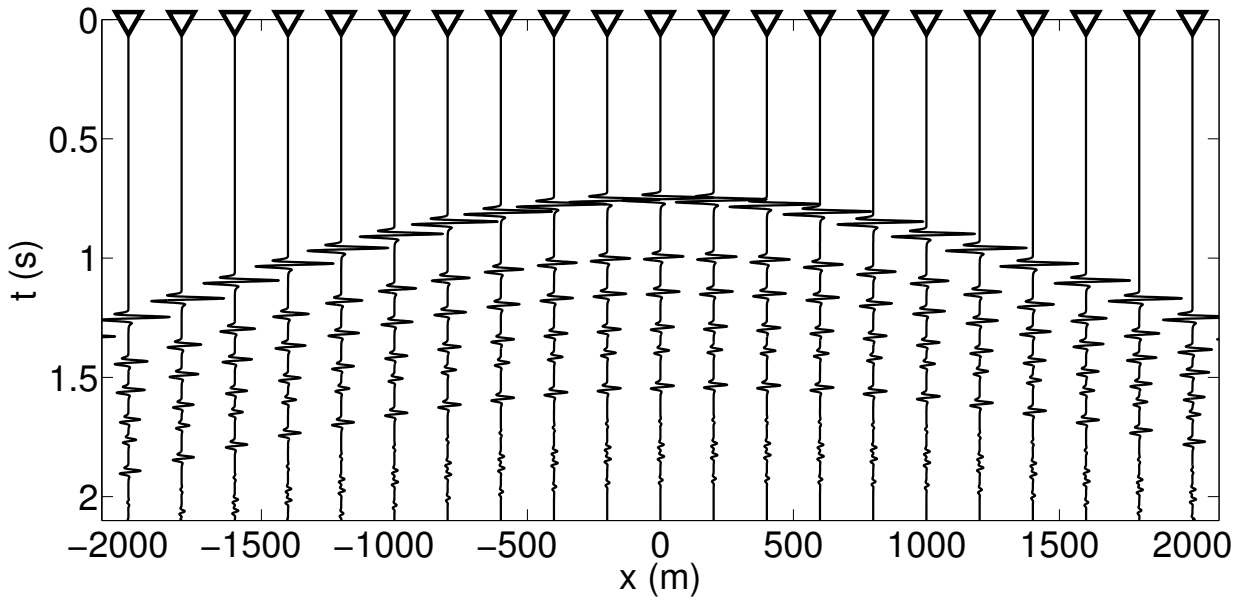

Figure 4.2: Total field originated by a real source located at $\mathbf{x}_{VS}$, i.e., $G(\mathbf{x}, \mathbf{x}_{VS}, t) * s(t)$. This is the reference wave field.

As mentioned in the introduction, we need an estimate of the direct arrivals. For the simple configuration of Figure 4.1, where there are only variations in density, the high-frequency approximation of the Fourier transform of the direct Green's function $G^d(\mathbf{x}, \mathbf{x}_{VS}, t)$ is given by $\hat{G}^d(\mathbf{x}, \mathbf{x}_{VS}, \omega) = \tau_1^- \tau_2^- \rho_3 \hat{G}_0^d(\mathbf{x}, \mathbf{x}_{VS}, \omega)$, with

$$\hat{G}_0^d(\mathbf{x}, \mathbf{x}_{VS}, \omega) = j\omega \frac{\exp\{-j(\omega|\mathbf{x} - \mathbf{x}_{VS}|/c + \mu\pi/4)\}}{\sqrt{8\pi|\omega||\mathbf{x} - \mathbf{x}_{VS}|/c}}, \tag{4.1}$$

where $\mu = \text{sign}(\omega)$ (Snieder, 2004). We define $\hat{G}_0^d(\mathbf{x}, \mathbf{x}_{VS}, \omega)$ as the scaled direct Green's function and its temporal counterpart $G_0^d(\mathbf{x}, \mathbf{x}_{VS}, t)$, convolved with $s(t)$, is shown in Figure 4.3. We see that $\hat{G}_0^d(\mathbf{x}, \mathbf{x}_{VS}, \omega)$ does not necessitate information about the position of the interfaces or about the density, but it only depends on the traveltime $|\mathbf{x} - \mathbf{x}_{VS}|/c$. In Figure 4.3, we also define two traveltime curves indicated by the solid black lines. The lower curve describes the onset time of the direct arrivals and the upper curve is defined as the time-reversal of the lower curve. These two curves allow us to define a window function

$$w(\mathbf{x}, t) = 1 \quad \text{between the solid black lines of Figure 4.3,}$$

$$w(\mathbf{x}, t) = 0 \quad \text{elsewhere.}$$

This window function is a key component of the iterative scheme.

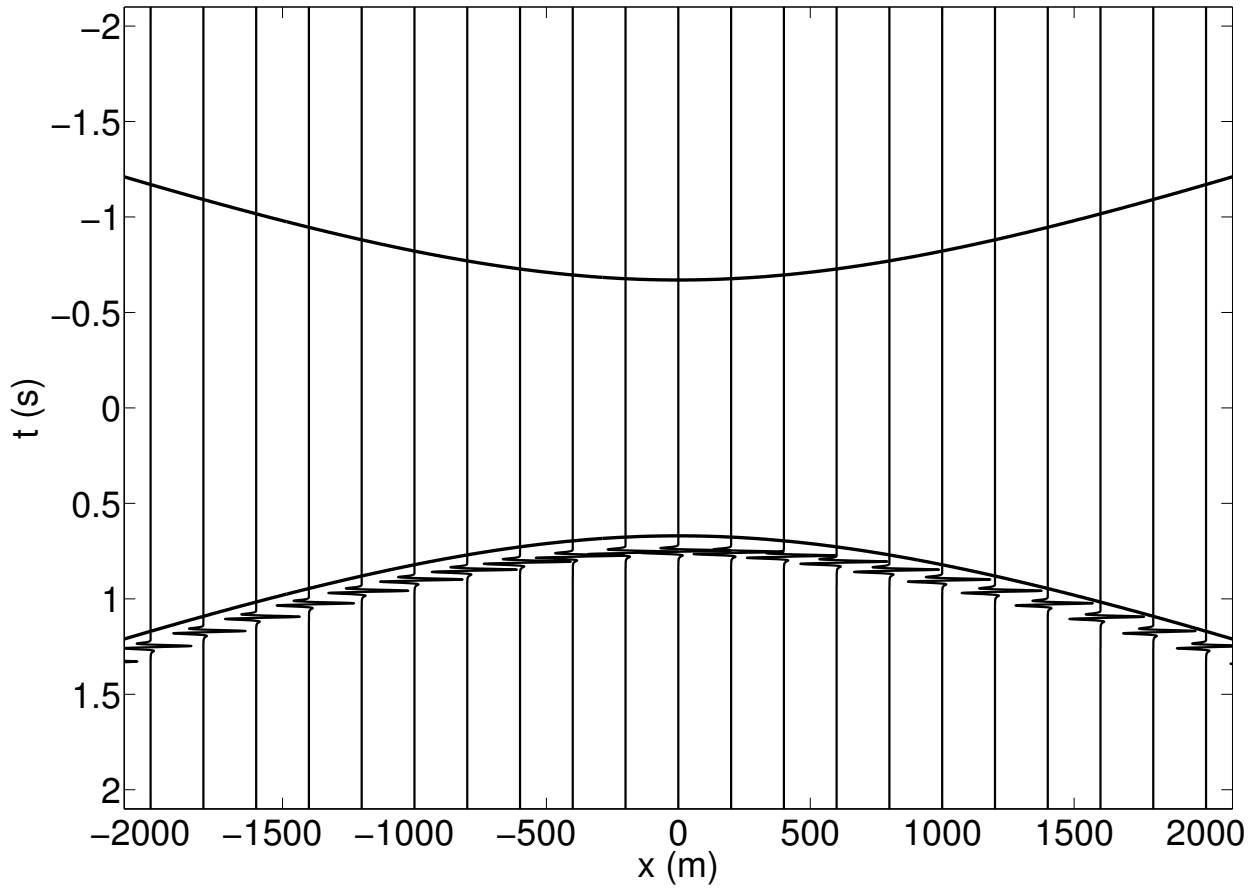

Figure 4.3: Scaled direct arrivals of the response to the virtual source $\mathbf{x}_{VS}$ measured at the acquisition surface. The bottom solid black line indicates the onset time of the direct arrivals. The top solid black lines is the time-reversed version of the bottom black line.

4.3.3 Reflection response

To retrieve the virtual-source response $G(\mathbf{x}, \mathbf{x}_{VS}, t)$, we need the reflection response at the surface $R(\mathbf{x}_R, \mathbf{x}_S, t) * s(t)$ in addition to an estimate of the direct arrivals. We assume that the reflection data do not include any multiples related to the acquisition surface. If surface-related multiples are present in the reflection data, then they must be removed with an appropriate technique (Amundsen, 2001; van Groenestijn and Verschuur, 2009; Verschuur

et al., 1992). Following Wapenaar and Berkhout (1993) (equation 15a), the reflection response can be derived from a Rayleigh-type integral:

$$\hat{p}^{-}(\mathbf{x}_R,\omega) = \int_{-\infty}^{\infty} \frac{2}{j\omega\rho_1}\left[\frac{\partial \hat{G}^s(\mathbf{x}_R,\mathbf{x},\omega)}{\partial z}\hat{p}^{+}(\mathbf{x},\omega)\right]_{z=0} \mathrm{d}x, \tag{4.2}$$

where $\hat{p}^{+}$ and $\hat{p}^{-}$ are the Fourier transform of the downgoing and upgoing wave fields, respectively. Hence, in the frequency domain, we define the reflection response in terms of the scattered Green's function $\hat{G}^s$ via

$$\hat{R}(\mathbf{x}_R,\mathbf{x}_S,\omega)\hat{s}(\omega) = \frac{2}{j\omega\rho_1}\frac{\partial \hat{G}^s(\mathbf{x}_R,\mathbf{x}_S,\omega)}{\partial z_S}\hat{s}(\omega), \tag{4.3}$$

for $z_R = z_S = 0$ and after multiplying both sides by the spectrum of the source wavelet $s(t)$. According to Berkhout (1987), $\hat{R}(\mathbf{x}_R,\mathbf{x}_S,\omega)\hat{s}(\omega)$ is equivalent to the pressure recorded at $\mathbf{x}_R$ due to a force source located at $\mathbf{x}_S$ (multiplied by -2).

4.3.4 Initiating the iterative process

We define the initial incident downgoing wave field at $z = 0$ as the time-reversed version of the scaled direct arrivals at the recording surface excited by the virtual source in Figure 4.3. Hence, the initial wave field is $p_0^{+}(\mathbf{x},t) = G_0^d(\mathbf{x},\mathbf{x}_{VS},-t) * s(t)$ and is shown in Figure 4.4 with the label A. The subscript 0 of $p_0^{+}(\mathbf{x},t)$ indicates the initial wave field (or the 0th iteration).

The reflected upgoing wave field $p_0^{-}(\mathbf{x},t)$ is obtained by convolving the downgoing incident wave field $p_0^{+}(\mathbf{x},t)$ with the deconvolved reflection response and integrating over the source locations:

$$p_0^{-}(\mathbf{x}_R,t) = \int_{-\infty}^{\infty} \left[R(\mathbf{x}_R,\mathbf{x},t) * p_0^{+}(\mathbf{x},t)\right]_{z=0} \mathrm{d}x, \tag{4.4}$$

for $z_R = 0$. Equation 4.4 is the time-domain version of the Rayleigh integral described by equation 4.2. We discuss and solve this integral with geometrical arguments based on the method of stationary phase and we give a detailed mathematical derivation in the Appendix D. Figure 4.5 shows various rays for different receiver locations. Note that the rays of the

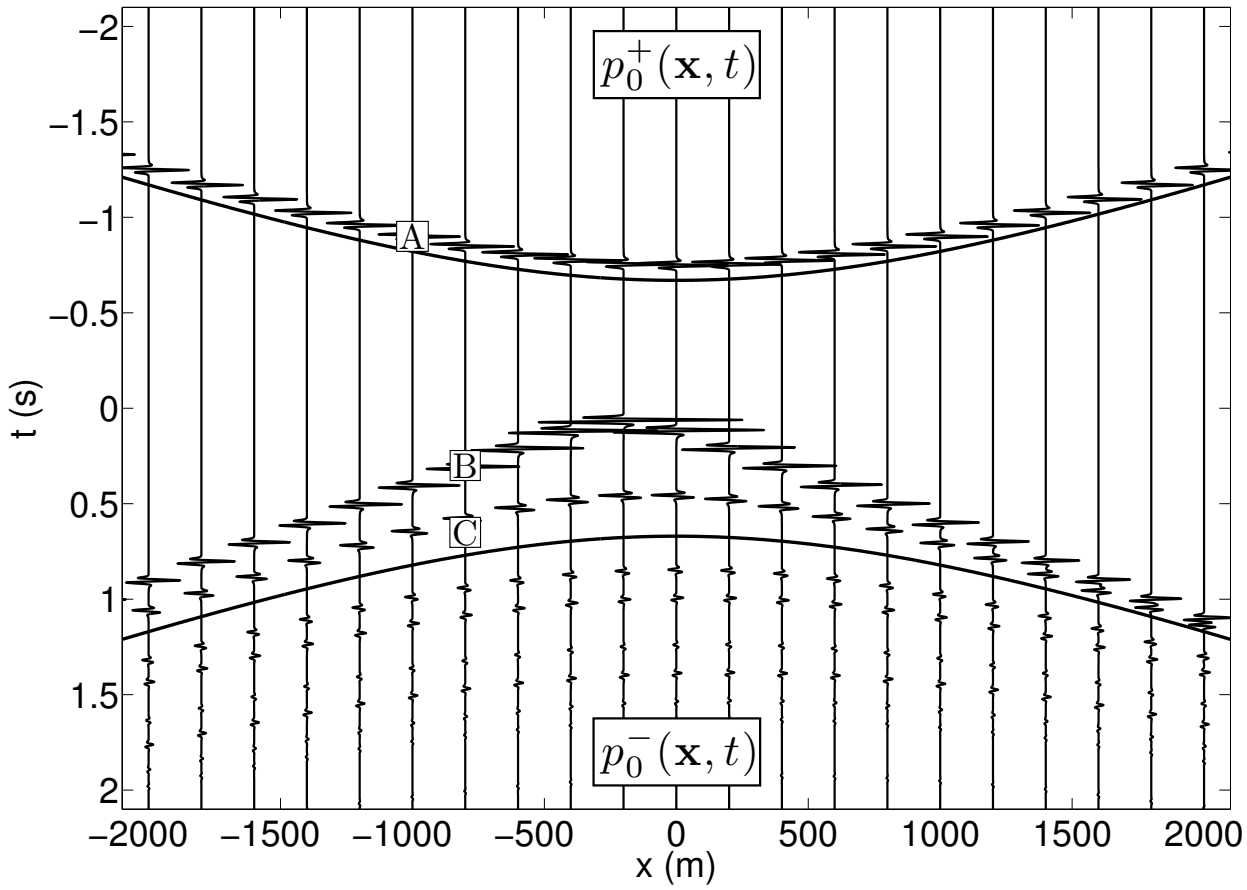

Figure 4.4: Initial incident wave field ($t < 0$) and its reflection response ($t > 0$), both measured at $z = 0$. Initial incident wave field is the time-reversal of Figure 4.3. We show the reflection response only until 2 s. The solid black lines denote the onset time of the direct arrivals and its time-reversed counterpart. These black lines are repeated in the subsequent figures.

incident field (converging in $\mathbf{x}_{VS}$) and of the reflection response (for the first reflector) have the same direction (Wapenaar et al., 2010, in the appendix). For this reason, these specific rays are said to be stationary. With simple geometrical arguments, it follows that these rays cross each other at the mirror image of the virtual source with respect to the first reflector, i.e., at $\mathbf{x}_{VS}^{(1)}$. Hence, the response of the first dipping reflector to the initial downgoing field appears to originate from a virtual source located at $\mathbf{x}_{VS}^{(1)}$. This wave field corresponds to $r_1 G_0^d(\mathbf{x}_R, \mathbf{x}_{VS}^{(1)}, t) * s(t)$, the first term on the right-hand side of equation D.21, and is shown as the event with label B in Figure 4.4. Following similar stationary-phase arguments, the response of the second reflector to the initial downgoing field apparently originates from a mirror image of the virtual source with respect to the second reflector, i.e., at $\mathbf{x}_{VS}^{(2)}$. This response is equal to $\tau_1^- r_2 \tau_1^+ G_0^d(\mathbf{x}_R, \mathbf{x}_{VS}^{(2)}, t) * s(t)$ and corresponds to the second term on the right-hand side of equation D.21 (see the event with label C in Figure 4.4). However, the multiply reflected responses to the initial incident field also apparently originate from mirror images of the virtual source, all located along the line $z = z_{VS} + x/a$ (see Figure 4.1). We derived these responses with the method of stationary phase, hence they are free of artefacts. We emphasize that the stationary phase analysis is not essential for the method, but it is used here because wave fields obey simple analytical expressions.

4.3.5 Iterative process

We now discuss an iterative scheme, which uses the (k-1)th iteration of the reflection response $p_{k-1}^-(\mathbf{x}, t)$ to create the kth iteration of the incident field $p_k^+(\mathbf{x}, t)$. The objective is to iteratively update the incident field in such a way that, within the upper and lower solid black lines shown in Figure 4.4, the field becomes anti-symmetric in time. The meaning of this criterion will be evident in the next section, where we show how to reconstruct $G(\mathbf{x}, \mathbf{x}_{VS}, t)$. The method requires a combination of time reversal and windowing and the kth iteration of the incident field is defined by

$$p_k^+(\mathbf{x}, t) = p_0^+(\mathbf{x}, t) - w(\mathbf{x}, t) p_{k-1}^-(\mathbf{x}, -t), \quad \text{for } \mathbf{x} \text{ at } z = 0, \tag{4.5}$$

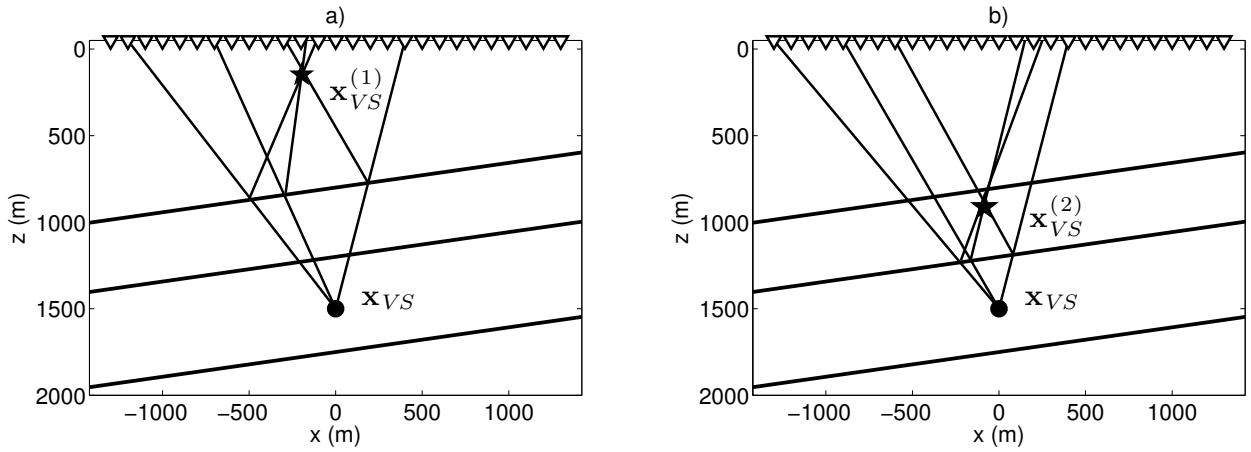

Figure 4.5: Analysis of the response of the first and second reflectors to the initial incident wave field $p_0^+(\mathbf{x}, t)$. a) Stationary rays for different receivers. The response of the first reflector seems to originate from $\mathbf{x}_{VS}^{(1)}$. b) Stationary rays for different receivers. The response of the second reflector seems to originate from $\mathbf{x}_{VS}^{(2)}$.

where the time window $w(\mathbf{x}, t)$ is defined by equation 4.2. The reflection response is then obtained using equation 4.4, which we rewrite here as

$$p_k^-(\mathbf{x}_R, t) = \int_{-\infty}^{\infty} \left[R(\mathbf{x}_R, \mathbf{x}, t) * p_k^+(\mathbf{x}, t) \right]_{z=0} \mathrm{d}x, \tag{4.6}$$

for $\mathbf{x}$ and $\mathbf{x}_R$ at $z = 0$. The first and second iteration of the incident and reflected fields are shown in Figures 4.6 and 4.7, respectively. The events of $p_1^+(\mathbf{x}, t)$ labelled B,C in Figure 4.6 correspond to the events of $p_0^-(\mathbf{x}, t)$ labelled C,B in Figure 4.4 (time-reversed and multiplied by -1, see equation 4.5). Similarly, the events of $p_2^+(\mathbf{x}, t)$ labelled B,C,D in Figure 4.7 correspond to the events of $p_1^-(\mathbf{x}, t)$ labelled F,E,D in Figure 4.6 (time-reversed and multiplied by -1).

For this particular configuration, the kth iteration of the incident field (for $k > 2$) is similar to $p_2^+(\mathbf{x}, t)$ and is composed of four events, as shown in Figure 4.7 for $t < 0$. The events labelled A and D remain unchanged in the iterative process. The other two events (labelled B and C) correspond to $-A_k^{(2)} G_0^d(\mathbf{x}_R, \mathbf{x}_{VS}^{(2)}, -t) * s(t)$ and $-A_k^{(2,1)} G_0^d(\mathbf{x}_R, \mathbf{x}_{VS}^{(2,1)}, -t) * s(t)$, respectively. $\mathbf{x}_{VS}^{(2,1)}$ is the mirror image of $\mathbf{x}_{VS}^{(2)}$ with respect to the first reflector. The coefficient $A_k^{(2)}$ varies at each iteration and is equal to the partial sum of the geometric series

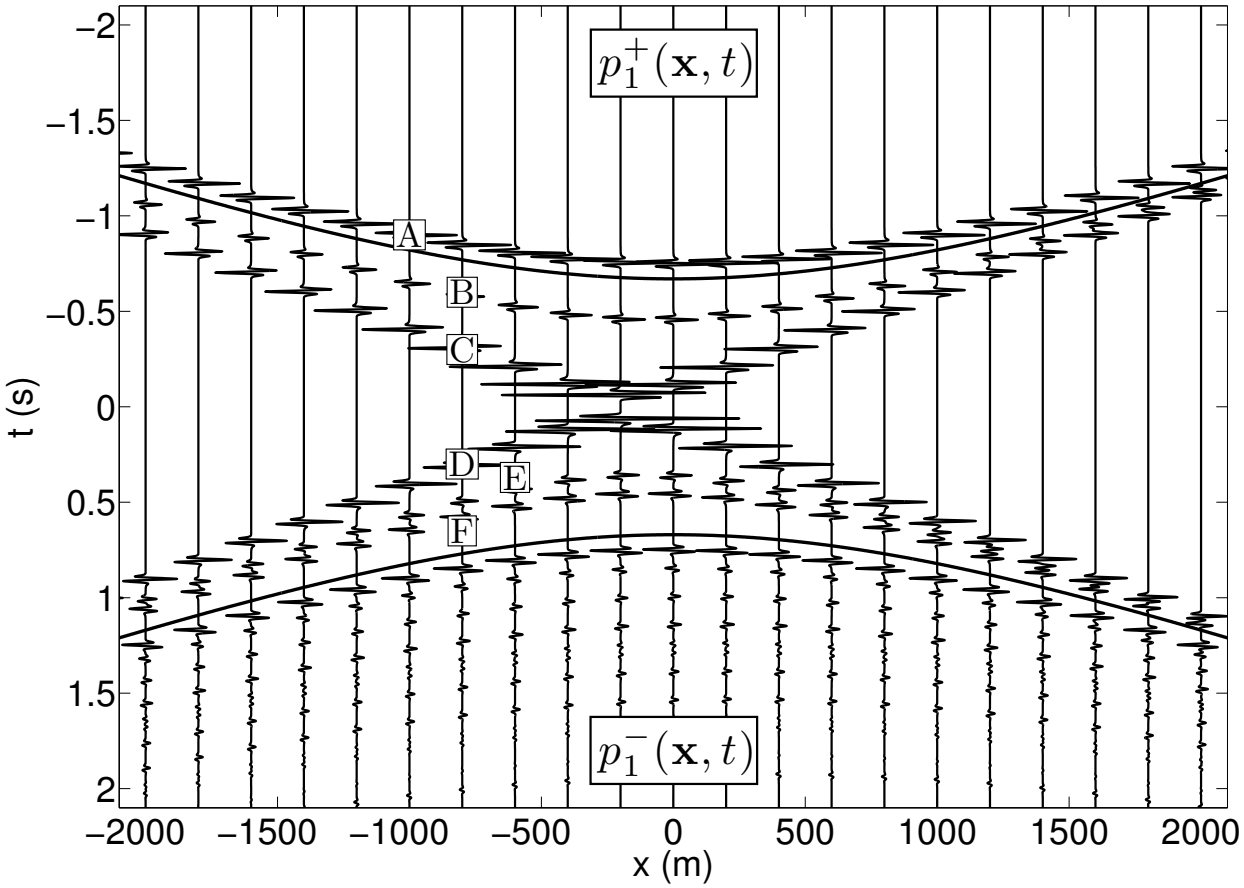

Figure 4.6: First iteration of the incident wave field ($t < 0$) and its reflection response ($t > 0$), both measured at $z = 0$. The labels A−F identify the first six events in the total field. We show the reflection response only until 2 s.

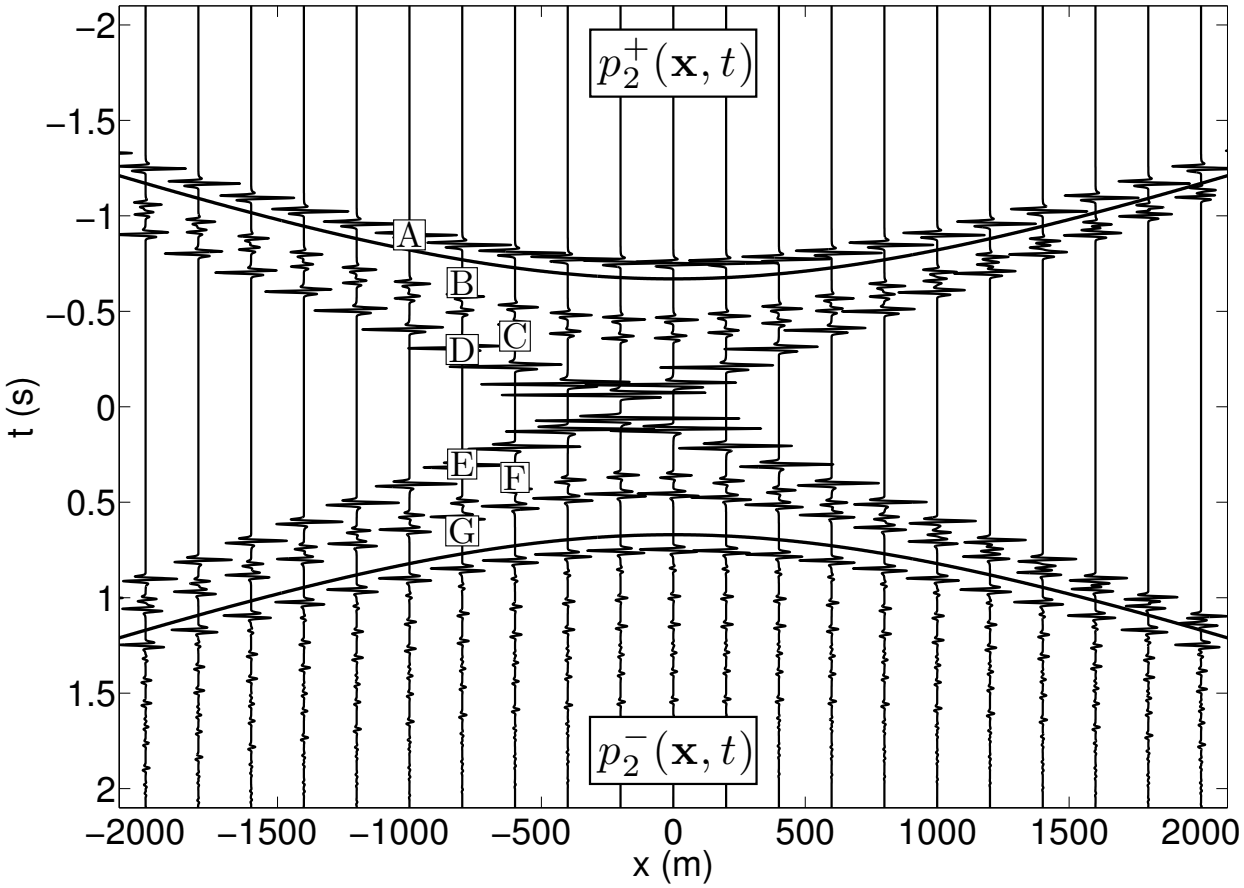

Figure 4.7: Second iteration of the incident wave field ($t < 0$) and its reflection response ($t > 0$), both measured at $z = 0$. The labels A−G identify the first seven events in the total field. We show the reflection response only until 2 s.

$b + by + by^2 + by^3 + by^4 + \cdots + by^k$ where $b = \tau_1^+ r_2 \tau_1^-$ and $y = r_1^2$. The sum of the series converges because $y < 1$ and yields

$$\sum_{k=0}^{\infty} by^k = \frac{b}{1-y} = r_2, \tag{4.7}$$

where we used that $1 - r_1^2 = \tau_1^- \tau_1^+$. The coefficient $A_k^{(2,1)}$ of the third event (labelled C in Figure 4.7) is equal to $-r_1 A_k^{(2)}$ and, hence, it converges to $-r_1 r_2$. Figure 4.8 shows the thirtieth iteration and, within the solid black lines, the wave field is antisymmetric in time. This is the result we predicted when we described the iterative method; in fact, the antisymmetry was the design criterion for the iterative scheme. Wapenaar et al. (2012a) show that, for their simple configuration with one dipping layer, convergence is reached after one iteration.

4.3.6 Green's function reconstruction from the virtual source

After showing that the method converges to the desired result, we define $p_k(\mathbf{x}, t)$ as the superposition of the kth version of the incident and reflected wave fields: $p_k(\mathbf{x}, t) = p_k^+(\mathbf{x}, t) + p_k^-(\mathbf{x}, t)$. Figures 4.4, 4.6, 4.7 and 4.8 show $p_k(\mathbf{x}, t)$ at $z = 0$ for $k = 0, 1, 2,$ and 30, respectively. For brevity, we define $p(\mathbf{x}, t) = p_{30}(\mathbf{x}, t)$. We remind the reader that, within the solid black lines, the total field at $z = 0$ is antisymmetric in time and this particular feature was the design criterion for the iterative scheme. Consequently, if we sum the total field and its time-reversed version, i.e., $p(\mathbf{x}, t) + p(\mathbf{x}, -t)$, all events inside the time window cancel each other, as shown in Figure 4.9. Note that $p(\mathbf{x}, t) + p(\mathbf{x}, -t)$ also obeys the wave equation because we consider a lossless medium. The causal part of this superposition corresponds to $p^-(\mathbf{x}, t) + p^+(\mathbf{x}, -t)$ and the anti-causal part is equal to $p^+(\mathbf{x}, t) + p^-(\mathbf{x}, -t)$, as shown in Figure 4.9 for $t > 0$ and $t < 0$, respectively. From a physical point of view, time-reversal changes the propagation direction. Hence, it follows that the causal part propagates upward at $z = 0$ and the anti-causal part propagates downward at $z = 0$. According to our theory (Wapenaar et al., 2013a), the causal and anti-causal parts of Figure 4.9 are proportional to $G(\mathbf{x}, \mathbf{x}_{VS}, t)$ and $G(\mathbf{x}, \mathbf{x}_{VS}, -t)$ for $z = 0$, respectively. This can be understood with the

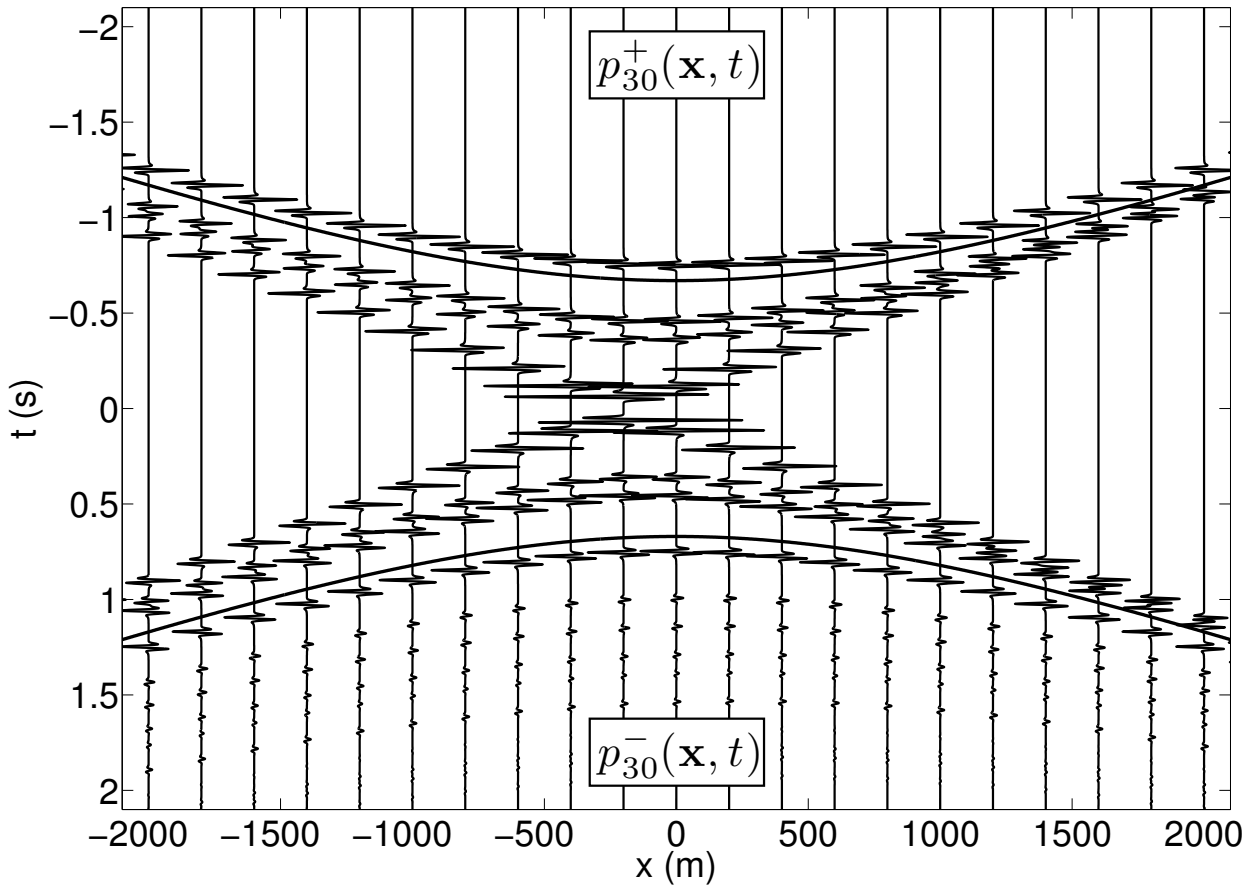

Figure 4.8: Thirtieth iteration of the incident wave field ($t < 0$) and its reflection response ($t > 0$), both measured at $z = 0$. Within the solid black lines, the total field is antisymmetric in time and this particular feature was the design criterion for the iterative scheme. The method has converged to the final result.

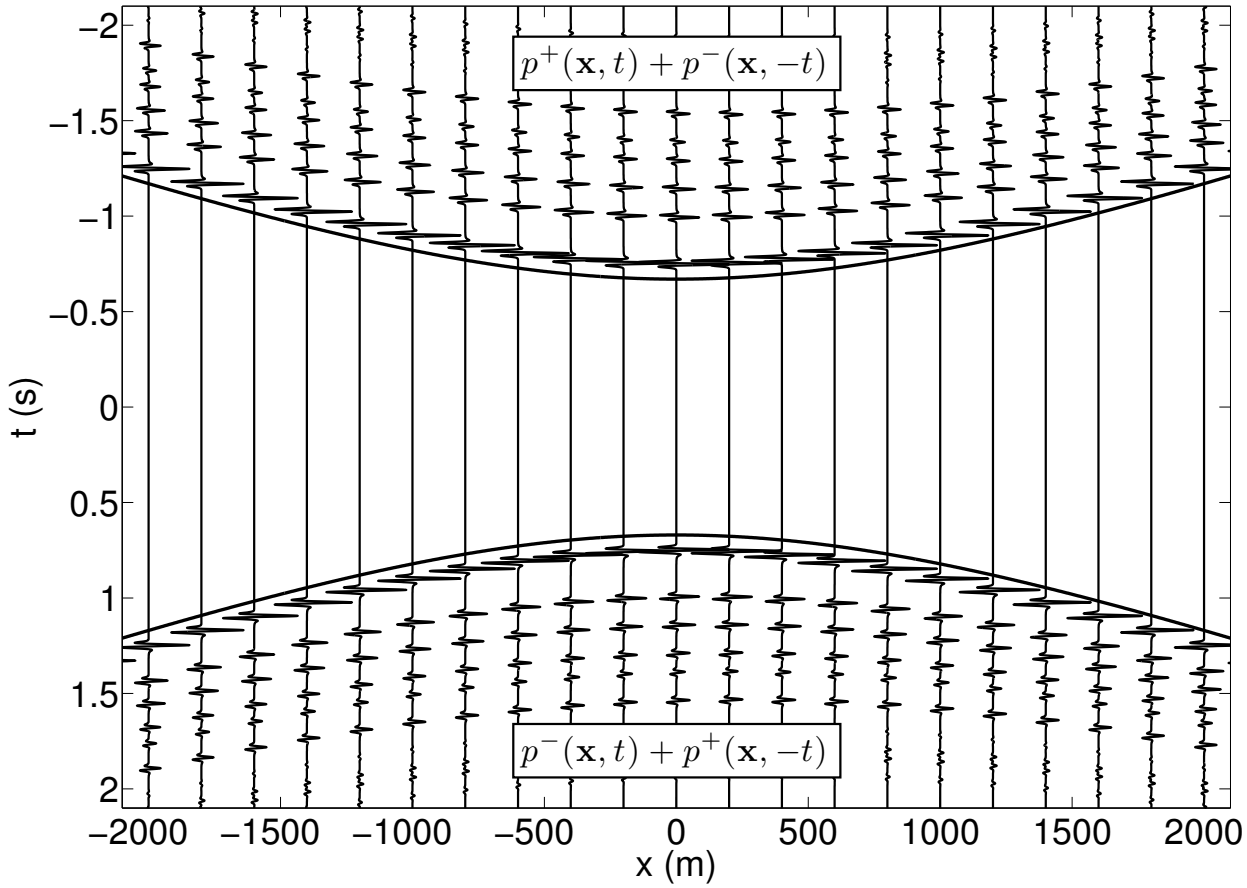

Figure 4.9: Thirtieth iteration. Superposition of the total field and its time-reversed version after the method has converged.

following heuristic derivation. The first event of the causal part of Figure 4.9 has the same arrival time as the direct arrival of the response to the virtual source at $\mathbf{x}_{VS}$ (Figure 4.3). If we combine this last observation with the fact that the causal part is upward propagating at $z = 0$, and that the total field obeys the wave equation in the inhomogeneous medium and is symmetric, it can be understood that the total field in Figure 4.9 is proportional to $G(\mathbf{x}, \mathbf{x}_{VS}, t) + G(\mathbf{x}, \mathbf{x}_{VS}, -t)$.

This reasoning does not depend on any particular feature of the configuration used in this analysis and, according to our theory, it indeed holds for more general situations (Wapenaar et al., 2013a). We confirm its validity for the response in Figure 4.9. Following the steps that led to the field shown in Figure 4.9, we find for the causal part that

$$\begin{aligned} &p^-(\mathbf{x}, t) + p^+(\mathbf{x}, -t) \\ &\quad = \tau_1^+\tau_2^+\tau_1^-\tau_2^- \big\{ G_0^d(\mathbf{x}, \mathbf{x}_{VS}, t) \\ &\quad + r_3 G_0^d(\mathbf{x}, \mathbf{x}_{VS}^{(4)}, t) - r_1 r_2 G_0^d(\mathbf{x}, \mathbf{x}_{VS}^{(5)}, t) \\ &\quad - r_2 r_3 G_0^d(\mathbf{x}, \mathbf{x}_{VS}^{(6)}, t) - r_1 r_2 r_3 G_0^d(\mathbf{x}, \mathbf{x}_{VS}^{(7)}, t) \\ &\quad - r_2(r_1^2 r_2 - r_3^2) G_0^d(\mathbf{x}, \mathbf{x}_{VS}^{(8)}, t) \ldots \big\} * s(t), \end{aligned} \tag{4.8}$$

with the virtual source position and its mirror images shown in Figure 4.1. For the configuration of Figure 4.1, expression 4.8 is proportional to the wave field $G(\mathbf{x}, \mathbf{x}_{VS}, t) * s(t)$ originated from the virtual source and recorded at the surface (with $\tau_1^+\tau_2^+/\rho_3$ as the coefficient of proportionality). The directly modelled response to the virtual source is shown in Figure 4.2 and matches the causal part of the field shown in Figure 4.9. These two wave fields are superposed in Figure 4.10. This is also illustrated in Figure 4.11, where we superposed the traces $(\tau_1^+\tau_2^+/\rho_3)G(\mathbf{x}_{R0}, \mathbf{x}_{VS}, t) * s(t)$ and $p^-(\mathbf{x}_{R0}, t) + p^+(\mathbf{x}_{R0}, -t)$, where $\mathbf{x}_{R0} = (0, 0)$. For the total wave field, we obtain

$$p(\mathbf{x}, t) + p(\mathbf{x}, -t) = \frac{\tau_1^+\tau_2^+}{\rho_3} G_h(\mathbf{x}, \mathbf{x}_{VS}, t) * s(t), \tag{4.9}$$

where $G_h(\mathbf{x}, \mathbf{x}_{VS}, t) = G(\mathbf{x}, \mathbf{x}_{VS}, t) + G(\mathbf{x}, \mathbf{x}_{VS}, -t)$.

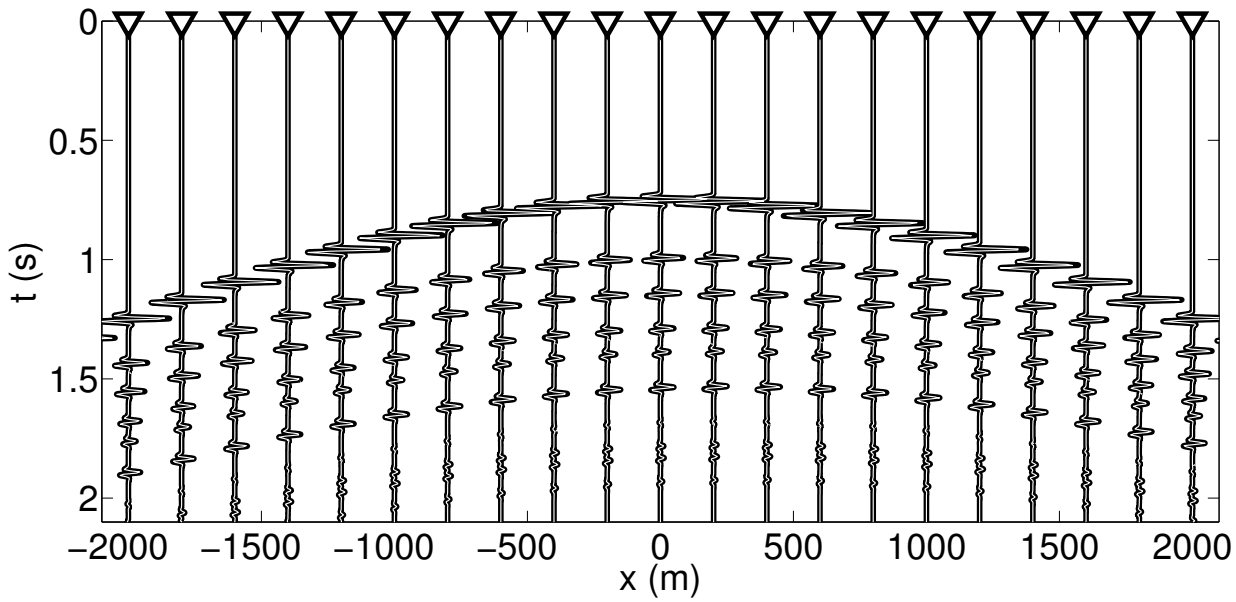

Figure 4.10: Superposition of the total field originated by a real source located at $\mathbf{x}_{VS}$, multiplied by $\tau_1^+\tau_2^+/\rho_3$, (black line) and the wave field reconstructed by the iterative scheme (white line). The two wave fields match perfectly.

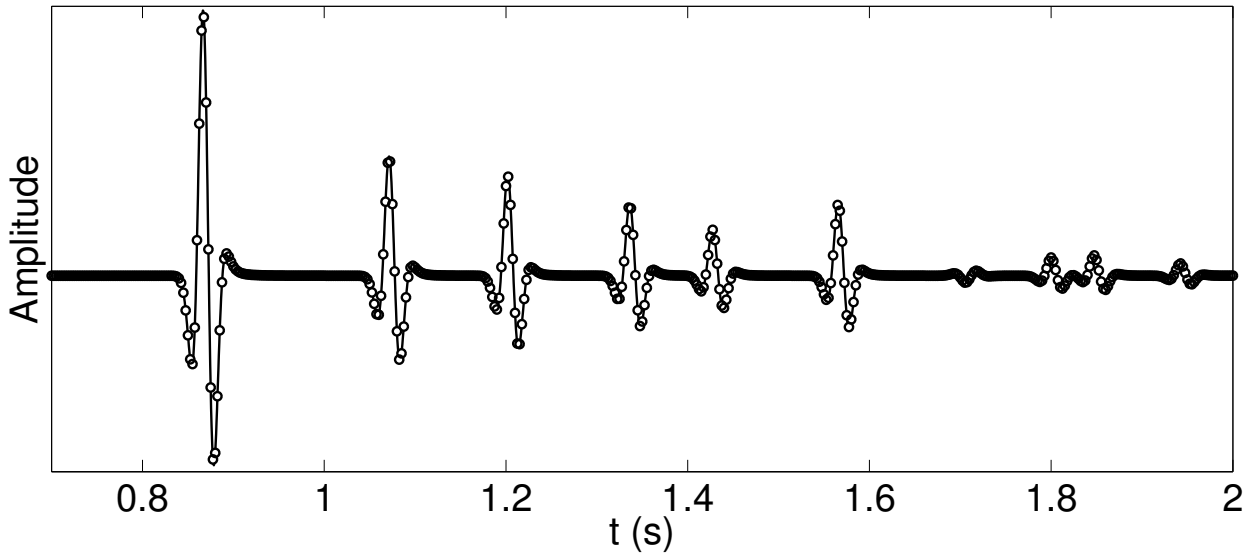

Figure 4.11: Superposition of $(\tau_1^+\tau_2^+/\rho_3)G(\mathbf{x}_{R0}, \mathbf{x}_{VS}, t) * s(t)$ (solid line) and $p^-(\mathbf{x}_{R0}, t) + p^+(\mathbf{x}_{R0}, -t)$ (black circles) for $\mathbf{x}_{R0} = (0, 0)$. The two traces match perfectly.

Note that $G(\mathbf{x}, \mathbf{x}_{VS}, -t)$ satisfies the same wave equation as $G(\mathbf{x}, \mathbf{x}_{VS}, t)$, i.e., $LG(\mathbf{x}, \mathbf{x}_{VS}, -t) = -\rho_3\delta(\mathbf{x} - \mathbf{x}_{VS})\frac{\partial\delta(-t)}{\partial(-t)} = \rho_3\delta(\mathbf{x} - \mathbf{x}_{VS})\frac{\partial\delta(t)}{\partial t}$. Hence, G_h satisfies the homogeneous equation $LG_h = -\rho_3\delta(\mathbf{x} - \mathbf{x}_{VS})\frac{\partial\delta(t)}{\partial t} + \rho_3\delta(\mathbf{x} - \mathbf{x}_{VS})\frac{\partial\delta(t)}{\partial t} = 0$.

To show the convergence of the proposed method, we compute the energy of $p_k(\mathbf{x}, t) + p_k(\mathbf{x}, -t)$ within the solid black lines as a function of the number of iterations:

$$\text{Energy}(k) = \sum_t \sum_x w(\mathbf{x}, t) \left[p_k(\mathbf{x}, t) + p_k(\mathbf{x}, -t)\right]^2 . \tag{4.10}$$

This quantity is shown in Figure 4.12 and the energy inside the time window clearly converges to zero, as confirmed by Figure 4.9. Note that this procedure is expected to converge because in each iteration the reflected energy is smaller than the incident energy. We consider the proposed method as a correction scheme that minimizes the energy within the region where the time window $w(\mathbf{x}, t)$ equals 1.

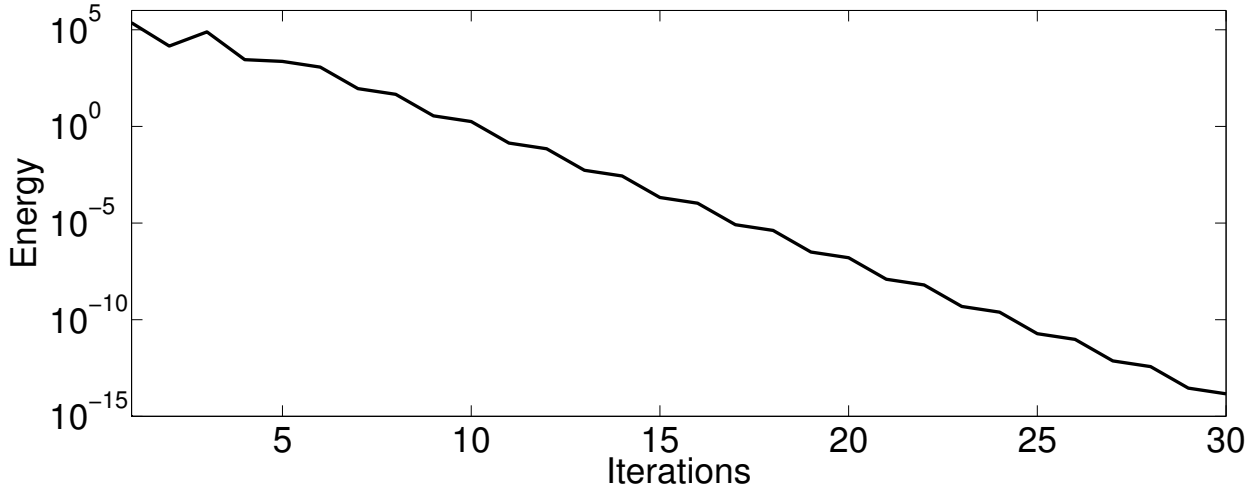

Figure 4.12: Energy of $p_k(\mathbf{x}, t) + p_k(\mathbf{x}, -t)$ within the region where the time window $w(\mathbf{x}, t)$ equals 1 versus number of iterations k. A logarithmic scale (base 10) is used for the Y-axis.

4.4 Wave field decomposition

We first apply a simple source-receiver reciprocity argument, $G(\mathbf{x}_{VS}, \mathbf{x}, t) * s(t) = G(\mathbf{x}, \mathbf{x}_{VS}, t) * s(t)$, and define $G(\mathbf{x}_{VS}, \mathbf{x}, t) * s(t)$ as the wave field originating from sources at the surface and observed by a virtual receiver located at $\mathbf{x}_{VS}$. Following this reasoning, the wave field

in Figure 4.2 can be interpreted as the response recorded at the location $\mathbf{x}_{VS}$, indicated by the black dot in Figure 4.1, due to sources indicated by the white triangles.

To build an image of the reflectors, it is necessary to decompose the total Green's function at the virtual receiver located at $\mathbf{x}_{VS}$ into its downgoing and upgoing component, $G^+(\mathbf{x}_{VS}, \mathbf{x}, t) * s(t)$ and $G^-(\mathbf{x}_{VS}, \mathbf{x}, t) * s(t)$, respectively. These wave fields are illustrated in Figure 4.13. To perform this decomposition, we consider a variant of the iterative scheme, in which the subtraction in equation 4.5 is replaced by an addition (Wapenaar et al., 2011a):

$$q_k^+(\mathbf{x}, t) = q_0^+(\mathbf{x}, t) + w(\mathbf{x}, t) q_{k-1}^-(\mathbf{x}, -t), \quad \text{for } \mathbf{x} \text{ at } z = 0, \tag{4.11}$$

where the time window $w(\mathbf{x}, t)$ is defined by equation 4.2. Note that the 0th iteration of the downgoing field $q_0^+(\mathbf{x}, t)$ is equal to $p_0^+(\mathbf{x}, t)$. As in the previous section, the reflection response is then obtained using equation 4.6, which we rewrite here as

$$q_k^-(\mathbf{x}_R, t) = \int_{-\infty}^{\infty} \left[R(\mathbf{x}_R, \mathbf{x}, t) * q_k^+(\mathbf{x}, t) \right]_{z=0} dx, \quad \text{for } z_R = 0. \tag{4.12}$$

After convergence, we define two additional wave fields: $p_{sym}(\mathbf{x}, t) = p(\mathbf{x}, t) + p(\mathbf{x}, -t)$ and $p_{asym}(\mathbf{x}, t) = q(\mathbf{x}, t) - q(\mathbf{x}, -t)$ (Wapenaar et al., 2012b).

Finally, by combining the wave fields $p_{sym}(\mathbf{x}, t)$ and $p_{asym}(\mathbf{x}, t)$ in two different ways, the Green's function at $\mathbf{x}_{VS}$ is decomposed into downgoing and upgoing fields, according to

$$G^+(\mathbf{x}_{VS}, \mathbf{x}, t) * s(t) = \frac{1}{2} \left\{ p_{sym}(\mathbf{x}, t) - p_{asym}(\mathbf{x}, t) \right\}, \quad \text{for } t \geq 0, \tag{4.13}$$

and

$$G^-(\mathbf{x}_{VS}, \mathbf{x}, t) * s(t) = \frac{1}{2} \left\{ p_{sym}(\mathbf{x}, t) + p_{asym}(\mathbf{x}, t) \right\}, \quad \text{for } t \geq 0. \tag{4.14}$$

The decomposition of the wave field observed at the virtual receiver located at $\mathbf{x}_{VS}$ (Figure 4.10) is shown in Figure 4.14. The top panel corresponds to the downward propagating Green's function $G^+(\mathbf{x}_{VS}, \mathbf{x}, t) * s(t)$ and the bottom panel shows the upward propagating Green's function $G^-(\mathbf{x}_{VS}, \mathbf{x}, t) * s(t)$.

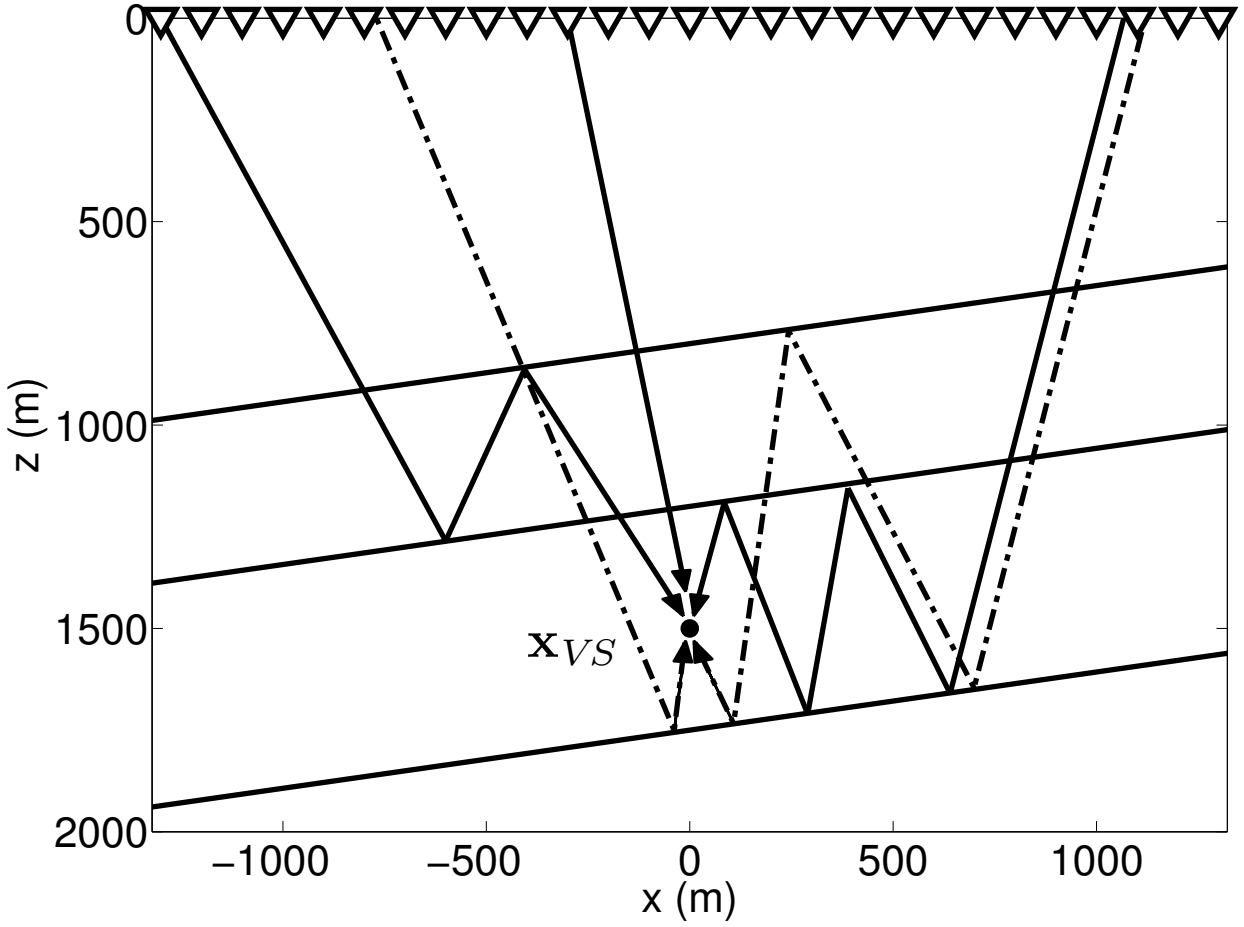

Figure 4.13: Total wave field at the virtual receiver located at $\mathbf{x}_{VS}$. The solid black rays correspond to $G^{+}(\mathbf{x}_{VS}, \mathbf{x}, t) * s(t)$. The dashed black rays correspond to $G^{-}(\mathbf{x}_{VS}, \mathbf{x}, t) * s(t)$.

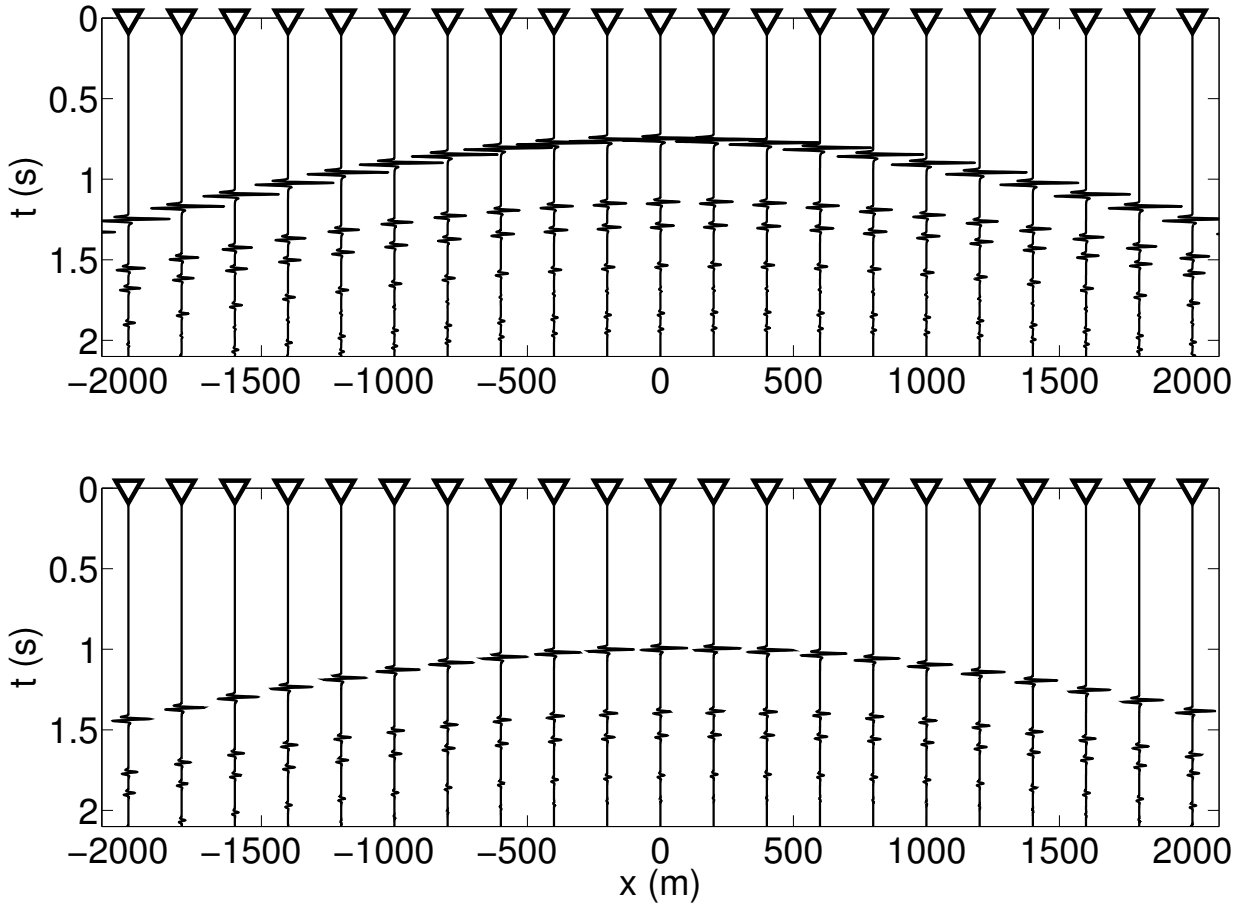

Figure 4.14: Upgoing and downgoing wave field decomposition. Top panel: $G^+(\mathbf{x}_{VS}, \mathbf{x}, t) * s(t)$. Bottom panel: $G^-(\mathbf{x}_{VS}, \mathbf{x}, t) * s(t)$.

4.5 Imaging

In this section, we use the decomposed wave fields to create a ghost-free image of the subsurface. This image is constructed using either simple crosscorrelations or multi-dimensional deconvolution and is compared to standard prestack migration.

4.5.1 Standard prestack imaging

We start by creating a reference image using a standard imaging technique (Claerbout, 1985). Standard prestack imaging and many other seismic imaging algorithms rely on the single scattering assumption. This implies that the recorded wave fields do not include internal multiples (waves bouncing multiple times between reflectors before reaching the receivers). When multiple reflections are present in the data, the imaging algorithm incorrectly interprets them as ghost reflectors. This initial image is shown in Figure 4.15a and the arrows indicate some of the ghost reflectors present in this standard image. Also, note that the amplitudes do not agree with the correct reflection coefficients.

4.5.2 Imaging with crosscorrelation

If we repeat the decomposition process described in the previous section for virtual receivers $\mathbf{x}_{VS}$ located on many depth levels $z = z_i$ (e.g. the horizontal lines composed of black dots in Figure 4.16), we are able to create a more accurate image of the medium. To perform this task, we compute the crosscorrelation function C

$$C(\mathbf{x}_{VS}, \mathbf{x}_{VS}, t) = \int_{-\infty}^{\infty} \left[G^{-}(\mathbf{x}_{VS}, \mathbf{x}, t) * G^{+}(\mathbf{x}_{VS}, \mathbf{x}, -t) \right]_{z=0} \mathrm{d}x \tag{4.15}$$

at every virtual receiver depth and evaluate the result at $t = 0$. This new image is shown in Figure 4.15b. As in the standard prestack image, the actual reflectors have been reconstructed at the correct spatial location, but now the image is free of internal multiple ghosts. This is an improvement over the previous image, but the retrieved amplitudes still do not agree with the true reflection coefficients. The amplitude of the first two reflectors should have the same magnitude and opposite polarity because $r_2 = -r_1$ (in this particular configu-

ration), but the amplitude of the second reflector is smaller than the first one. Furthermore, the amplitude of the third reflector should be 75% of that of the first reflector ($r_3 = 0.75r_1$), but the image shows that the amplitude of the third reflector is considerably smaller than its expected value.

4.5.3 Imaging with multidimensional deconvolution

Now, we show that multidimensional deconvolution allows us to create an image with more accurate amplitudes. As in imaging with crosscorrelation, we consider a constant depth level $z = z_i$. The Green's functions at this constant depth level are related by

$$G^-(\mathbf{x}_r, \mathbf{x}_s, t) = \int_{-\infty}^{\infty} \left[R(\mathbf{x}_r, \mathbf{x}, t) * G^+(\mathbf{x}, \mathbf{x}_s, t)\right]_{z=z_i} \mathrm{d}x, \tag{4.16}$$

where $R(\mathbf{x}_r, \mathbf{x}, t)$ is the reflection response to downgoing waves at $z = z_i$ of the truncated medium below $z = z_i$, $\mathbf{x}_s$ is at $z = 0$, and $\mathbf{x}_r$ is at $z = z_i$. The truncated medium is equal to the true medium below the depth level $z = z_i$ and is homogeneous above $z = z_i$. Now, the reflectivity $R(\mathbf{x}_r, \mathbf{x}, t)$ can be resolved from equation 4.16 by multidimensional deconvolution (MDD) (Wapenaar et al., 2011b). To achieve this result, we first correlate both sides of equation 4.16 with the downgoing Green's function and integrate over source locations over the acquisition surface:

$$C(\mathbf{x}_r, \mathbf{x}', t) = \int_{-\infty}^{\infty} \left[R(\mathbf{x}_r, \mathbf{x}, t) * \Gamma(\mathbf{x}, \mathbf{x}', t)\right]_{z=z_i} \mathrm{d}x, \quad \text{for } \mathbf{x}_r \text{ and } \mathbf{x}' \text{at } z = z_i, \tag{4.17}$$

where C is the crosscorrelation function (as in the previous section, but with not-coinciding coordinates)

$$C(\mathbf{x}_r, \mathbf{x}', t) = \int_{-\infty}^{\infty} \left[G^-(\mathbf{x}_r, \mathbf{x}_s, t) * G^+(\mathbf{x}', \mathbf{x}_s, -t)\right]_{z_s=0} \mathrm{d}x_s, \tag{4.18}$$

and Γ is the point-spread function (van der Neut et al., 2011)

$$\Gamma(\mathbf{x}, \mathbf{x}', t) = \int_{-\infty}^{\infty} \left[G^+(\mathbf{x}, \mathbf{x}_s, t) * G^+(\mathbf{x}', \mathbf{x}_s, -t)\right]_{z_s=0} \mathrm{d}x_s. \tag{4.19}$$

We resolve $R(\mathbf{x}_r, \mathbf{x}, t)$ for different depth levels $z = z_i$ and many virtual source locations, as shown by the horizontal lines composed of black dots in Figure 4.16, and evaluate the result

at $t = 0$ and $x_r = x$. Figure 4.15c shows the final result of the imaging process. As in the previous image, the reflectors have been imaged at the correct spatial locations, but now the retrieved amplitudes agree with the true reflection coefficients. The amplitudes of the first two reflectors have similar magnitude and opposite polarity and the amplitude of the third reflector is roughly 75% of that of the first reflector. The difference in the amplitudes between the two images is clearly shown in Figure 4.15d, where we compare the reflectivity at $x = 0$ m retrieved by standard prestack migration, crosscorrelation, and multidimensional deconvolution with the true reflectivity. Multidimensional deconvolution acknowledges the multi-dimensional nature of the seismic wave field, hence the internal multiples contribute to the restoration of the amplitudes of the reflectors.

4.6 Conclusions

We discussed a generalization to two dimensions of the model-independent wave field reconstruction method of Broggini et al. (2011; 2012b). Unlike the one-dimensional method, which uses the reflection response only, the proposed multi-dimensional extension requires, in addition to the reflection response, independent information about the first arrivals. This method can be easily extended to three dimensions.

The proposed data-driven procedure yields the Green's function (including correct internal multiples) originating from a virtual source, without needing a receiver at the virtual source location and without needing detailed knowledge of the medium, as shown in Figure 4.10. The method requires (1) the direct arriving wave front at the surface originated from a virtual source in the subsurface, and (2) the reflection impulse responses for all source and receiver positions at the surface. The direct arriving wave front can be obtained by modelling in a macro model, from microseismic events (Artman et al., 2010), from borehole check shots, or directly from the data by the CFP method (Berkhout, 1997; Haffinger and Verschuur, 2012; Thorbecke, 1997) when the virtual source is located at an interface. The required reflection responses are obtained from conventional seismic reflection data after removal of the multiples due to the free-surface and after deconvolution for the source wavelet

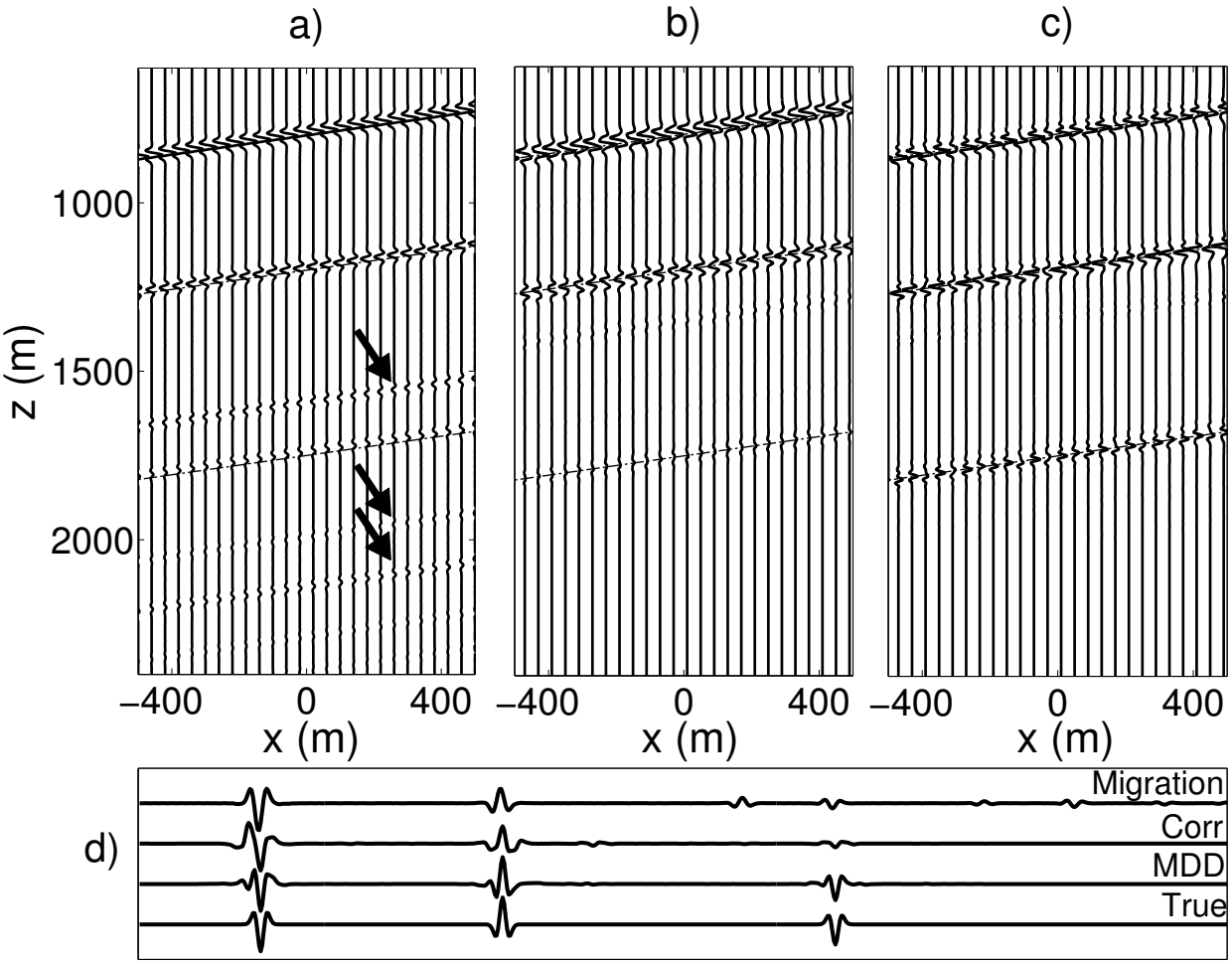

Figure 4.15: a) Image of the reflectors obtained with standard prestack migration. The arrows indicate ghost images. b) Image of the reflectors obtained with the crosscorrelation function C. c) Image of the reflectors obtained with multidimensional deconvolution. d) Comparison of the reflectivity at $x = 0$ m retrieved by standard prestack migration, crosscorrelation, and multidimensional deconvolution with the true reflectivity (from top to bottom).

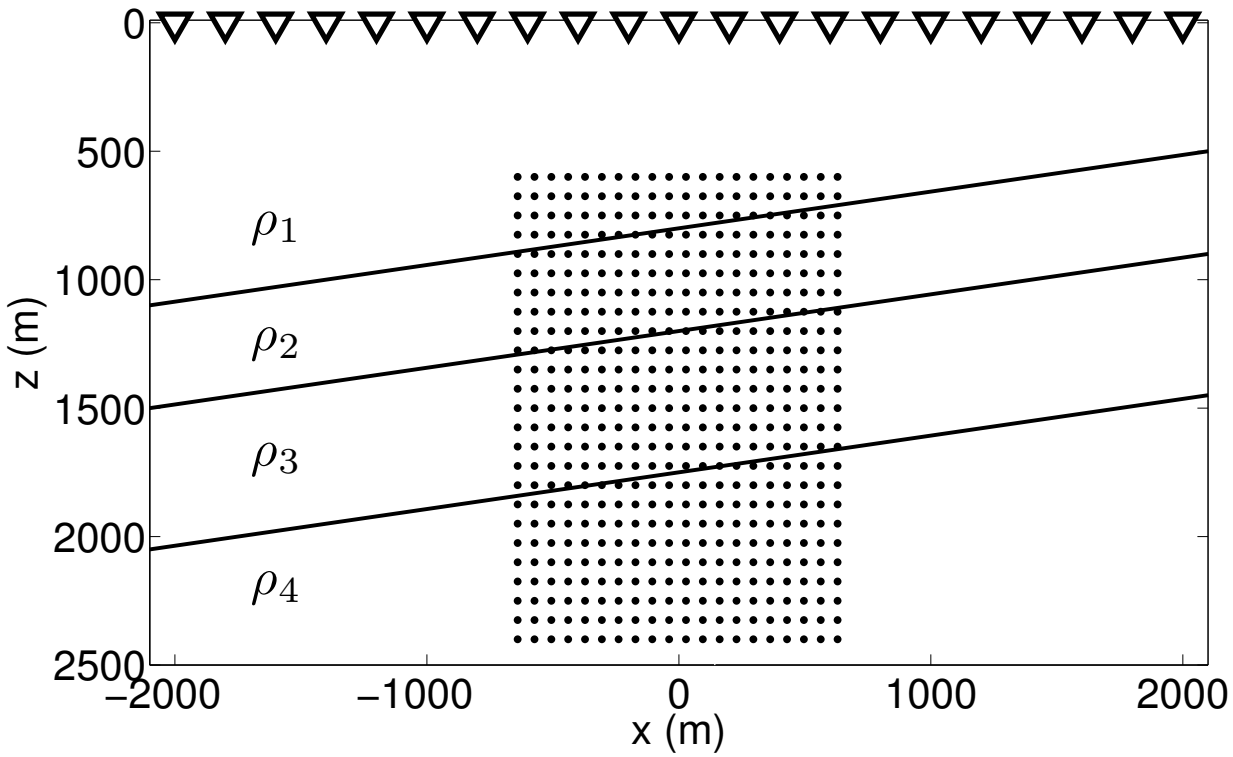

Figure 4.16: The black dots correspond to various virtual receiver locations $\mathbf{x}_{VS}$. Virtual receivers located on a constant depth level $z = z_i$ are used to resolve $[R(\mathbf{x}_r, \mathbf{x}, t)]_{z=z_i}$.

(Amundsen, 2001; van Groenestijn and Verschuur, 2009; Verschuur et al., 1992).

For a simple configuration with planar dipping reflectors, the stationary-phase analysis gives a better understanding of the two-dimensional iterative scheme and confirms that the method converges to the virtual-source response. This reconstruction is handled by the actual medium through the reflection data measured at the surface (which includes all the information about the medium itself).

A variant of the iterative scheme allows the decomposition of the reconstructed Green's function into its downgoing and upgoing components. These wave fields are then used to create different images of the medium with crosscorrelation and multidimensional deconvolution. These two techniques show an improvement over standard imaging and allow us to construct an image that is not affected by ghost images of the reflectors. Additionally, multidimensional deconvolution yields an image whose amplitudes agree with the correct reflection responses. This is due to the deconvolution process that correctly handles the internal multiples and retrieves the correct amplitudes of the primary reflections. We emphasize that, for the crosscorrelation and multidimensional deconvolution results, the imaging process does not require any more knowledge of the medium parameters than standard primary imaging schemes (which use a macro model).

The iterative scheme is equivalent to an integral equation. Inserting equation 4.5 into equation 4.6 and assuming convergence (setting $p_k^- = p_{k-1}^-$ and then dropping the subscript k) gives

$$\begin{aligned} p^-(\mathbf{x}_R, t) = &\int_{-\infty}^{\infty} \left[R(\mathbf{x}_R, \mathbf{x}, t) * p_0^+(\mathbf{x}, t)\right]_{z=0} \mathrm{d}x \\ &- \int_{-\infty}^{\infty} \left[R(\mathbf{x}_R, \mathbf{x}, t) * \left\{w(\mathbf{x}, t) p^-(\mathbf{x}, -t)\right\}\right]_{z=0} \mathrm{d}x. \end{aligned} \tag{4.20}$$

This equation is the two-dimensional extension of the Marchenko equation in inverse scattering (Agranovich and Marchenko, 1963). The iterative scheme we propose thus implicitly solves the inverse scattering problem. A proof for more general models is given by Wapenaar

et al. (2013a).

4.7 Acknowledgments

The authors thank the members of the Center for Wave Phenomena for their constructive comments. This work was supported by the sponsors of the Consortium Project on Seismic Inverse Methods for Complex Structures at the Center for Wave Phenomena and the Netherlands Research Centre for Integrated Solid Earth Science (ISES).

CHAPTER 5

RELATIONSHIP BETWEEN ONE-SIDED AND TWO-SIDED GREEN'S FUNCTION REPRESENTATIONS

Filippo Broggini[1,2], Kees Wapenaar[3], Roel Snieder[1], and Evert Slob[3]

In preparation for *Geophysical Journal International*

5.1 Abstract

The Green's function, defined as the response recorded at the acquisition surface for a source located in the interior of the subsurface, is a combination of the downgoing and upgoing wave fields needed to reconstruct an image of the discontinuities inside the earth. Two-sided Green's function representations require measurement on the full boundary enclosing the domain of interest and allow us to retrieve the Green's function originating from any location inside the medium. Practical constraints usually prevent the placement of receivers at depth inside the earth; hence standard imaging techniques need to apply approximations to two-sided Green's function representations to construct an image of the subsurface. Recently-developed one-sided representations need data acquired on only one side of the boundary enclosing the region of interest. These theorems present a practical advantage because they remove the physical constraints of having receivers at depth; hence one-sided representations do not require the approximations needed by two-sided techniques. In this paper, we show the connection between one-sided and two-sided Green's function representations.

[1]Center for Wave Phenomena, Colorado School of Mines, Golden, CO 80401, USA
[2]Principal researcher and author
[3]Delft University of Technology, Department of Geoscience and Engineering, Delft, The Netherlands

5.2 Introduction

Green's function representations requiring measurement on a closed boundary surrounding an inhomogeneous medium allow us to retrieve the Green's function originating from any location inside the medium itself (Aki and Richards, 2002). Techniques based on these representations can be used to create an image of the structures inside the Earth. Unfortunately, because of practical constraints, we are unable to place receivers along a closed boundary inside the Earth. Since measurements are not available on the full closed boundary, standard imaging techniques need to apply approximations to two-sided Green's function representations to construct an image of the subsurface. Because these equations require measurements on a closed boundary, we refer to these equations as *two-sided* integral equations.

Pioneering work of Rose has shown the connection between one-dimensional autofocusing and the Marchenko equation (Aktosun and Rose, 2002; Rose, 2001, 2002a,b). We have extended this connection to one-dimensional Green's function retrieval by combining the time-reversed focusing wave field with its reflection response (Broggini and Snieder, 2012; Broggini et al., 2012b). Wapenaar et al. (2013a, 2012a, 2013b), and Broggini et al. (2012a) introduce an integral equation that allows one to reconstruct from reflection data at the surface the Green's function propagating from a location inside a medium to receivers located at the acquisition surface. Because reflection data are needed on only one side of the medium, we refer to this equation as *one-sided* integral equation. Following an insight by Lamb (1980), Wapenaar et al. (2013a) show that a *focusing solution* of the source-free wave equation is required to prove the validity of the one-sided integral equation and, additionally, discuss an iterative scheme to solve this integral equation.

The techniques introduced by one-side integral equations are elegant, but their derivations, based on the Marchenko equations, restrict their application to a limited number of problems. Here we show that techniques based on one-side representations can be derived from well-known integral equations for Green's function retrieval, known as seismic interferometry in the geophysical community (Bakulin and Calvert, 2006; Schuster, 2009; Wapenaar

and Fokkema, 2006). Since these two-sided equations are applicable to a wide range of problems (Larose et al., 2006; Lobkis and Weaver, 2001), one-sided techniques can, in principle, be extended to a large class of problems as well. In this paper, we present a derivation valid for acoustic waves in lossless media.

5.3 Two-sided integral equation for Green's function retrieval

We introduce the Green's function $G(\mathbf{x}, \mathbf{x}_B, t)$ as a solution to the wave equation $LG = -\rho\delta(\mathbf{x} - \mathbf{x}_B)\frac{\partial\delta(t)}{\partial t}$, with $L = \rho\nabla\cdot(\rho^{-1}\nabla) - c^{-2}\frac{\partial^2}{\partial t^2}$. The mass density and the velocity are denoted by $\rho(\mathbf{x})$ and $c(\mathbf{x})$, respectively. Following de Hoop (1995), the Green's function $G(\mathbf{x}, \mathbf{x}_B, t)$ corresponds to the acoustic pressure measured at $\mathbf{x}$ due to an impulsive point source of volume injection rate at $\mathbf{x}_B$. We define the spatial coordinate $\mathbf{x}$ as $\mathbf{x} = (\mathbf{x}_H, x_3)$, where $\mathbf{x}_H = (x_1, x_2)$ is the horizontal coordinate vector and x_3 the vertical coordinate. The positive direction of the x_3-axis points downward. The Green's function $G(\mathbf{x}, \mathbf{x}_B, t)$ can be decomposed in its downgoing $G^+(\mathbf{x}, \mathbf{x}_B, t)$ and upgoing $G^-(\mathbf{x}, \mathbf{x}_B, t)$ components. In this paper, these two wave fields are pressure-normalized (Ursin et al., 2012). Using the Fourier convention $f(\mathbf{x}, \omega) = \int_{-\infty}^{+\infty} f(\mathbf{x}, t)\exp(-j\omega t)dt$, the frequency domain Green's function $G(\mathbf{x}, \mathbf{x}_B, \omega)$ obeys the equation $LG = -j\omega\rho\delta(\mathbf{x}-\mathbf{x}_B)$, with $L = \rho\nabla\cdot(\rho^{-1}\nabla)+\omega^2/c^2$. Here, j is the imaginary unit and ω denotes the angular frequency. To keep a simple notation, we use the same symbol for the time-domain version of a function as for its frequency-domain counterpart.

Our starting point is the acoustic representation of Green's functions in the frequency domain given by equation 18 in Wapenaar and Fokkema (2006):

$$\begin{aligned}&\chi_{\mathbb{D}}(\mathbf{x}_A)G(\mathbf{x}_A, \mathbf{x}_B, \omega) + \chi_{\mathbb{D}}(\mathbf{x}_B)G^*(\mathbf{x}_B, \mathbf{x}_A, \omega) \\ &= \oint_{\partial\mathbb{D}} \frac{-1}{j\omega\rho(\mathbf{x})}\left\{G^*(\mathbf{x}, \mathbf{x}_A, \omega)\partial_i G(\mathbf{x}, \mathbf{x}_B, \omega) - \partial_i G^*(\mathbf{x}, \mathbf{x}_A, \omega)G(\mathbf{x}, \mathbf{x}_B, \omega)\right\} n_i \mathrm{d}^2\mathbf{x},\end{aligned} \tag{5.1}$$

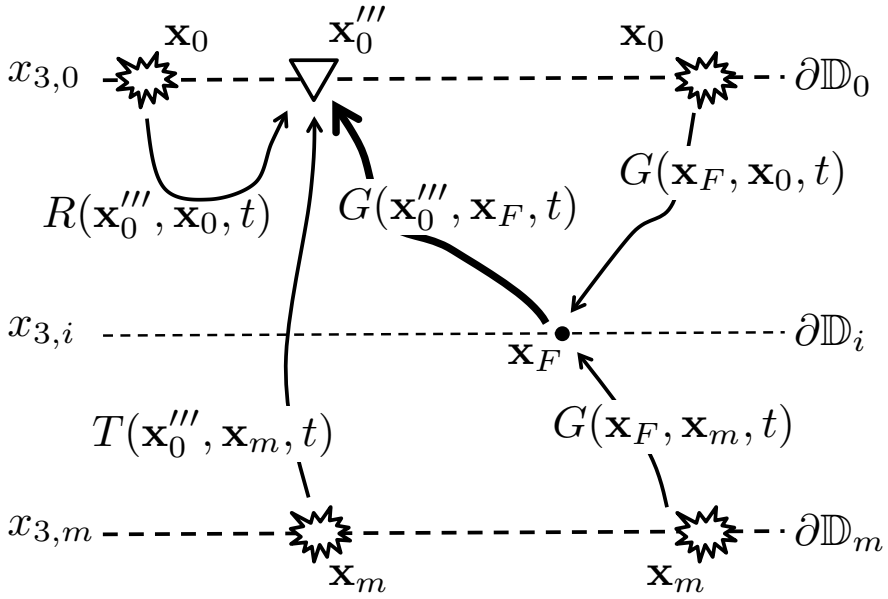

Figure 5.1: Definition of the variables used in equation 5.3.

where $*$ indicates complex-conjugation and $\chi_{\mathbb{D}}(\mathbf{x})$ is the characteristic function for the domain $\mathbb{D}$, defined as

$$\chi_{\mathbb{D}}(\mathbf{x}) = \begin{cases} 1 & \text{for } \mathbf{x} \in \mathbb{D} \\ \frac{1}{2} & \text{for } \mathbf{x} \in \partial\mathbb{D} \\ 0 & \text{for } \mathbf{x} \in \mathbb{R}^3 \in \setminus \{\mathbb{D} \cup \partial\mathbb{D}\}\,. \end{cases} \tag{5.2}$$

In equation 5.1, ∂_i denotes the partial derivative in the x_i-direction (Einstein's summation convention applies for repeated subscripts) and it acts on $\mathbf{x}$ which corresponds to a receiver location. The term $\dfrac{-1}{j\omega\rho(\mathbf{x})}\partial_i G(\mathbf{x}, \mathbf{x}_B, \omega)$ in equation 5.1 corresponds to the particle velocity recorded at $\mathbf{x}$ due to a monopole source located at $\mathbf{x}_B$. We consider an inhomogeneous lossless medium $\mathbb{D}$ enclosed by the boundary $\partial\mathbb{D}$ with outward point normal vector $\mathbf{n} = (n_1, n_2, n_3)$.

By infinitely extending the sides of the domain $\mathbb{D}$, we can replace the closed surface integral over $\partial\mathbb{D}$ by an integral over two horizontal boundaries $\partial\mathbb{D}_0$ and $\partial\mathbb{D}_m$ at depth $x_3 = x_{3,0}$ and $x_3 = x_{3,m}$, respectively, as shown in Figure 5.1. For this reason, we define equation 5.1 as a two-sided integral equation. In the following, the upper half-space $x_3 < x_{3,0}$ and the lower half-space $x_3 > x_{3,m}$ are homogeneous and their medium parameters do not have

to be the same. The boundaries $\partial\mathbb{D}_0$ and $\partial\mathbb{D}_m$ do not correspond with physical interfaces; hence they do not cause reflection of acoustic waves. With this configuration, the partial derivative ∂_i (acting on $\mathbf{x}$) is along the vertical direction x_3. Next, we take $\mathbf{x}_A$ to be a point $\mathbf{x}_F$ in the interior of $\mathbb{D}$ and take $\mathbf{x}_B$ to be the position $\mathbf{x}_0'''$ of a receiver located just above the surface $\partial\mathbb{D}_0$; see Figure 5.1, where $\mathbf{x}_0''' = (\mathbf{x}_H''', x_{3,0} - \epsilon)$, with $\epsilon \to 0$. The second term on the left-hand side of equation 5.1 disappears because $\chi_{\mathbb{D}}(\mathbf{x}_0''') = 0$ when $\mathbf{x}_0'''$ is outside $\mathbb{D}$. These substitutions reduce expression 5.1 to

$$\begin{aligned} &G(\mathbf{x}_F, \mathbf{x}_0''', \omega) \\ &= \int_{\partial\mathbb{D}_0 \cup \partial\mathbb{D}_m} \frac{-1}{j\omega\rho(\mathbf{x})} \left\{ G^*(\mathbf{x}, \mathbf{x}_F, \omega) \partial_i G(\mathbf{x}, \mathbf{x}_0''', \omega) - \partial_i G^*(\mathbf{x}, \mathbf{x}_F, \omega) G(\mathbf{x}, \mathbf{x}_0''', \omega) \right\} n_i \mathrm{d}^2\mathbf{x} \\ &\equiv I_{\partial\mathbb{D}_0} + I_{\partial\mathbb{D}_m}. \end{aligned} \tag{5.3}$$

$I_{\partial\mathbb{D}_0}$ and $I_{\partial\mathbb{D}_m}$ correspond to the integrals over the top $\partial\mathbb{D}_0$ and bottom $\partial\mathbb{D}_m$ boundaries, respectively.

We start by transforming the two terms inside the integral in equation 5.3 to a single term. To achieve this, we have to analyze separately the integral over the top and bottom boundaries because $\mathbf{x}_0'''$ and $\mathbf{x}_F$ are on different sides with respect to $\partial\mathbb{D}_0$, while they are on the same side with respect to $\partial\mathbb{D}_m$. First, we focus on the integral over the top boundary $\partial\mathbb{D}_0$,

$$I_{\partial\mathbb{D}_0} = \int_{\partial\mathbb{D}_0} \frac{1}{j\omega\rho(\mathbf{x})} \left\{ G^*(\mathbf{x}, \mathbf{x}_F, \omega) \partial_3 G(\mathbf{x}, \mathbf{x}_0''', \omega) - \partial_3 G^*(\mathbf{x}, \mathbf{x}_F, \omega) G(\mathbf{x}, \mathbf{x}_0''', \omega) \right\} \mathrm{d}^2\mathbf{x}, \tag{5.4}$$

where we used that $\partial_i n_i = -\partial_3$ (n_3 points upward at $\partial\mathbb{D}_0$, while x_3 points downward). According to Appendix B.3 of Wapenaar and Berkhout (1989), we can rewrite equation 5.4 (for the integral over $\partial\mathbb{D}_0$) as

$$\begin{aligned} I_{\partial\mathbb{D}_0} = &\int_{\partial\mathbb{D}_0} \frac{2}{j\omega\rho(\mathbf{x})} \left\{ G^+(\mathbf{x}, \mathbf{x}_F, \omega) \right\}^* \partial_3 G^+(\mathbf{x}, \mathbf{x}_0''', \omega) \mathrm{d}^2\mathbf{x} \\ &+ \int_{\partial\mathbb{D}_0} \frac{2}{j\omega\rho(\mathbf{x})} \left\{ G^-(\mathbf{x}, \mathbf{x}_F, \omega) \right\}^* \partial_3 G^-(\mathbf{x}, \mathbf{x}_0''', \omega) \mathrm{d}^2\mathbf{x}, \end{aligned} \tag{5.5}$$

where $G = G^{+} + G^{-}$. Note that equation 5.5 is not exact because the evanescent waves are neglected at the boundary $\partial\mathbb{D}_0$. Furthermore, because the medium above $\partial\mathbb{D}_0$ is homogeneous, the downgoing component of $G(\mathbf{x}, \mathbf{x}_F, \omega)$ is equal to zero; hence $G(\mathbf{x}, \mathbf{x}_F, \omega) = G^{-}(\mathbf{x}, \mathbf{x}_F, \omega)$. This yields

$$I_{\partial\mathbb{D}_0} = \int_{\partial\mathbb{D}_0} \frac{2}{j\omega\rho(\mathbf{x})} \left\{G^{-}(\mathbf{x}, \mathbf{x}_F, \omega)\right\}^{*} \partial_3 G^{-}(\mathbf{x}, \mathbf{x}_0''', \omega) \mathrm{d}^2\mathbf{x}. \tag{5.6}$$

The term $\dfrac{-1}{j\omega\rho(\mathbf{x})}\partial_3 G^{-}(\mathbf{x}, \mathbf{x}_0''', \omega)$ in equation 5.6 corresponds to the vertical component of the particle velocity of the upgoing field recorded at $\mathbf{x}$ due to a monopole source located at $\mathbf{x}_0'''$ just above the boundary $\partial\mathbb{D}_0$, or, via reciprocity, to the acoustic pressure recorded at $\mathbf{x}_0'''$ due to a downward radiating dipole source located at $\mathbf{x}$. Since we deal with pressure-normalized wave fields, we use the last definition and define the reflection response as (Wapenaar et al., 2012a)

$$R(\mathbf{x}_0''', \mathbf{x}, \omega) = \frac{2}{j\omega\rho(\mathbf{x})}\partial_3 G^{-}(\mathbf{x}, \mathbf{x}_0''', \omega), \quad \text{for}\, \mathbf{x} \in \partial\mathbb{D}_0. \tag{5.7}$$

The reflection response is acquired in a seismic experiment where sources and receivers are both located along the acquisition surface at $x_3 = x_{3,0}$. Using this, we rewrite equation 5.6 as

$$I_{\partial\mathbb{D}_0} = \int_{\partial\mathbb{D}_0} R(\mathbf{x}_0''', \mathbf{x}, \omega) G^{*}(\mathbf{x}, \mathbf{x}_F, \omega) \mathrm{d}^2\mathbf{x}, \tag{5.8}$$

where $G(\mathbf{x}, \mathbf{x}_F, \omega) = G^{-}(\mathbf{x}, \mathbf{x}_F, \omega)$.

Next, we analyze the integral over the bottom boundary $\partial\mathbb{D}_m$ in equation 5.3:

$$I_{\partial\mathbb{D}_m} = \int_{\partial\mathbb{D}_m} \frac{-1}{j\omega\rho(\mathbf{x})} \left\{G^{*}(\mathbf{x}, \mathbf{x}_F, \omega)\partial_3 G(\mathbf{x}, \mathbf{x}_0''', \omega) - \partial_3 G^{*}(\mathbf{x}, \mathbf{x}_F, \omega) G(\mathbf{x}, \mathbf{x}_0''', \omega)\right\} \mathrm{d}^2\mathbf{x}, \tag{5.9}$$

where we used that $\partial_i n_i = +\partial_3$ (n_3 points downward at $\partial\mathbb{D}_m$, while x_3 also points downward). As previously mentioned, $\mathbf{x}_0'''$ and $\mathbf{x}_F$ are on the same side with respect to $\partial\mathbb{D}_m$; hence, we can use the same arguments given by Wapenaar and Fokkema (2006) to reduce the integral

over $\partial\mathbb{D}_m$ to a single term. This yields

$$I_{\partial\mathbb{D}_m} = -\int_{\partial\mathbb{D}_m} \frac{2}{j\omega\rho(\mathbf{x})} \left\{G^+(\mathbf{x},\mathbf{x}_F,\omega)\right\}^* \partial_3 G^+(\mathbf{x},\mathbf{x}_0''',\omega)\mathrm{d}^2\mathbf{x}. \tag{5.10}$$

We define the pressure-normalized transmission response as

$$T(\mathbf{x}_0''',\mathbf{x},\omega) = -\frac{2}{j\omega\rho(\mathbf{x})}\partial_3 G^+(\mathbf{x},\mathbf{x}_0''',\omega), \quad \text{for}\,\mathbf{x}\in\partial\mathbb{D}_m. \tag{5.11}$$

and rewrite equation 5.10 as

$$I_{\partial\mathbb{D}_m} = \int_{\partial\mathbb{D}_m} T(\mathbf{x}_0''',\mathbf{x},\omega)G^*(\mathbf{x},\mathbf{x}_F,\omega)\mathrm{d}^2\mathbf{x}, \tag{5.12}$$

where $G(\mathbf{x},\mathbf{x}_F,\omega) = G^+(\mathbf{x},\mathbf{x}_F,\omega)$. We finally combine equations 5.8 and 5.12 to obtain

$$\begin{aligned} &G(\mathbf{x}_0''',\mathbf{x}_F,\omega) \\ &= \int_{\partial\mathbb{D}_0} R(\mathbf{x}_0''',\mathbf{x},\omega)G^*(\mathbf{x}_F,\mathbf{x},\omega)\mathrm{d}^2\mathbf{x} + \int_{\partial\mathbb{D}_m} T(\mathbf{x}_0''',\mathbf{x},\omega)G^*(\mathbf{x}_F,\mathbf{x},\omega)\mathrm{d}^2\mathbf{x}, \end{aligned} \tag{5.13}$$

where we have used the source-receiver reciprocity relation $G(\mathbf{x},\mathbf{x}_F,\omega) = G(\mathbf{x}_F,\mathbf{x},\omega)$. Note that, if R and T are known, we could solve this equation to retrieve the unknown wave field G (but the trivial solution $G = 0$ would also be a valid solution).

Equation 5.13 is the starting point to derive the relationship with the one-sided integral equation given by Wapenaar et al. (2013a, 2012a, 2013b). In the time domain, equation 5.13 corresponds to

$$\begin{aligned} &G(\mathbf{x}_0''',\mathbf{x}_F,t) \\ &= \int_{\partial\mathbb{D}_0} \mathrm{d}^2\mathbf{x} \int_{-\infty}^{+\infty} R(\mathbf{x}_0''',\mathbf{x},t-t')G(\mathbf{x}_F,\mathbf{x},-t')dt' \\ &+ \int_{\partial\mathbb{D}_m} \mathrm{d}^2\mathbf{x} \int_{-\infty}^{+\infty} T(\mathbf{x}_0''',\mathbf{x},t-t')G(\mathbf{x}_F,\mathbf{x},-t')dt'. \end{aligned} \tag{5.14}$$

5.4 Relationships between Green's functions and focusing solution

In the domain $\mathbb{D}$ enclosed by the boundaries $\partial\mathbb{D}_0$ and $\partial\mathbb{D}_m$, we consider two independent acoustic states: the Green's function $G(\mathbf{x},\mathbf{x}_m,\omega)$ due to an impulsive point source of volume injection rate at $\mathbf{x}_m$ (just below $\partial\mathbb{D}_m$) and the *focusing solution* $f_1(\mathbf{x},\mathbf{x}_i',\omega)$. This particular

wave field $f_1(\mathbf{x}, \mathbf{x}'_i, \omega)$ is defined anywhere as the wave field that focuses at the location $\mathbf{x}'_i$ in the interior of $\mathbb{D}$. The domain $\mathbb{D}$ is source-free for all states, and the medium parameters are identical between the boundary $\partial\mathbb{D}_0$ and the depth level $\partial\mathbb{D}_i$, where $\partial\mathbb{D}_i$ is an arbitrary depth level between $\partial\mathbb{D}_0$ and $\partial\mathbb{D}_m$. For this situation, the reciprocity theorems of the convolution-type and correlation-type are (Fokkema and van den Berg, 1993), respectively,

$$\begin{aligned}\int_{\partial\mathbb{D}_0} \frac{1}{j\omega\rho(\mathbf{x}_0)} \left\{(\partial_3 f_1)G - f_1(\partial_3 G)\right\} \mathrm{d}^2\mathbf{x}_0 \\ = \int_{\partial\mathbb{D}_i} \frac{1}{j\omega\rho(\mathbf{x}_i)} \left\{(\partial_3 f_1)G - f_1(\partial_3 G)\right\} \mathrm{d}^2\mathbf{x}_i,\end{aligned} \tag{5.15}$$

$$\begin{aligned}\int_{\partial\mathbb{D}_0} \frac{1}{j\omega\rho(\mathbf{x}_0)} \left\{(\partial_3 f_1)^* G - f_1^*(\partial_3 G)\right\} \mathrm{d}^2\mathbf{x}_0 \\ = \int_{\partial\mathbb{D}_i} \frac{1}{j\omega\rho(\mathbf{x}_i)} \left\{(\partial_3 f_1)^* G - f_1^*(\partial_3 G)\right\} \mathrm{d}^2\mathbf{x}_i.\end{aligned} \tag{5.16}$$

Substituting $f_1 = f_1^+ + f_1^-$ and $G = G^+ + G^-$ into equations 5.15 and 5.16 and following the derivation in Appendix B.3 of Wapenaar and Berkhout (1989), we obtain

$$\begin{aligned}-\int_{\partial\mathbb{D}_0} \frac{2}{j\omega\rho(\mathbf{x}_0)} \left\{f_1^+(\partial_3 G^-) + f_1^-(\partial_3 G^+)\right\} \mathrm{d}^2\mathbf{x}_0 \\ = \int_{\partial\mathbb{D}_i} \frac{2}{j\omega\rho(\mathbf{x}_i)} \left\{(\partial_3 f_1^+)G^- + (\partial_3 f_1^-)G^+\right\} \mathrm{d}^2\mathbf{x}_i,\end{aligned} \tag{5.17}$$

$$\begin{aligned}-\int_{\partial\mathbb{D}_0} \frac{2}{j\omega\rho(\mathbf{x}_0)} \left\{(f_1^+)^*(\partial_3 G^+) + (f_1^-)^*(\partial_3 G^-)\right\} \mathrm{d}^2\mathbf{x}_0 \\ = \int_{\partial\mathbb{D}_i} \frac{2}{j\omega\rho(\mathbf{x}_i)} \left\{(\partial_3 f_1^+)^* G^+ + (\partial_3 f_1^-)^* G^-\right\} \mathrm{d}^2\mathbf{x}_i,\end{aligned} \tag{5.18}$$

where in equation 5.18 the evanescent wave field is neglected.

Figure 5.2 shows the two different states to which we apply equations 5.17 and 5.18. State A1 is defined in the actual medium between the boundaries $\partial\mathbb{D}_0$ and $\partial\mathbb{D}_m$, and a source is located at $\mathbf{x}_m$, just below $\partial\mathbb{D}_m$. The downgoing and upgoing Green's function at $\mathbf{x}_0 \in \partial\mathbb{D}_0$

are

$$\frac{2}{j\omega\rho(\mathbf{x}_0)}\partial_3 G^+(\mathbf{x},\mathbf{x}_m,\omega)|_{x_3=x_{3,0}} = 0, \tag{5.19}$$

$$\frac{2}{j\omega\rho(\mathbf{x}_0)}\partial_3 G^-(\mathbf{x},\mathbf{x}_m,\omega)|_{x_3=x_{3,0}} = T(\mathbf{x}_m,\mathbf{x}_0,\omega). \tag{5.20}$$

State B1 is defined in a reference medium where the medium parameters are identical to the actual medium between the boundary $\partial\mathbb{D}_0$ and the depth level $\partial\mathbb{D}_i$. Below $\partial\mathbb{D}_i$, state B1 is composed of a reflection-free half-space. The focusing solution f_1 is defined in this reference medium and its dowgoing and upgoing components at $\mathbf{x}_i' \in \partial\mathbb{D}_i$ are

$$\frac{2}{j\omega\rho(\mathbf{x}_i)}\partial_3 f_1^+(\mathbf{x},\mathbf{x}_i',\omega)|_{x_3=x_{3,i}} = -\delta(\mathbf{x}_H - \mathbf{x}_H'), \tag{5.21}$$

$$\frac{2}{j\omega\rho(\mathbf{x}_i)}\partial_3 f_1^-(\mathbf{x},\mathbf{x}_i',\omega)|_{x_3=x_{3,i}} = 0. \tag{5.22}$$

Substituting equations 5.19-5.22 into equations 5.17-5.18 gives

$$G^-(\mathbf{x}_i',\mathbf{x}_m,\omega) = \int_{\partial\mathbb{D}_0} T(\mathbf{x}_m,\mathbf{x}_0,\omega) f_1^+(\mathbf{x}_0,\mathbf{x}_i',\omega)\mathrm{d}^2\mathbf{x}_0, \tag{5.23}$$

and

$$G^+(\mathbf{x}_i',\mathbf{x}_m,\omega) = -\int_{\partial\mathbb{D}_0} T(\mathbf{x}_m,\mathbf{x}_0,\omega)\left\{f_1^-(\mathbf{x}_0,\mathbf{x}_i',\omega)\right\}^* \mathrm{d}^2\mathbf{x}_0. \tag{5.24}$$

Adding these last two expressions yields

$$G(\mathbf{x}_i',\mathbf{x}_m,\omega) = \int_{\partial\mathbb{D}_0} T(\mathbf{x}_m,\mathbf{x}_0,\omega) f_2(\mathbf{x}_i',\mathbf{x}_0,\omega)\mathrm{d}^2\mathbf{x}_0, \tag{5.25}$$

where we defined a second focusing solution $f_2(\mathbf{x}_i',\mathbf{x}_0''',\omega) = f_1^+(\mathbf{x}_0''',\mathbf{x}_i',\omega) - \left\{f_1^-(\mathbf{x}_0''',\mathbf{x}_i',\omega)\right\}^*$. The focusing solution f_2 has a focal point at $\mathbf{x}_0'''$ (Wapenaar et al., 2013a), as shown in Figure 5.3.

Finally, we introduce two different definitions of the inverse of the transmission response:

$$\delta(\mathbf{x}_H - \mathbf{x}_H') = \int_{\partial\mathbb{D}_m} T(\mathbf{x}_m,\mathbf{x}_0,\omega) T^{\mathrm{inv}}(\mathbf{x}_m,\mathbf{x}_0',\omega)\mathrm{d}^2\mathbf{x}_m, \tag{5.26}$$

$$\delta(\mathbf{x}_H - \mathbf{x}_H') = \int_{\partial\mathbb{D}_0} T(\mathbf{x}_0,\mathbf{x}_m,\omega) T^{\mathrm{inv}}(\mathbf{x}_0,\mathbf{x}_m',\omega)\mathrm{d}^2\mathbf{x}_0, \tag{5.27}$$

where $\mathbf{x}_0$ and $\mathbf{x}_0'$ are located on the top boundary $\partial\mathbb{D}_0$, and $\mathbf{x}_m$ and $\mathbf{x}_m'$ are located on the bottom boundary $\partial\mathbb{D}_m$.

5.5 Comparison between the integral equations

In this section, we show the consistency between two-sided, i.e. equation 5.13, and one-sided Green's function representations. Substituting equation 5.13 into itself gives

$$\begin{aligned} &G(\mathbf{x}_0''', \mathbf{x}_F, \omega) \\ &= \int_{\partial\mathbb{D}_0} \mathrm{d}^2\mathbf{x}_0 R(\mathbf{x}_0''', \mathbf{x}_0, \omega) \int_{\partial\mathbb{D}_0} \left\{R(\mathbf{x}_0, \mathbf{x}_0'', \omega)\right\}^* G(\mathbf{x}_0'', \mathbf{x}_F, \omega)\mathrm{d}^2\mathbf{x}_0'' \\ &+ \int_{\partial\mathbb{D}_0} \mathrm{d}^2\mathbf{x}_0 R(\mathbf{x}_0''', \mathbf{x}_0, \omega) \int_{\partial\mathbb{D}_m} \left\{T(\mathbf{x}_0, \mathbf{x}_m, \omega)\right\}^* G(\mathbf{x}_m, \mathbf{x}_F, \omega)\mathrm{d}^2\mathbf{x}_m \\ &+ \int_{\partial\mathbb{D}_m} T(\mathbf{x}_0''', \mathbf{x}_m, \omega) \left\{G(\mathbf{x}_F, \mathbf{x}_m, \omega)\right\}^* \mathrm{d}^2\mathbf{x}_m. \end{aligned} \tag{5.28}$$

Bringing the first term of the right-hand side to the left-hand side yields

$$\begin{aligned} &\int_{\partial\mathbb{D}_0} \mathrm{d}^2\mathbf{x}_0'' G(\mathbf{x}_0'', \mathbf{x}_F, \omega) \underbrace{\left[\delta(\mathbf{x}_H'' - \mathbf{x}_H''') - \int_{\partial\mathbb{D}_0} R(\mathbf{x}_0''', \mathbf{x}_0, \omega) \left\{R(\mathbf{x}_0, \mathbf{x}_0'', \omega)\right\}^* \mathrm{d}^2\mathbf{x}_0\right]}_{\mathrm{T1}} \\ &= \int_{\partial\mathbb{D}_0} \mathrm{d}^2\mathbf{x}_0 R(\mathbf{x}_0''', \mathbf{x}_0, \omega) \int_{\partial\mathbb{D}_m} \left\{T(\mathbf{x}_0, \mathbf{x}_m, \omega)\right\}^* G(\mathbf{x}_F, \mathbf{x}_m, \omega)\mathrm{d}^2\mathbf{x}_m \\ &+ \int_{\partial\mathbb{D}_m} T(\mathbf{x}_0''', \mathbf{x}_m, \omega) \left\{G(\mathbf{x}_F, \mathbf{x}_m, \omega)\right\}^* \mathrm{d}^2\mathbf{x}_m. \end{aligned} \tag{5.29}$$

Wapenaar et al. (2004) derive a relationship between flux-normalized reflection and transmission responses for a domain $\mathbb{D}$ enclosed by boundaries $\partial\mathbb{D}_0$ and $\partial\mathbb{D}_m$. In Appendix E, we derive a similar relationship for pressure-normalized reflection and transmission responses, equation E.14; its expression is

$$\begin{aligned} &\int_{\partial\mathbb{D}_m} \left\{T(\mathbf{x}_m, \mathbf{x}_0'', \omega)\right\}^* T(\mathbf{x}_0''', \mathbf{x}_m, \omega)\mathrm{d}^2\mathbf{x}_m \\ &\quad = \delta(\mathbf{x}_H'' - \mathbf{x}_H''') - \int_{\partial\mathbb{D}_0} R(\mathbf{x}_0''', \mathbf{x}_0, \omega) \left\{R(\mathbf{x}_0, \mathbf{x}_0'', \omega)\right\}^* \mathrm{d}^2\mathbf{x}_0. \end{aligned} \tag{5.30}$$

Note that equation 5.30 shows the unitarity of the scattering matrix (Rodberg and Thaler, 1967). Now, we use equation 5.30 to rewrite term T1 of equation 5.29:

$$\begin{aligned}\int_{\partial\mathbb{D}_0} \mathrm{d}^2\mathbf{x}_0'' G(\mathbf{x}_0'', \mathbf{x}_F, \omega) \int_{\partial\mathbb{D}_m} \left\{T(\mathbf{x}_m, \mathbf{x}_0'', \omega)\right\}^* T(\mathbf{x}_0''', \mathbf{x}_m, \omega)\mathrm{d}^2\mathbf{x}_m \\ = \int_{\partial\mathbb{D}_0} \mathrm{d}^2\mathbf{x}_0 R(\mathbf{x}_0''', \mathbf{x}_0, \omega) \int_{\partial\mathbb{D}_m} \left\{T(\mathbf{x}_0, \mathbf{x}_m, \omega)\right\}^* G(\mathbf{x}_F, \mathbf{x}_m, \omega)\mathrm{d}^2\mathbf{x}_m \\ + \int_{\partial\mathbb{D}_m} T(\mathbf{x}_0''', \mathbf{x}_m, \omega) \left\{G(\mathbf{x}_F, \mathbf{x}_m, \omega)\right\}^* \mathrm{d}^2\mathbf{x}_m.\end{aligned} \tag{5.31}$$

Then, we insert equation 5.25 into equation 5.31 and, after rearranging the terms, obtain

$$\begin{aligned}\int_{\partial\mathbb{D}_0} \mathrm{d}^2\mathbf{x}_0'' G(\mathbf{x}_0'', \mathbf{x}_F, \omega) \int_{\partial\mathbb{D}_m} \left\{T(\mathbf{x}_m, \mathbf{x}_0'', \omega)\right\}^* T(\mathbf{x}_0''', \mathbf{x}_m, \omega)\mathrm{d}^2\mathbf{x}_m \\ = \int_{\partial\mathbb{D}_0} \mathrm{d}^2\mathbf{x}_0 R(\mathbf{x}_0''', \mathbf{x}_0, \omega) \int_{\partial\mathbb{D}_0} \mathrm{d}^2\mathbf{x}_0' f_2(\mathbf{x}_F, \mathbf{x}_0', \omega) \int_{\partial\mathbb{D}_m} T(\mathbf{x}_m, \mathbf{x}_0', \omega) \left\{T(\mathbf{x}_0, \mathbf{x}_m, \omega)\right\}^* \mathrm{d}^2\mathbf{x}_m \\ + \int_{\partial\mathbb{D}_0} \mathrm{d}^2\mathbf{x}_0'' \left\{f_2(\mathbf{x}_F, \mathbf{x}_0'', \omega)\right\}^* \int_{\partial\mathbb{D}_m} \left\{T(\mathbf{x}_m, \mathbf{x}_0'', \omega)\right\}^* T(\mathbf{x}_0''', \mathbf{x}_m, \omega)\mathrm{d}^2\mathbf{x}_m.\end{aligned} \tag{5.32}$$

Now, we focus on the first term on the right-hand side of equation 5.32 which we rewrite here:

$$\int_{\partial\mathbb{D}_0} \mathrm{d}^2\mathbf{x}_0 R(\mathbf{x}_0''', \mathbf{x}_0, \omega) \int_{\partial\mathbb{D}_0} \mathrm{d}^2\mathbf{x}_0' f_2(\mathbf{x}_F, \mathbf{x}_0', \omega) \int_{\partial\mathbb{D}_m} T(\mathbf{x}_m, \mathbf{x}_0', \omega) \left\{T(\mathbf{x}_0, \mathbf{x}_m, \omega)\right\}^* \mathrm{d}^2\mathbf{x}_m. \tag{5.33}$$

We take the complex-conjugate of equation 5.30 and then insert it into equation 5.33

$$\begin{aligned}\int_{\partial\mathbb{D}_0} R(\mathbf{x}_0''', \mathbf{x}_0, \omega) f_2(\mathbf{x}_F, \mathbf{x}_0, \omega)\mathrm{d}^2\mathbf{x}_0 \\ - \int_{\partial\mathbb{D}_0} \mathrm{d}^2\mathbf{x}_0 f_2(\mathbf{x}_F, \mathbf{x}_0, \omega) \int_{\partial\mathbb{D}_0} \mathrm{d}^2\mathbf{x}_0'' R(\mathbf{x}_0'', \mathbf{x}_0, \omega) \int_{\partial\mathbb{D}_0} R(\mathbf{x}_0''', \mathbf{x}_0', \omega) \left\{R(\mathbf{x}_0', \mathbf{x}_0'', \omega)\right\}^* \mathrm{d}^2\mathbf{x}_0',\end{aligned} \tag{5.34}$$

where we performed a change of variables in the second term. Following a similar step, we insert equation 5.30 into equation 5.34:

$$\int_{\partial\mathbb{D}_0} \mathrm{d}^2\mathbf{x}_0 f_2(\mathbf{x}_F, \mathbf{x}_0, \omega) \int_{\partial\mathbb{D}_0} \mathrm{d}^2\mathbf{x}_0'' R(\mathbf{x}_0'', \mathbf{x}_0, \omega) \int_{\partial\mathbb{D}_m} \left\{T(\mathbf{x}_m, \mathbf{x}_0'', \omega)\right\}^* T(\mathbf{x}_0''', \mathbf{x}_m, \omega)\mathrm{d}^2\mathbf{x}_m. \tag{5.35}$$

Using equation 5.35, we can rewrite equation 5.32 as

$$\begin{aligned}
&\int_{\partial\mathbb{D}_0} \mathrm{d}^2\mathbf{x}_0'' G(\mathbf{x}_0'', \mathbf{x}_F, \omega) \int_{\partial\mathbb{D}_m} \left\{T(\mathbf{x}_m, \mathbf{x}_0'', \omega)\right\}^* T(\mathbf{x}_0''', \mathbf{x}_m, \omega) \mathrm{d}^2\mathbf{x}_m \qquad (5.36)\\
&= \int_{\partial\mathbb{D}_0} \mathrm{d}^2\mathbf{x}_0 f_2(\mathbf{x}_F, \mathbf{x}_0, \omega) \int_{\partial\mathbb{D}_0} \mathrm{d}^2\mathbf{x}_0'' R(\mathbf{x}_0'', \mathbf{x}_0, \omega) \int_{\partial\mathbb{D}_m} \left\{T(\mathbf{x}_m, \mathbf{x}_0'', \omega)\right\}^* T(\mathbf{x}_0''', \mathbf{x}_m, \omega) \mathrm{d}^2\mathbf{x}_m\\
&+ \int_{\partial\mathbb{D}_0} \mathrm{d}^2\mathbf{x}_0'' \left\{f_2(\mathbf{x}_F, \mathbf{x}_0'', \omega)\right\}^* \int_{\partial\mathbb{D}_m} \left\{T(\mathbf{x}_m, \mathbf{x}_0'', \omega)\right\}^* T(\mathbf{x}_0''', \mathbf{x}_m, \omega) \mathrm{d}^2\mathbf{x}_m.
\end{aligned}$$

Note that all the terms in equation 5.36 include a surface integral over $\partial\mathbb{D}_m$ of the transmission responses. To remove this integral, first, we multiply both sides of equation 5.36 by the inverse of the transmission response $T(\mathbf{x}_0''', \mathbf{x}_m, \omega)$ and integrate over $\partial\mathbb{D}_0$. Then, following a similar process, we multiply both sides of equation 5.36 by the inverse of the transmission response $\{T(\mathbf{x}_m, \mathbf{x}_0'', \omega)\}^*$ and integrate over $\partial\mathbb{D}_m$. This allows us to eliminate the surface integral of the transmission responses and yields

$$\begin{aligned}
&G(\mathbf{x}_0''', \mathbf{x}_F, \omega) \qquad (5.37)\\
&\quad = \int_{\partial\mathbb{D}_0} R(\mathbf{x}_0''', \mathbf{x}_0, \omega) f_2(\mathbf{x}_F, \mathbf{x}_0, \omega) \mathrm{d}^2\mathbf{x}_0 + \left\{f_2(\mathbf{x}_F, \mathbf{x}_0''', \omega)\right\}^*.
\end{aligned}$$

The right-hand side of equation 5.37 contains a surface integral over only the top boundary $\partial\mathbb{D}_0$; hence we do not require any measurements on the bottom boundary $\partial\mathbb{D}_m$ which are needed by equation 5.13. Additionally, equation 5.37 now requires knowledge of the focusing wave field f_2 (whit focal points on the top boundary $\partial\mathbb{D}_0$) rather then the Green's function recorded at $\mathbf{x}_F$ and due to sources on the top and bottom boundaries. Wapenaar et al. (2013a) use a causality argument to solve equation 5.37 in the time domain for the focusing solution f_2. Once f_2 is known, it can be used to retrieve $G(\mathbf{x}_0''', \mathbf{x}_F, \omega)$. The one-sided Green's function representation of equation 5.37 is the key result of our paper. This expression shows that the two-sided and one-sided integral equations for the Green's function retrieval lead to equivalent results.

5.6 Conclusion

We have shown the connection between one- and two-sided integral equations for Green's function retrieval. Representations based on one-sided equations are more recent and present a practical advantage because they remove the physical constraints of having receivers and sources at depth; hence, they do not require approximations that are needed because measurements are unavailable at depth. On the other hand, methods requiring data on a closed boundary (two-sided) present well-known applications. For these reasons, their connection can introduce mutual benefits to the different representations.

5.7 Acknowledgments

We thank Ken Larner for his constructive comments. This work was supported by the sponsors of the Consortium Project on Seismic Inverse Methods for Complex Structures at the Center for Wave Phenomena and the Netherlands Research Centre for Integrated Solid Earth Science (ISES).

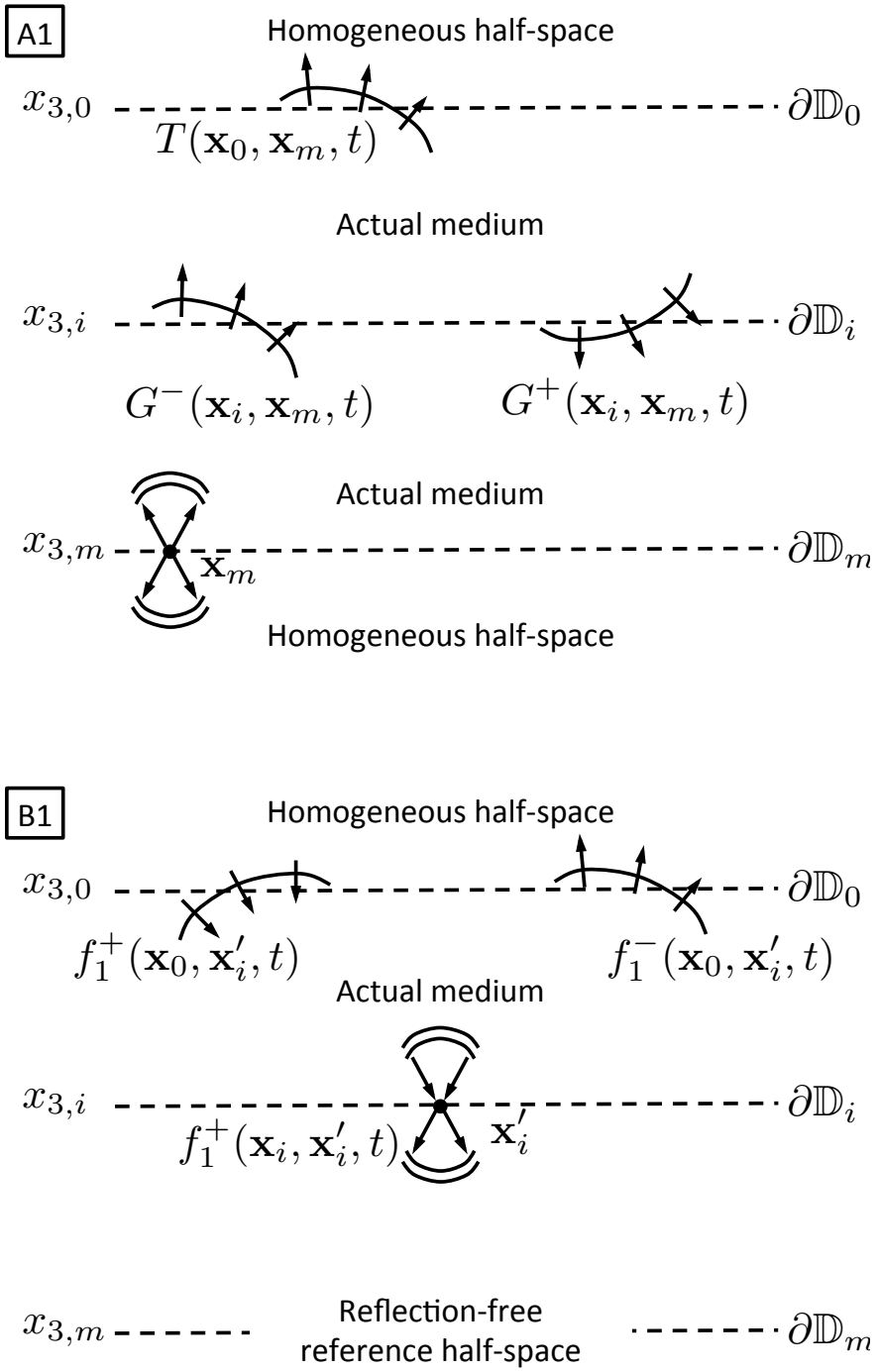

Figure 5.2: States for reciprocity theorems. Top - State A1: Green's function with a source at $\mathbf{x}_m$ just below $\partial\mathbb{D}_m$. Bottom - State B1: focusing solution f_1 with a focal point at $\mathbf{x}_i'$ at depth level $\partial\mathbb{D}_i$.

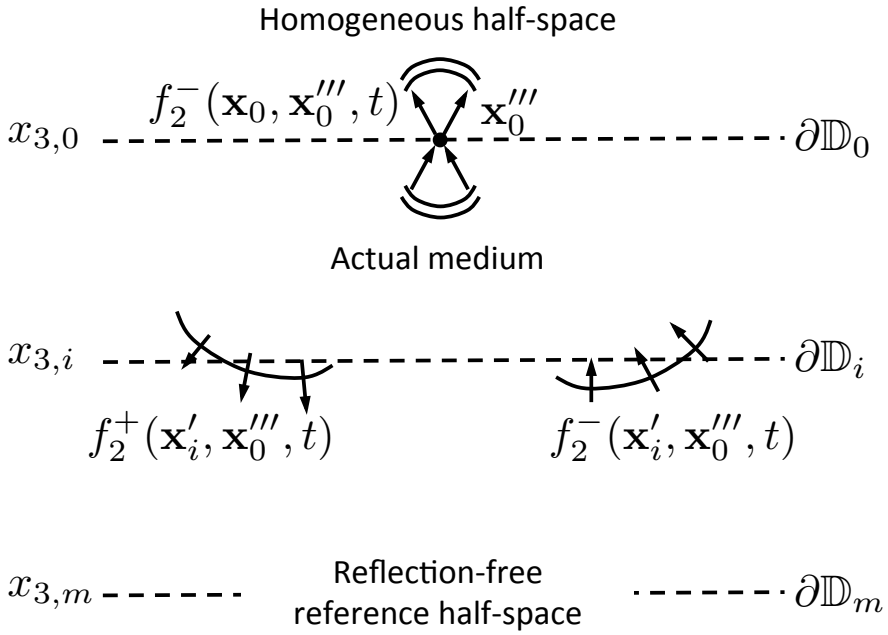

Figure 5.3: Focusing solution f_2 with a focal point at $\mathbf{x}_0'''$ at the depth level $\partial\mathbb{D}_0$.

CHAPTER 6

WAVE FIELD AUTOFOCUSING AND IMAGING WITH MULTIDIMENSIONAL DECONVOLUTION: NUMERICAL EXAMPLES FOR REFLECTION DATA WITH INTERNAL MULTIPLES

Filippo Broggini[1,2], **Roel Snieder**[1], **and Kees Wapenaar**[3]

In preparation for *Geophysics*

6.1 Abstract

Standard imaging techniques rely on the single scattering assumption. This requires that the recorded data do not include internal multiples, i.e. waves bouncing multiple times between layers before reaching the receivers at the acquisition surface. When multiple reflections are present in the data, standard imaging algorithms incorrectly image them as ghost reflectors. These artifacts can mislead the interpreters in locating potential hydrocarbon reservoirs. Recently, we introduced a new approach for retrieving the Green's function recorded at the acquisition surface due to a virtual source located at depth. We refer to this approach as wave field *autofocusing*. Additionally, autofocusing allows us to decompose the Green's function in its downgoing and upgoing components. These wave fields are then used to create a ghost-free image of the medium with either crosscorrelation or multidimensional deconvolution, presenting an advantage over standard prestack migration. We test the robustness of our approach when an erroneous velocity model is used to estimate the first-arriving waves which are a required input for the autofocusing process. We illustrate the new method with a numerical example based on a modification of the Amoco model.

[1]Center for Wave Phenomena, Colorado School of Mines, Golden, CO 80401, USA
[2]Principal researcher and author
[3]Delft University of Technology, Department of Geoscience and Engineering, Delft, The Netherlands

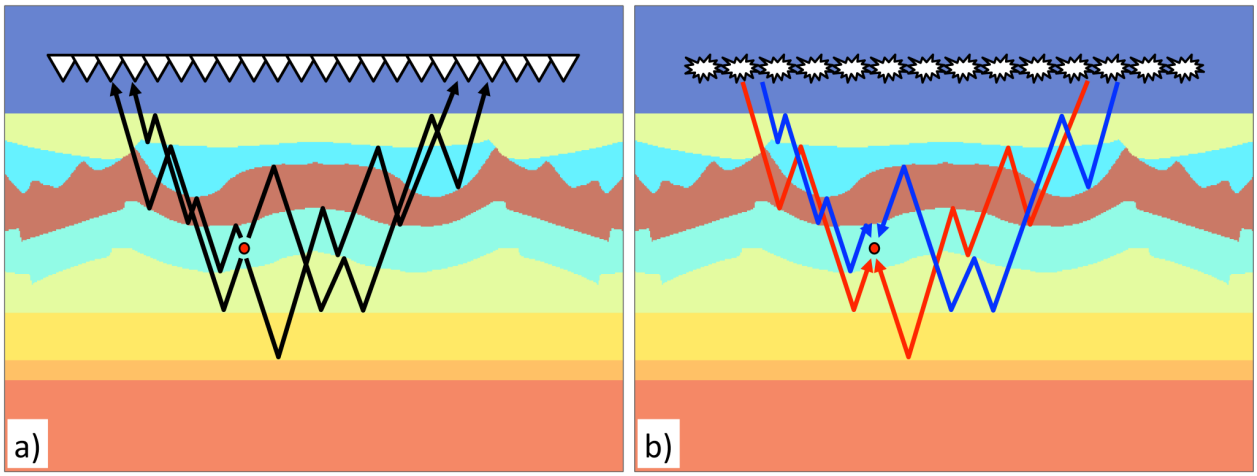

Figure 6.1: a) Total wave field from the imaging point located at $\mathbf{x}_\mathrm{I}$ (indicated by the red dot) and recorded at the acquisition surface. b) Decomposed wave fields. The solid blue rays correspond to the downgoing component $G^+(\mathbf{x}_\mathrm{I}, \mathbf{x}, t)$. The solid red rays correspond to the upgoing component $G^-(\mathbf{x}_\mathrm{I}, \mathbf{x}, t)$.

6.2 Introduction

One of the main goals of exploration geophysics is to retrieve the location and amplitude of the discontinuities between layers with different properties inside the subsurface from reflection data acquired on the surface of the Earth. This is a challenging research task because an accurate image of the structures inside the Earth is needed to locate energy sources, such as hydrocarbon reservoirs.

Standard imaging methods, such as one-way prestack migration (Claerbout, 1985), usually suffer from artifacts (ghost images) due to the presence of multiple reflections in the recorded data. These multiple reflections are often caused by high impedance layers, such as salt bodies, and hence they can severely affect the final images. One-way imaging schemes cannot differentiate between primaries and multiples; hence they erroneously interpret the multiply reflected waves as primary reflections due to deeper layers.

We have recently introduced a new method that allows us to reconstruct the total wave field originating from a point in the subsurface to receivers located at the surface (Wapenaar et al., 2013a, 2012a). Following Rose (2002a), we refer to this approach as wave field *auto-*

focusing. The Green's function, defined as the response recorded at the acquisition surface due to a source located in the interior of the subsurface, see Figure 6.1a, is a combination of the downgoing and upgoing wave fields needed to reconstruct an image of the discontinuities inside the Earth. These downgoing and upgoing wave fields are illustrated in Figure 6.1b, where we have applied source-receiver reciprocity. The new method consists of an iterative algorithm that transforms the reflection response (at the acquisition surface) of an arbitrary medium into the wave field generated by a virtual source inside the unknown medium. Apart from requiring the reflection data measured at the surface, autofocusing also requires an estimate of the traveltimes of the first-arriving wave traveling from the virtual source location to receivers located at the acquisition surface. These traveltimes are a key element of the method because they specify the location of the virtual source in the subsurface. Consequently, the proposed method is not fully model-independent. However, we do not require any more knowledge of the medium parameters than standard primary imaging schemes. We emphasize that we use the internal multiples to construct images with more correct amplitudes, while other methods aim at removing the internal multiples before the imaging step (Berkhout and Verschuur, 1997; Jakubowicz, 1998; ten Kroode, 2002; Weglein et al., 1997). Moreover, our method is non-recursive, which means that it does not suffer from error propagation. Also we do not need to resolve the multiple problem in the overburden prior to imaging a specific target zone.

We start with a brief review of the theory behind autofocusing, and describe how to decompose the Green's function in its downgoing and upgoing components. Then, we apply autofocusing to a synthetic data set and compare its imaging capabilities with those of one-way prestack migration. Finally, we show the robustness of our method when an erroneous velocity model is used to compute an estimate of the first-arriving waves.

6.3 Theory of autofocusing

Following recent work (Broggini et al., 2012a,b; Wapenaar et al., 2013a, 2012a), we briefly introduce the theory of wave field autofocusing for two-dimensional media and illustrate it

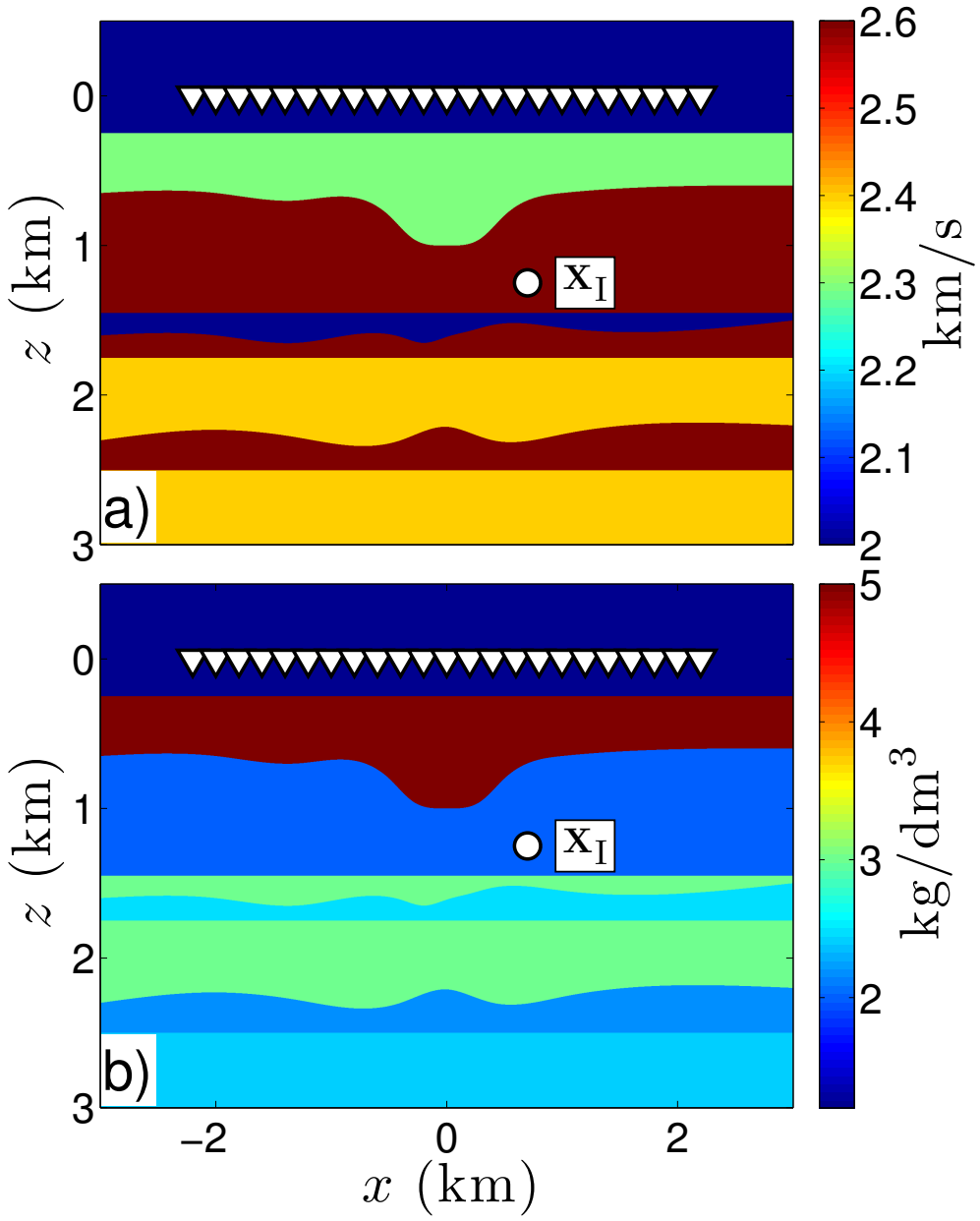

Figure 6.2: a) Velocity model. b) Density model. In both panels, the white triangles denote the receivers at $z = 0$, and the white circle indicates the location of the source of the retrieved Green's function.

with a numerical example in an inhomogeneous medium shown in Figure 6.2. This method implements an iterative scheme which requires 1) an estimate of the first-arriving wave between an image point $\mathbf{x}_\mathrm{I}$ in the subsurface and the receivers at the surface, and 2) the measured reflection response deconvolved for the source wavelet and without surface-related multiples. We denote these two input as $G_d(\mathbf{x}_0, \mathbf{x}_\mathrm{I}, t)$ and $R(\mathbf{x}_0, \mathbf{x}, t)$, respectively. The first-arriving wave for the model of Figure 6.2 is shown in Figure 6.3. The iterative scheme is based on a system of two integral equations which relates downgoing waves $p_k^+(\mathbf{x}_0, \mathbf{x}_\mathrm{I}, t)$ and upgoing waves $p_k^-(\mathbf{x}_0, \mathbf{x}_\mathrm{I}, t)$ at the acquisition surface $\partial\mathbb{D}_0$:

$$p_k^+(\mathbf{x}_0, \mathbf{x}_\mathrm{I}, t) = p_0^+(\mathbf{x}_0, \mathbf{x}_\mathrm{I}, t) - w(\mathbf{x}_0, -t)p_k^-(\mathbf{x}_0, \mathbf{x}_\mathrm{I}, -t), \tag{6.1}$$

$$p_k^-(\mathbf{x}_0, \mathbf{x}_\mathrm{I}, t) = \int_{\partial\mathbb{D}_0} \mathrm{d}^2\mathbf{x} \int_{-\infty}^{+\infty} R(\mathbf{x}_0, \mathbf{x}, t - t')p_k^+(\mathbf{x}, \mathbf{x}_\mathrm{I}, t')\mathrm{d}t', \tag{6.2}$$

where k is the iteration number. The window function $w(\mathbf{x}_0, t)$ satisfies

$$w(\mathbf{x}_0, -t) = \Theta(t + t_f(\mathbf{x}_0, \mathbf{x}_\mathrm{I}) - \epsilon), \tag{6.3}$$

where $\Theta(t)$ is the Heaviside function, $t_f(\mathbf{x}_0, \mathbf{x}_\mathrm{I})$ is the arrival time of the first arriving wave propagating from the target point $\mathbf{x}_\mathrm{I}$ to the acquisition surface at $z = 0$, and ϵ is a small positive constant related to the duration of the source wavelet $s(t)$. The window function $w(\mathbf{x}_0, t)$ is equal to 1 for $t < t_f(\mathbf{x}_0, \mathbf{x}_\mathrm{I})$ and equal to 0 elsewhere. The iterative scheme starts with the downgoing wave field $p_0^+(\mathbf{x}_0, \mathbf{x}_\mathrm{I}, t)$ which is defined as the time-reversed version of the first arriving wave, $G_d(\mathbf{x}_0, \mathbf{x}_\mathrm{I}, -t)$, and is only nonzero when

$$p_0^+(\mathbf{x}_0, \mathbf{x}_\mathrm{I}, t) \neq 0 \quad \text{only for} \quad t < -(t_f(\mathbf{x}_0, \mathbf{x}_\mathrm{I}) - \epsilon). \tag{6.4}$$

The method converges after several iterations and Wapenaar et al. (2013a,b) show that the Green's function propagating between a location $\mathbf{x}_\mathrm{I}$ inside the subsurface and the receivers on the acquisition surface at $z = 0$ is related to the downgoing and upgoing wave fields p^+ and p^- by

$$G(\mathbf{x}_0, \mathbf{x}_\mathrm{I}, t) = p^+(\mathbf{x}_0, \mathbf{x}_\mathrm{I}, -t) + p^-(\mathbf{x}_0, \mathbf{x}_\mathrm{I}, t). \tag{6.5}$$

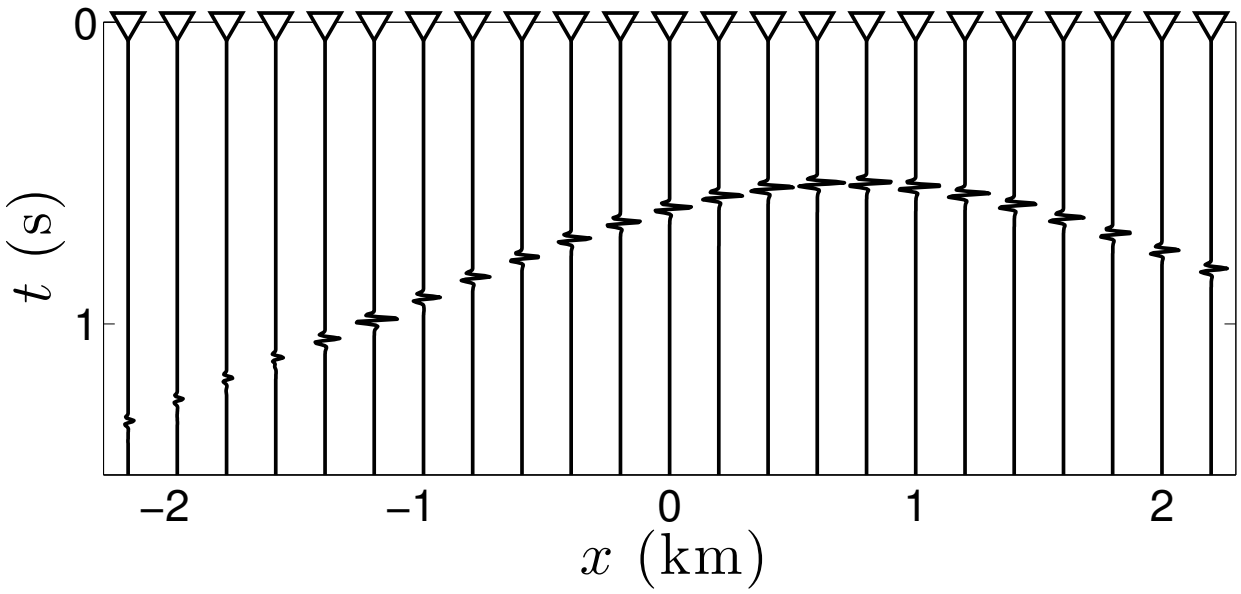

Figure 6.3: Estimate of the first-arriving wave propagating from the image point $\mathbf{x}_\mathrm{I}$ to the receivers (indicated by the white triangles) located at $z = 0$. The arrival times of this wave is denoted by $t_f(\mathbf{x}_0, \mathbf{x}_\mathrm{I})$, where $\mathbf{x}_0$ corresponds to the location of the receivers.

The retrieved Green's function is shown in Figure 6.4, where it is superposed to the directly-modeled reference wave field. The two wave fields match almost perfectly. A small mismatch is localized at large offset and is denoted by the red arrow in Figure 6.4. This mismatch is caused by the finite aperture of the employed receiver array and by refracted waves (such waves violate the up and down decomposition on which the theory is based). All traces have been multiplied by $\exp(2t)$ to emphasize the scattering coda which has been very well recovered. The number of iterations needed to reach convergence depends on the complexity of the subsurface. Wapenaar et al. (2012a) show that, for a simple medium, one iteration only is needed; while in Chapter 4 we show that rate of convergence follows a geometric series.

Now, we apply a simple source-receiver reciprocity argument $G(\mathbf{x}_\mathrm{I}, \mathbf{x}, t) = G(\mathbf{x}, \mathbf{x}_\mathrm{I}, t)$, and define $G(\mathbf{x}_\mathrm{I}, \mathbf{x}, t)$ as the wave field originating from sources at the surface and observed by a virtual receiver located at the imaging point $\mathbf{x}_\mathrm{I}$. To perform the decomposition of this Green's function in its downgoing $G^+(\mathbf{x}_\mathrm{I}, \mathbf{x}, t)$ and upgoing components $G^+(\mathbf{x}_\mathrm{I}, \mathbf{x}, t)$, we

consider a variant of the iterative scheme, in which the subtraction in equation 6.1 is replaced by an addition (Wapenaar et al., 2011a):

$$q_k^+(\mathbf{x}_0,\mathbf{x}_\mathrm{I},t) = q_0^+(\mathbf{x}_0,\mathbf{x}_\mathrm{I},t) + w(\mathbf{x}_0,-t)q_k^-(\mathbf{x}_0,\mathbf{x}_\mathrm{I},-t), \tag{6.6}$$

$$q_k^-(\mathbf{x}_0,\mathbf{x}_\mathrm{I},t) = \int_{\partial\mathbb{D}_0} \mathrm{d}^2\mathbf{x} \int_{-\infty}^{+\infty} R(\mathbf{x}_0,\mathbf{x},t-t')q_k^+(\mathbf{x},\mathbf{x}_\mathrm{I},t')\mathrm{d}t', \tag{6.7}$$

where the 0th iteration of the downgoing field $q_0^+(\mathbf{x},t)$ is equal to $p_0^+(\mathbf{x},t)$.

After the second iterative scheme reaches convergence, we define two additional wave fields: $p_{sym}(\mathbf{x},t) = p(\mathbf{x},t) + p(\mathbf{x},-t)$, and $p_{asym}(\mathbf{x},t) = q(\mathbf{x},t) - q(\mathbf{x},-t)$ (Wapenaar et al., 2012b). The Green's function recorded at $\mathbf{x}_\mathrm{I}$ is finally decomposed into downgoing and upgoing wave fields by combining $p_{sym}(\mathbf{x},t)$ and $p_{asym}(\mathbf{x},t)$ in two different ways, according to

$$G^+(\mathbf{x}_\mathrm{I},\mathbf{x},t) = \frac{1}{2}\left\{p_{sym}(\mathbf{x},t) - p_{asym}(\mathbf{x},t)\right\}, \quad \text{for } t \geq 0, \tag{6.8}$$

and

$$G^-(\mathbf{x}_\mathrm{I},\mathbf{x},t) = \frac{1}{2}\left\{p_{sym}(\mathbf{x},t) + p_{asym}(\mathbf{x},t)\right\}, \quad \text{for } t \geq 0. \tag{6.9}$$

These downgoing and upgoing (one-way) wave fields are used in the next section to create images of the subsurface with either prestack migration, crosscorrelation or multidimensional deconvolution.

6.4 Imaging

We consider a model based on a modified version of the Amoco dataset, originally introduced by Etgen and Regone (1998), as shown in Figure 6.5a. Since our method allows targeted imaging, we focus on the portion of the model enclosed by the solid rectangle in Figure 6.5a. The velocity and density profiles for this portion of the model are shown in Figures 6.6a and 6.6b. The black arrow in Figure 6.5a indicates a layer characterized by higher impedance with respect to the surrounding layers.

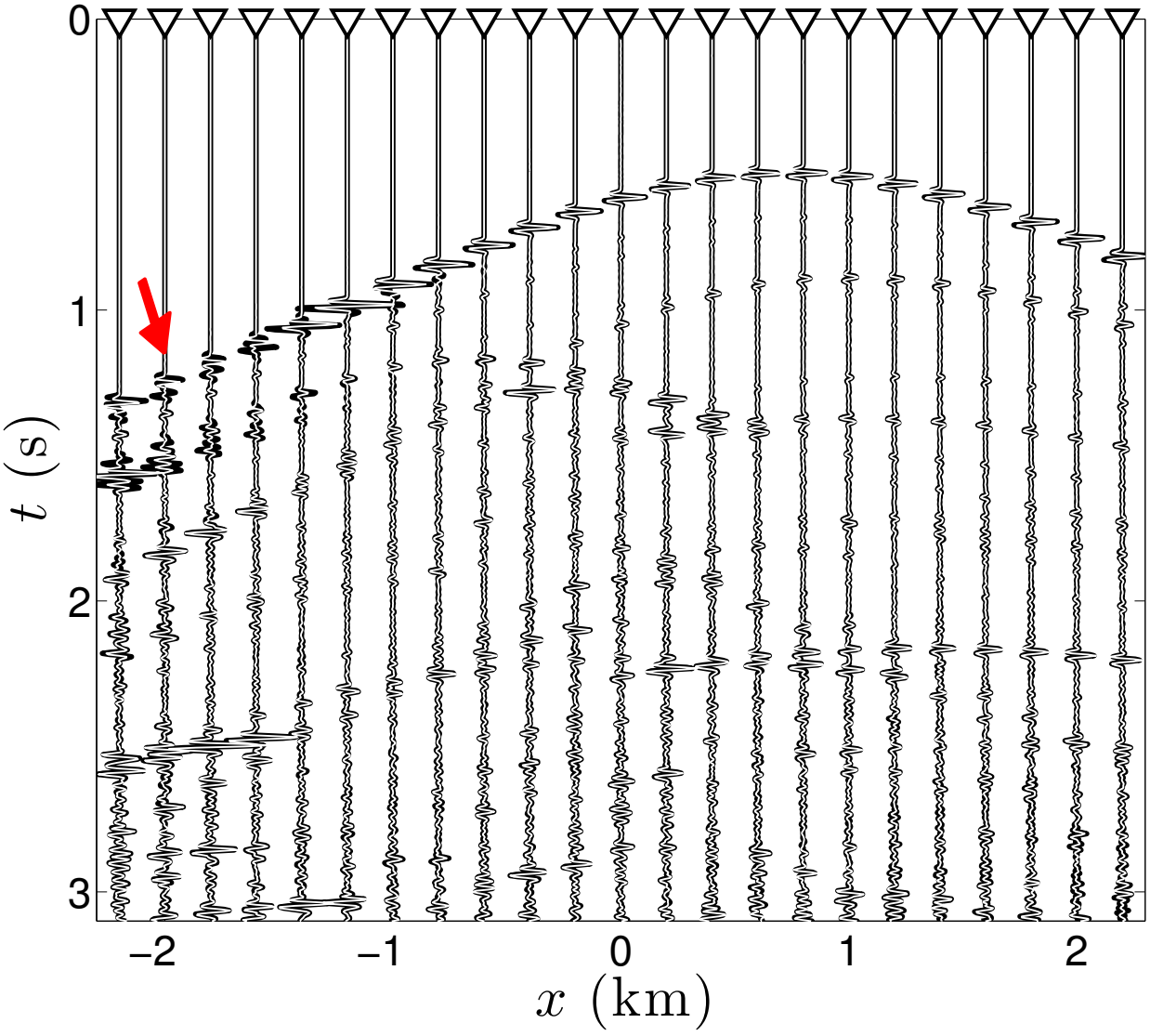

Figure 6.4: Superposition of the reference wave field originated by a real source located at $\mathbf{x}_{\mathrm{I}}$ (black line) and the wave field retrieved by the iterative scheme (white line). The two wave fields match almost perfectly. The red arrow denotes a mismatch localizes at large offset. All traces have been multiplied by $\exp(2t)$ to emphasize the scattering coda. The white triangles denote the receivers at $z = 0$.

We computed the response to 501 shots with sources located at $z = 0$ Km. The acquisition surface is transparent; hence no surface-related multiples are present. In the horizontal direction, the sources are located every 10 m between -2.5 and 2.5 km. In practice, the required reflection responses are obtained from conventional seismic reflection data after removal of the multiples due to the free-surface and after deconvolution for the source wavelet (Amundsen, 2001; van Groenestijn and Verschuur, 2009; Verschuur et al., 1992).

We compute the direct arriving wave front, required by our method, using an eikonal solver. As in input for the solver, we use a smooth version of the velocity model; see Figure 6.6c. Note that, using an eikonal solver, we ignore the influence of the density. We introduce another approximation assigning a constant amplitude to these first-arriving wave fields. Alternatively, the direct arriving wave front can be obtained by modeling in a macro model, from microseismic events (Artman et al., 2010), from borehole check shots, or directly from the data by the CFP method (Berkhout, 1997; Haffinger and Verschuur, 2012; Thorbecke, 1997) when the imaging point is located at an interface.

6.4.1 Standard prestack imaging

For comparison, we start by computing a reference image using standard one-way prestack migration (Berkhout, 1979; Claerbout, 1985; Gazdag and Sguazzero, 1984). One-way prestack migration and many other seismic imaging algorithms rely on the single scattering assumption. This implies that the recorded wave fields do not include internal multiples (waves bouncing multiple times between reflectors before reaching the receivers). When unwanted multiple reflections are present in the data, the imaging algorithm incorrectly images them as ghost reflectors. This reference image is shown in Figure 6.7a, where we have used the same smooth model of Figure 6.6c needed to compute the first arriving waves required by the iterative scheme. The high-impedance layer, indicated by the black arrow in Figure 6.5a, creates high-amplitude multiply-scattered waves. The yellow arrows in Figure 6.7a indicate some of the ghost reflectors present in this standard image. Additionally, the image is noisy below the high-impedance layer. The ghost reflectors and the noise mask the flat reflector at

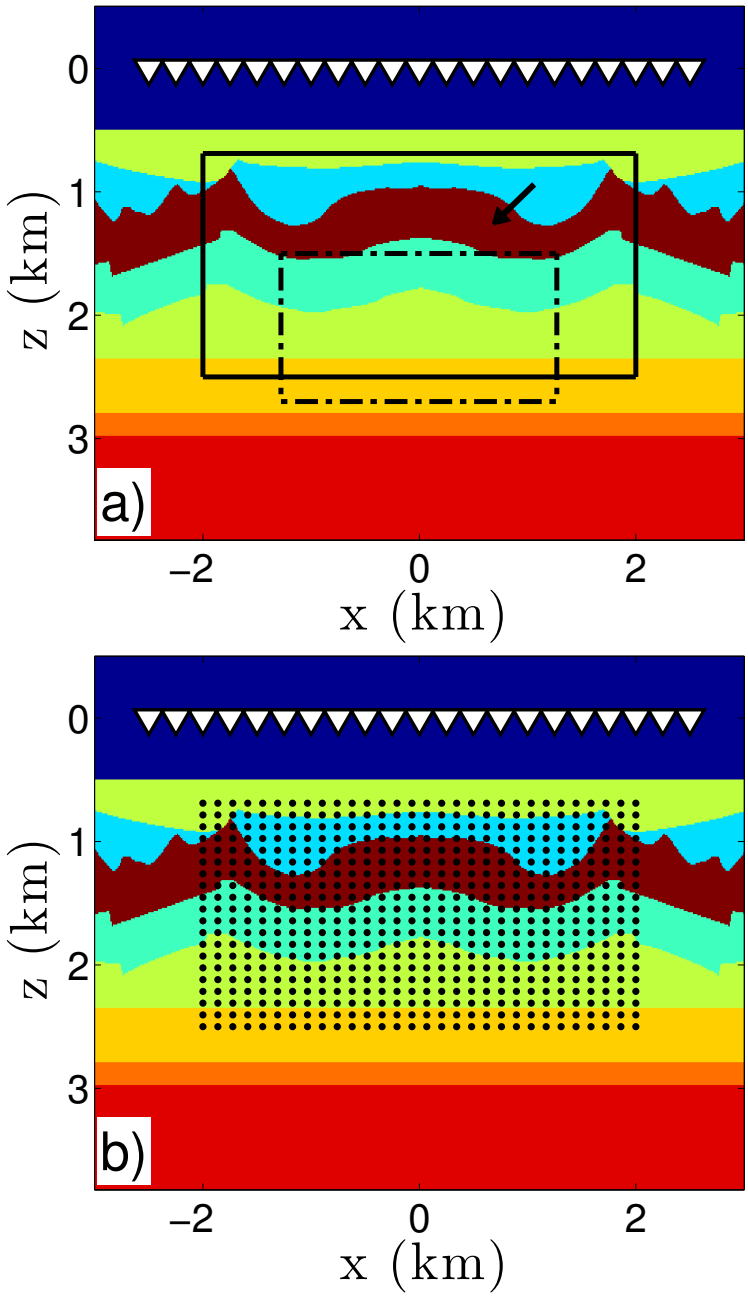

Figure 6.5: a) Velocity model. The white triangles denotes the receivers at $z = 0$. The black arrow indicates a layer characterized by higher impedance with respect to the surrounding layers. The solid rectangle encloses the target area used to compare the different imaging methods. The dashed rectangle bounds the portion of the subsurface used to compare the robustness of the different imaging methods when we use an erroneous background model. b) The black dots correspond to various imaging points $\mathbf{x}_{\mathrm{I}}$. Imaging points located on a constant depth level $z = z_i$ are used to resolve $[R(\mathbf{x}_r, \mathbf{x}, t)]_{z=z_i}$.

$z = 2.3$ km, indicated by the blue arrow in Figures 6.7b-c, and affect the lateral continuity of the deeper reflectors. The comparison between the amplitudes of this reference image and the true reflectivity is shown in Figure 6.8.

6.4.2 Imaging with crosscorrelation

If we retrieve the Green's function with our method and decompose it in its downgoing and upgoing components for imaging points $\mathbf{x}_\mathrm{I}$ located on many depth levels $z = z_i$ (e.g. the horizontal lines composed of black dots in Figure 6.5b), we are able to create a more accurate image of the medium. To perform this task, we compute the crosscorrelation function C

$$C(\mathbf{x}_\mathrm{I}, \mathbf{x}_\mathrm{I}, t) = \int_{-\infty}^{\infty} \left[G^-(\mathbf{x}_\mathrm{I}, \mathbf{x}, t) * G^+(\mathbf{x}_\mathrm{I}, \mathbf{x}, -t)\right]_{z=0} \mathrm{d}x \tag{6.10}$$

at every imaging point depth and evaluate the result at $t = 0$. This new image is shown in Figure 6.7b. As in the standard prestack image, the actual reflectors have been reconstructed at the correct spatial location, but now the image is free of internal multiple ghosts. The image is now less noisy and the flat reflector at $z = 2.3$ km is more visible. This is an improvement over the previous image as shown in Figure 6.8, but the retrieved amplitudes of the deeper targets are not consistent with the true reflection coefficients. This is due to fact that we have a limited source aperture, that we do not take into account the multi-dimensional nature of the seismic wave field, and that the reflectivity is the ratio of upgoing and downgoing waves which would require a deconvolution imaging condition rather than the standard crosscorrelation imaging condition.

6.4.3 Imaging with multidimensional deconvolution

Now, we show that multidimensional deconvolution allows us to create an image with more accurate amplitudes. As in imaging with crosscorrelation, we consider a constant depth level $z = z_i$. The Green's functions at this constant depth level are related by

$$G^-(\mathbf{x}_r, \mathbf{x}_s, t) = \int_{-\infty}^{\infty} \left[R(\mathbf{x}_r, \mathbf{x}, t) * G^+(\mathbf{x}, \mathbf{x}_s, t)\right]_{z=z_i} \mathrm{d}x, \tag{6.11}$$

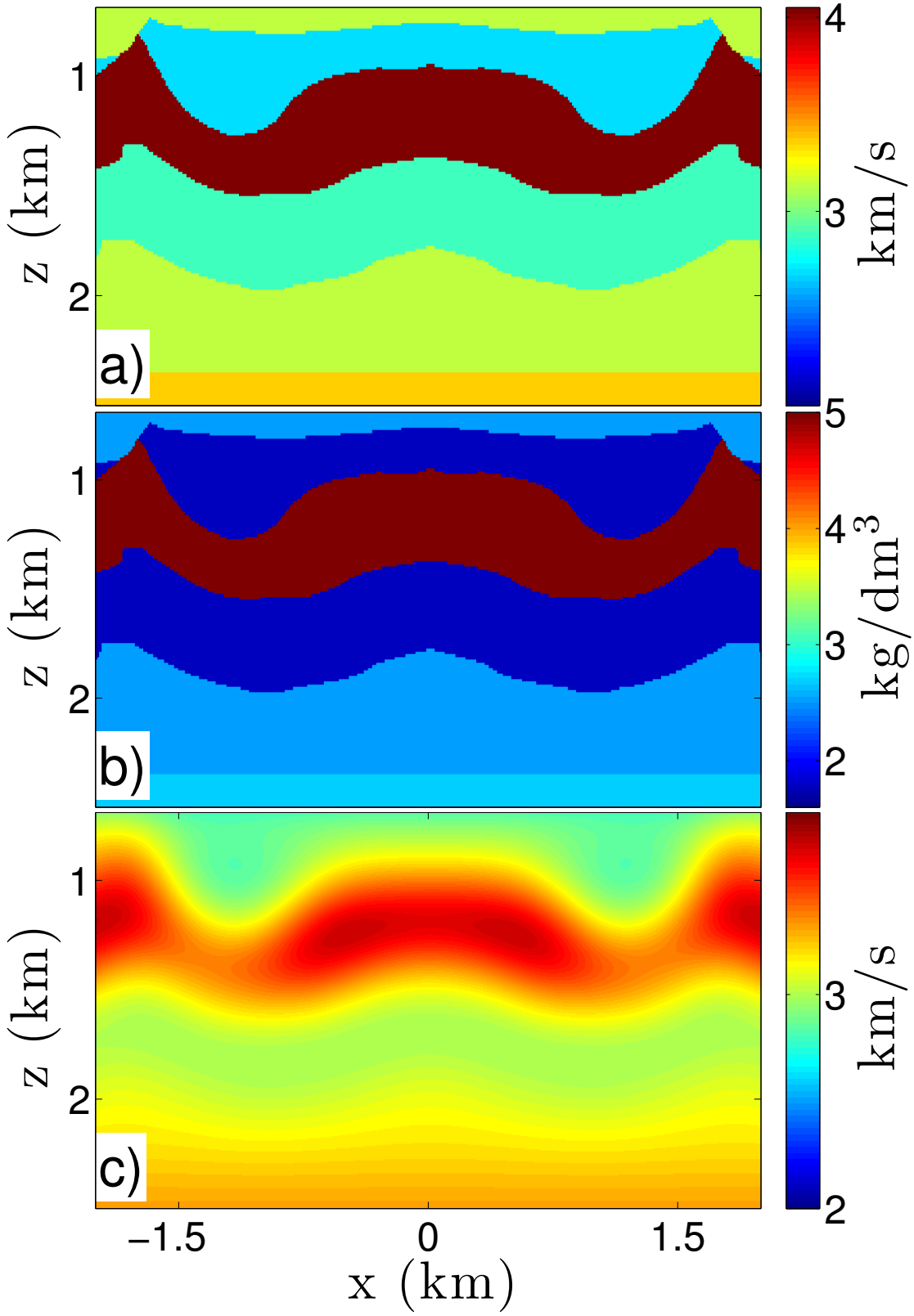

Figure 6.6: a) Velocity model. b) Density model. b) Smooth velocity model.

where $R(\mathbf{x}_r, \mathbf{x}, t)$ is the reflection response to downgoing waves at $z = z_i$ of the truncated medium below $z = z_i$, $\mathbf{x}_s$ is at $z = 0$, and $\mathbf{x}_r$ is at $z = z_i$. The truncated medium is equal to the true medium below the depth level $z = z_i$ and is homogeneous above $z = z_i$. The reflectivity $R(\mathbf{x}_r, \mathbf{x}, t)$ can be resolved from equation 6.11 by multidimensional deconvolution (MDD) (Wapenaar et al., 2011b). To achieve this result, we first correlate both sides of equation 6.11 with the downgoing Green's function and integrate over source locations over the acquisition surface:

$$C(\mathbf{x}_r, \mathbf{x}', t) = \int_{-\infty}^{\infty} [R(\mathbf{x}_r, \mathbf{x}, t) * \Gamma(\mathbf{x}, \mathbf{x}', t)]_{z=z_i} \, \mathrm{d}x, \quad \text{for } \mathbf{x}_r \text{ and } \mathbf{x}' \text{ at } z = z_i, \tag{6.12}$$

where C is the crosscorrelation function (as in the previous section, but with not-coinciding coordinates)

$$C(\mathbf{x}_r, \mathbf{x}', t) = \int_{-\infty}^{\infty} \left[G^-(\mathbf{x}_r, \mathbf{x}_s, t) * G^+(\mathbf{x}', \mathbf{x}_s, -t)\right]_{z_s=0} \mathrm{d}x_s, \tag{6.13}$$

and Γ is the point-spread function (van der Neut et al., 2011)

$$\Gamma(\mathbf{x}, \mathbf{x}', t) = \int_{-\infty}^{\infty} \left[G^+(\mathbf{x}, \mathbf{x}_s, t) * G^+(\mathbf{x}', \mathbf{x}_s, -t)\right]_{z_s=0} \mathrm{d}x_s. \tag{6.14}$$

We solve for $R(\mathbf{x}_r, \mathbf{x}, t)$ at different depth levels $z = z_i$ and many imaging points, as shown by the horizontal lines composed of black dots in Figure 6.5b, and evaluate the result at $t = 0$ and $x_r = x$. Figure 6.7c shows the final result of the imaging process. As in the previous image, the reflectors have been imaged at the correct spatial locations, but now the relative amplitudes between the different reflectors are better retrieved. Additionally, note how the lateral continuity of the deeper reflectors is well preserved in comparison with the prestack image in Figure 6.7a. The comparison between the amplitudes of the three images is shown in Figure 6.8, where we compare the reflectivity at $x = 200$ m retrieved by standard prestack migration, crosscorrelation, and multidimensional deconvolution with the true reflectivity. Multidimensional deconvolution acknowledges the multi-dimensional nature of the seismic wave field, hence the internal multiples contribute to the restoration of the amplitudes of the reflectors.

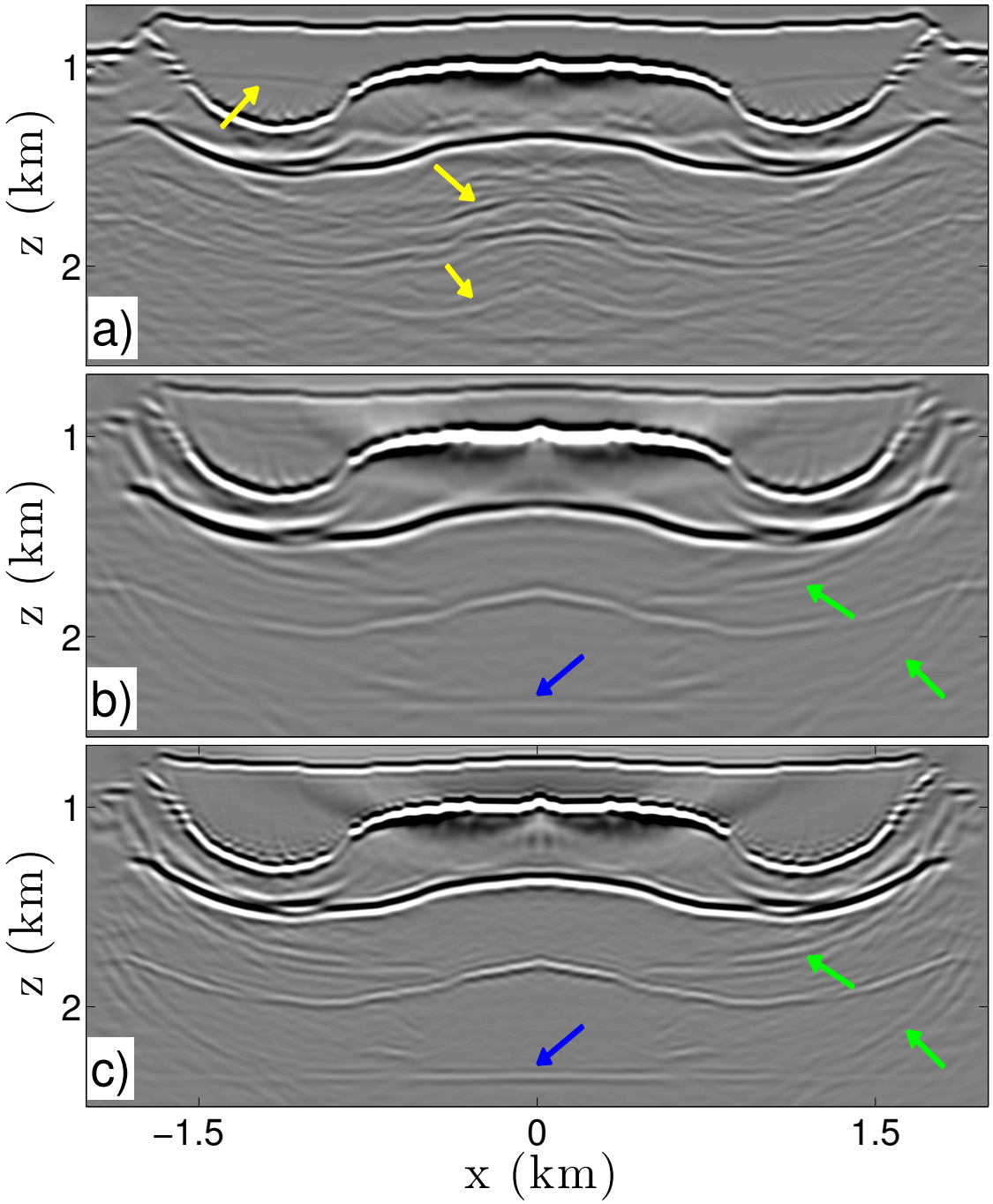

Figure 6.7: a) Image of the reflectors obtained with standard prestack migration. The yellow arrows indicate ghost images. b) Image of the reflectors obtained with the crosscorrelation function C. The green arrows indicate artifacts due to limited source aperture. The blue arrow indicates the flat reflector at $z = 2.3$ km. c) Image of the reflectors obtained with multidimensional deconvolution. The green arrows indicate artifacts due to limited source aperture. The blue arrow indicates the flat reflector at $z = 2.3$ km.

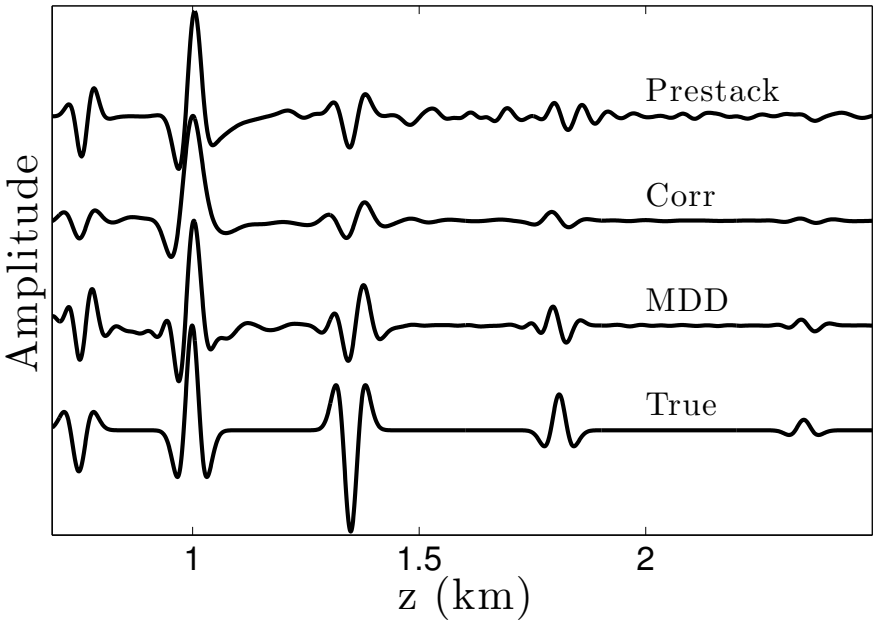

Figure 6.8: Comparison of the reflectivity at $x = 200$ m retrieved by standard prestack migration, crosscorrelation, and multidimensional deconvolution with the true reflectivity (from top to bottom).

6.5 Imaging with erroneous velocity

In this section, we demonstrate the robustness of the combination of autofocusing and multidimensional deconvolution when an erroneous velocity model is used to estimate the first-arriving waves (a required input for the autofocusing process). This experiment is carried out with a velocity error of +10% in the background velocity shown in Figure 6.6c and we compute a target-oriented image in a smaller portion of the model which is enclosed by the dashed rectangle in Figure 6.5a. We start by creating a reference image using one-way prestack migration. This reference image is shown in Figure 6.9a, where we have used the erroneous background velocity model in the prestack migration algorithm. As expected, the reflectors are now imaged at the wrong spatial location. In average, they have been shifted downward by ≈ 300 m. The yellow ellipses in Figure 6.9a indicate some of the pronounced artifacts, such as ghost reflectors, present in this standard image. The yellow arrow indicates a strong artifact due to limited source aperture.

Figure 6.9b shows the result of multidimensional deconvolution applied to the autofocused downgoing and upgoing wave fields. Similarly to the reference image, the reflectors have been reconstructed at the wrong spatial location, but now we obtain a superior image with fewer artifacts. Additionally, the image is less noisy and the flat reflector, indicated by the blue arrow in Figures 6.9b, is now visible. This flat reflector corresponds to the one indicated by the blue arrow in Figures 6.7b-c at $z = 2.3$ km. Note that the artifact indicated by the yellow arrow in 6.9b, is still present because it is due to limited source aperture and not to the multiply-scattered waves included in the data. This test shows that the image obtained by autofocusing (with an erroneous background model) still focuses the multiples along with the primaries, albeit at the wrong location.

6.6 Conclusions

We showed that our recently introduced method for data-driven Green's function retrieval (Wapenaar et al., 2013a, 2012a) allows us to construct an image that is not affected by ghost images of the reflectors. The retrieved downgoing and upgoing components of the Green's functions are the key components needed to obtain this result. These wave fields are then used to create different images of the medium with crosscorrelation and multidimensional deconvolution. The images created with crosscorrelation and multidimensional deconvolution show an improvement over standard imaging. Additionally, multidimensional deconvolution yields an image whose amplitudes better agree with the correct reflection responses. This is due to the deconvolution process that correctly handles the internal multiples and retrieves more correct amplitudes of the primary reflections. We emphasize that, for the crosscorrelation and multidimensional deconvolution results, the imaging process does not require any more knowledge of the medium parameters than standard primary imaging schemes (which use a macro model). Our method can be helpful in situations where waves have traversed a strongly inhomogeneous and scattering overburden, e.g., subsalt (Sava and Biondi, 2004) and near-surface imaging (Keho and Kelamis, 2012). Finally, the results in the last section of the paper showed that autofocusing is robust with respect to errors in the background model

used to estimate the first-arriving waves. The combination of autofocusing and multidimensional deconvolution still removes the artifacts due to the presence of multiply-scattered waves in the reflection data. This is a promising result towards future applications of the method on real data where we expect to have only estimates of the background velocity of the subsurface.

6.7 Acknowledgments

This work was supported by the sponsors of the Consortium Project on Seismic Inverse Methods for Complex Structures at the Center for Wave Phenomena and the Netherlands Research Centre for Integrated Solid Earth Science (ISES). The reproducible numeric examples in this paper use the Madagascar open-source software package freely available from http://www.ahay.org and the one-way prestack depth migration code freely available from http://janth.home.xs4all.nl.

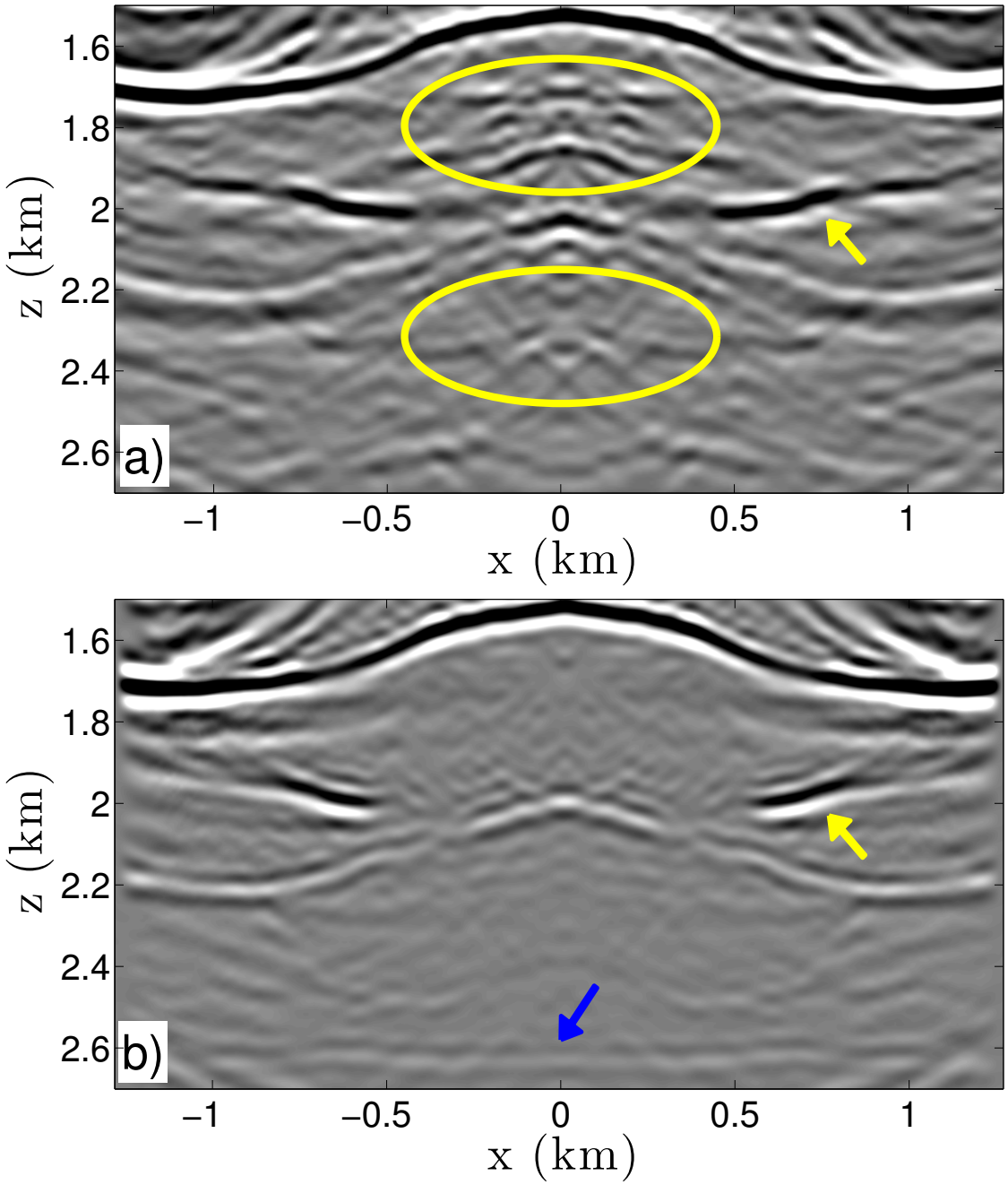

Figure 6.9: a) Image of the reflectors obtained with standard prestack migration using a background velocity with an error of +10%. The yellow ellipses indicate ghost images and artifacts. The yellow arrow indicates an artifact due to limited source aperture. b) Image of the reflectors obtained with multidimensional deconvolution. The first arriving waves (a required input for the autofocusing process) are computed using a background velocity with an error of +10%. The yellow arrow indicates an artifact due to limited source aperture. The blue arrow indicates the flat reflector.

CHAPTER 7

GENERAL CONCLUSIONS AND FUTURE RESEARCH

This chapter provides a brief and general conclusion to this dissertation and suggests recommendations for future research paths of the work exposed here. For specific conclusions related to the different Chapters, I ask the reader to refer to the individual conclusions in Chapters 2 through 6.

The most significant contribution of my thesis is the development of a new approach that allows one to retrieve the Green's wave field originating from a location (image point) inside the subsurface and recorded at the acquisition surface, and to decompose it in its downgoing and upgoing (one-way) components. This method requires as input the reflection response acquired at the surface and an estimate of the first-arriving wave traveling between the image point and the surface. Throughout this dissertation, I emphasize that, unlike in other Green's function retrieval methods, no physical receiver is needed at the position of the image point. The importance of retrieving the Green's functions is twofold. First, once the Green's functions are known, one can downward continue the wave field from the recording surface to the interior by virtue of the representation theorem (Aki and Richards, 2002). It is not necessary to use any modeling for this purpose because the Green's function *is* the two-way downward continuation operator. Second, since the proposed method provides the downgoing and upgoing Green's functions in the interior, one can immediately use these for imaging. This can be achieved either by crosscorrelating the downgoing and upgoing one-way Green's functions, or by multidimensional deconvolution (van der Neut et al., 2011). This dissertation emphasizes that imaging with multiply-scattered waves is a challenging task, and it proposes a new approach to solve some aspects of this problem.

Chapters 2 and 3 establish the link between inversion methods originally used in quantum scattering and Green's function retrieval for a one-dimensional medium. In these Chapters

I show that the importance of these inversion methods is linked to the retrieval of the wave field propagating in an unknown medium and not to the retrieval of the impedance profile of the same medium (Berryman and Greene, 1980; Newton, 1981) This insight proved to be fundamental in the development of this thesis. Chapter 4 utilizes the theoretical foundation for one-dimensional media, discussed in Chapters 2 and 3, and extends the novel method to two-dimensional inhomogeneous media. In Chapter 5, the unitarity of the scattering matrix plays an important role in exposing the consistency between the new approach (requiring data on only one side of the medium) and existing methods that require measurement on a closed boundary, such as seismic interferometry.

In a complicated subsurface, singly scattered waves can illuminate only a limited number of structures; hence techniques that remove multiple reflections from the data reduce the amount of information included in the recorded wave fields. The new approach uses the multiply scattered waves, such as internal multiples, because they provide additional illumination of the structures in the subsurface and, hence, increase the information available for interpretation (Malcolm et al., 2011). Chapter 6 demonstrates that the proposed approach shows an improvement over standard imaging because it provides images with more correct amplitudes and without ghost reflectors. Additionally, the new approach shows promising results when an erroneous velocity model is used to estimate the first-arriving waves.

I also note some potential research directions which will be pursued in future work. One of the most natural extensions is the modification of the iterative scheme to handle data including free-surface multiples. Preliminary results of synthetic examples prove that this research question can be potentially solved in the near future. Another important step is to extend the results exposed in this thesis to a wider class of physical phenomena, such as elastic or electromagnetic wave propagation. For example, extension to elastic waves has to deal with time windowing issues because reflected elastic waves contain both P- and S-waves. A key question that needs to be addressed concerns the analysis of wave propagation in media with intrinsic attenuation. An ansatz to this problem would be the application of

ad-hoc corrections to recorded traces between every iteration.

REFERENCES CITED

Agranovich, Z. S., and V. A. Marchenko, 1963, The Inverse Problem of Scattering Theory: Gordon and Breach.

Aki, K., and P. G. Richards, 2002, Quantitative seismology, 2nd ed.: University Science Books.

Aktosun, T., and J. H. Rose, 2002, Wave focusing on the line: Journal of Mathematical Physics, **43**, 3717–3745.

Amundsen, L., 2001, Elimination of freesurface related multiples without need of the source wavelet: Geophysics, **66**, 327–341.

Artman, B., I. Podladtchikov, and B. Witten, 2010, Source location using time-reverse imaging: Geophysical Prospecting, **58**, 861–873.

Bakulin, A., and R. Calvert, 2006, The virtual source method: Theory and case study: Geophysics, **71**, SI139–SI150.

Baysal, E., D. Kosloff, and J. Sherwood, 1983, Reverse time migration: Geophysics, **48**, 1514–1524.

Beresnev, I. A., and P. A. Johnson, 1994, Elastic-wave stimulation of oil production; a review of methods and results: Geophysics, **59**, 1000–1017.

Berkhout, A. J., 1979, Steep dip finite-difference migration: Geophysical Prospecting, **27**.

———, 1987, Applied seismic wave theory: Elsevier.

———, 1997, Pushing the limits of seismic imaging, Part I: Prestack migration in terms of double dynamic focusing: Geophysics, **62**, 937–954.

Berkhout, A. J., and D. J. Verschuur, 1997, Estimation of multiple scattering by iterative inversion, Part I: Theoretical considerations: Geophysics, **62**, 1586–1595.

Berryman, J., and R. Greene, 1980, Discrete inverse methods for elastic waves in layered media: Geophysics, **45**, 213–233.

Biondi, B., 2006, 3D Seismic Imaging: Society of Exploration Geophysicists.

Bleistein, N., J. Cohen, and J. Stockwell, 2001, Mathematics of Multidimensional Seismic Imaging, Migration, and Inversion: Springer.

Bleistein, N., and R. A. Handelsman, 1975, Asymptotic expansions of integrals: Dover Publications.

Born, M., and E. Wolf, 1999, Principles of optics: Cambridge University Press.

Brenders, A. J., and R. G. Pratt, 2007, Full waveform tomography for lithospheric imaging: results from a blind test in a realistic crustal model: Geophysical Journal International, **168**, 133–151.

Broggini, F., and R. Snieder, 2012, Connection of scattering principles: a visual and mathematical tour: European Journal of Physics, **33**, 593–613.

Broggini, F., R. Snieder, and K. Wapenaar, 2011, Connection of scattering principles: Focusing the wavefield without source or receiver: SEG Technical Program Expanded Abstracts, **757**, 3845–3850.

———, 2012a, Creating a virtual source inside a medium from reflection data: numerical examples for laterally-varying velocity models, spatially-extended virtual sources, and inaccurate direct arrivals: SEG Technical Program Expanded Abstracts, **710**, 1–5.

———, 2012b, Focusing the wavefield inside an unknown 1D medium - Beyond seismic interferometry: Geophysics, **77**, A25–A28.

Budreck, D. E., and J. H. Rose, 1990, Three-dimensional inverse scattering in anisotropic elastic media: Inverse Problems, **6**, 331–348.

———, 1991, Elastodynamic completeness relations for scattered wavefields: SIAM Journal of Applied Mathematics, **51**, 1568–1584.

———, 1992, A Newton-Marchenko equation and generalized optical theorem for elastodynamics: Journal of Mathematical Physics, **33**, 2903–2915.

Burridge, R., 1980, The Gelfand-Levitan, the Marchenko, and The Gopinath-Sondhi integral equations of Inverse Scattering theory, regarded in the context of inverse impulse-response problems: Wave Motion, **2**, 305–323.

Carney, P., J. Schotland, and E. Wolf, 2004, Generalized optical theorem for reflection, transmission, and extinction of power for scalar fields: Phys. Rev. E, **70**, 036611.

Chadan, K., and P. C. Sabatier, 1989, Inverse Problems in Quantum Scattering Theory, 2nd ed.: Springer.

Claerbout, J. F., 1985, Imaging the Earth's interior: Blackwell Scientific Publications.

Colton, D., and R. Kress, 1998, Inverse Acoustic and Electromagnetic Scattering Theory: Springer.

Curtis, A., P. Gerstoft, H. Sato, R. Snieder, and K. Wapenaar, 2006, Seismic interferometry—turning noise into signal: The Leading Edge, **25**, 1082–1092.

de Hoop, A. T., 1995, Handbook of radiation and scattering of waves: Academic Press.

Dorren, H. J. S., E. J. Muyzert, and R. Snieder, 1994, The stability of one-dimensional inverse scattering: Inverse Problems, **10**, 865–880.

Epstein, C. L., 2003, Mathematics of Medical Imaging: Prentice Hall.

Erdélyi, A., 1956, Asymptotic expansions: Dover Publications.

Etgen, J., S. H. Gray, and Y. Zhang, 2009, An overview of depth imaging in exploration geophysics: Geophysics, **74**, WCA5–WCA17.

Etgen, J., and C. Regone, 1998, Strike shooting, dip shooting, widepatch shooting - Does prestack depth migration care? A model study: SEG Technical Program Expanded Abstracts, 66–69.

Fokkema, J. T., and P. M. van den Berg, 1993, Seismic Applications of Acoustic Reciprocity: Elsevier.

Gazdag, J., and P. Sguazzero, 1984, Migration of seismic data by phase shift plus interpolation: Geophysics, **49**, 124–131.

Gladwell, G. M. L., 1993, Inverse Problems in Scattering: Kluwer Academic Publishing.

Haffinger, P., and D. J. Verschuur, 2012, Estimation and application of near-surface full waveform redatuming operators: Geophysical Prospecting, **60**, 270–280.

Heisenberg, W., 1943, Die "beobachtbaren Grössen" in der Theorie der Elementarteilchen. II: Z. Phys., **120**, 673–602.

Hovakimian, L., 2005, Optical theorem in N dimensions: Phys. Rev. A, **72**, 064701. (Notes).

Jakubowicz, H., 1998, Wave equation prediction and removal of interbed multiples: SEG Technical Program Expanded Abstracts, 1527–1530.

Keho, T. H., and P. G. Kelamis, 2012, Focus on land seismic technology: The near-surface challenge: The Leading Edge, **32**, 62–28.

Lamb, G. L., 1980, Elements of soliton theory: Wiley-Interscience.

Larose, E., O. Lobkis, and R. Weaver, 2006, Passive correlation imaging of a buried scatterer (L): Journal of the Acoustical Society of America, **119**, 3549–3552.

Lobkis, O., and R. Weaver, 2001, On the emergence of the Green's function in the correlations of a diffuse field: Journal of the Acoustical Society of America, **110**, 3011–3017.

Malcolm, A., M. D. Hoop, and B. Ursin, 2011, Recursive imaging with multiply scattered waves using partial image regularization: A North Sea case study: Geophysics, **76**, B33–B42.

Marston, P., 2001, Generalized optical theorem for scatterers having inversion symmetry: Applications to acoustic backscattering: The Journal of the Acoustical Society of America, **109**, 1291.

Newton, R. G., 1976, Optical theorem and beyond: American Journal of Physics, **44**, 639–642.

———, 1980, Inverse scattering. I. One dimension: Journal of Mathematical Physics, **21**, 493–505.

———, 1981, Inversion of reflection data for layered media a review of exact methods: Geophysical Journal of the Royal astronomical Society, **65**, 191–215.

Ohanian, H. C., and R. Ruffini, 1994, Gravitation and Spacetime, 2nd ed.: W. W. Norton & Company.

Oristaglio, M., 1989, An inverse scattering formula that uses all the data: Inverse Problems, **5**, 1097–1105.

Rodberg, L. S., and R. M. Thaler, 1967, Introduction to the Quantum Theory of Scattering: Academic Press.

Rose, J. H., 2001, "Single-sided" focusing of the time-dependent Schrödinger equation: Phys. Rev. A, **65**, 012707.

———, 2002a, Single-sided autofocusing of sound in layered materials: Inverse Problems, **18**, 1923–1934.

———, 2002b, Time Reversal, Focusing and Exact Inverse Scattering, *in* Imaging of Complex Media with Acoustic and Seismic Waves: Springer, 97–106.

Sava, P., and B. Biondi, 2004, Wave-equation migration velocity analysis - II: Subsalt imaging example: Geophysical Prospecting, **52**, 607–623.

Sava, P., and S. J. Hill, 2009, Overview and classification of wavefield seismic imaging methods: The Leading Edge, **28**, 170–183.

Schuster, G. T., 2009, Seismic Interferometry: Cambridge University Press.

Shull, P. J., 2002, Nondestructive evaluation: theory, techniques, and applications: CRC Press.

Snieder, R., 2004, A Guided Tour of Mathematical Methods for the Physical Sciences, 2nd ed.: Cambridge University Press.

Snieder, R., van K Wijk, M. Haney, and R. Calvert, 2008, Cancellation of spurious arrivals in Green's function extraction and the generalized optical theorem: Phys. Rev. E, **78**, 036606.

ten Kroode, F., 2002, Prediction of internal multiples: Wave Motion, **35**, 315 – 338.

Thorbecke, J., 1997, Common Focus Point Technology: PhD thesis, Technische Universiteit Delft.

Ursin, B., O. Pedersen, and B. Arntsen, 2012, Flux-normalized wavefield decomposition and migration of seismic data: Geophysics, **77**, S83–S92.

van der Neut, J., J. Thorbecke, K. Mehta, E. Slob, and K. Wapenaar, 2011, Controlled-source interferometric redatuming by crosscorrelation and multidimensional deconvolution in elastic media: Geophysics, **76**, SA63–SA76.

van Groenestijn, G. J. A., and D. J. Verschuur, 2009, Estimation of primaries and near-offset reconstruction by sparse inversion: Marine data applications: Geophysics, **74**, R119–R128.

Verschuur, D. J., A. J. Berkhout, and C. P. A. Wapenaar, 1992, Adaptive surface-related multiple elimination: Geophysics, **57**, 1166–1177.

Wapenaar, K., 1996, One-way representations of seismic data: Geophysical Journal International, **127**, 178–188.

Wapenaar, K., and A. J. Berkhout, 1989, Elastic wave field extrapolation: Redatuming of single- and multi-component seismic data: Elsevier.

———, 1993, Representations of seismic reflection data. Part I: state of affairs: Journal of Seismic Exploration, **2**, 123–131.

Wapenaar, K., F. Broggini, E. Slob, and R. Snieder, 2013a, Three-Dimensional Single-Sided Marchenko Inverse Scattering, Data-Driven Focusing, Green's Function Retrieval, and their Mutual Relations: Phys. Rev. Lett., **110**, 084301.

Wapenaar, K., F. Broggini, and R. Snieder, 2011a, A proposal for model-independent 3D wave field reconstruction from reflection data: SEG Technical Program Expanded Abstracts, **746**, 3788–3792.

———, 2012a, Creating a virtual source inside a medium from reflection data: heuristic derivation and stationary-phase analysis: Geophysical Journal International, **190**, 1020–1024.

Wapenaar, K., D. Draganov, R. Snieder, X. Campman, and A. Verdel, 2010, Tutorial on seismic interferometry: Part 1 - Basic principles and applications: Geophysics, **75**, 75A195–75A209.

Wapenaar, K., and J. Fokkema, 2006, Green's function representations for seismic interferometry: Geophysics, **71**, SI33–SI46.

Wapenaar, K., J. Fokkema, and R. Snieder, 2005, Retrieving the Green's function in an open system by cross correlation: A comparison of approaches (L): Journal of the Acoustical Society of America, **118**, 2783–2786.

Wapenaar, K., E. Slob, F. Broggini, R. Snieder, J. Thorbecke, and J. van der Neut, 2013b, Data-driven Green's function retrieval from reflection data: Theory and example: EAGE Expanded Abstracts.

Wapenaar, K., J. Thorbecke, and D. Draganov, 2004, Relations between reflection and transmission responses of three-dimensional inhomogeneous media: Geophysical Journal International, **156**, 179–194.

Wapenaar, K., J. Thorbecke, J. van der Neut, E. Slob, F. Broggini, J. Behura, and R. Snieder, 2012b, Integrated migration and internal multiple elimination: SEG Technical Program Expanded Abstracts 2012, **707**, 1–5.

Wapenaar, K., J. van der Neut, E. Ruigrok, D. Draganov, J. Hunziker, E. Slob, J. Thorbecke, and R. Snieder, 2011b, Seismic interferometry by crosscorrelation and by multi-dimensional deconvolution: a systematic comparison: Geophysical Journal International, **185**, 1335–1364.

Weaver, R., and O. Lobkis, 2001, Ultrasonics without a source: Thermal fluctuation correlations at mhz frequencies: Phys. Rev. Lett., **87**, 134301.

Weglein, A., F. Gasparotto, P. Carvalho, and R. Stolt, 1997, An inverse-scattering series method for attenuating multiples in seismic reflection data: Geophysics, **62**, 1975–1989.

APPENDIX A - DERIVATION OF EQUATION 2.11

Here, we derive equation 2.11, i.e., the representation theorem for the homogeneous Green's function. We start with the equations

$$\frac{d^2}{dx^2}G^+(x,x_B)+\frac{\omega^2}{c(x)^2}G^+(x,x_B)=-\delta(x-x_B) \tag{A.1}$$

and

$$\frac{d^2}{dx^2}G^-(x,x_A)+\frac{\omega^2}{c(x)^2}G^-(x,x_A)=-\delta(x-x_A), \tag{A.2}$$

where x_A, x_B, and x indicate a position between x_l and x_r in Figure 2.17. Next, we multiply equation A.1 by $G^-(x,x_A)$, and equation A.2 by $G^+(x,x_B)$; then we subtract the two results and integrate between x_l and x_r, yielding

$$\begin{aligned} &G^+(x_A,x_B)-G^-(x_B,x_A) \\ &\quad=\int_{x_l}^{x_r}dx\left[G^-(x,x_A)\frac{d^2}{dx^2}G^+(x,x_B)-G^+(x,x_B)\frac{d^2}{dx^2}G^-(x,x_A)\right]. \end{aligned} \tag{A.3}$$

The right-hand side of the last equation is an exact derivative:

$$\begin{aligned} &\int_{x_l}^{x_r}dx\left[G^-(x,x_A)\frac{d^2}{dx^2}G^+(x,x_B)-G^+(x,x_B)\frac{d^2}{dx^2}G^-(x,x_A)\right] \\ &\equiv\int_{x_l}^{x_r}dx\frac{d}{dx}\left[G^-(x,x_A)\frac{d}{dx}G^+(x,x_B)-G^+(x,x_B)\frac{d}{dx}G^-(x,x_A)\right]; \end{aligned} \tag{A.4}$$

hence we obtain the expression for G_h:

$$\begin{aligned} &G^+(x_A,x_B)-G^-(x_A,x_B) \\ &\quad=\sum_{x'=x_l,x_r}m\left[G^-(x',x_A)\frac{d}{dx}G^+(x,x_B)|_{x=x'}-G^+(x',x_B)\frac{d}{dx}G^-(x,x_A)|_{x=x'}\right] \end{aligned} \tag{A.5}$$

with

$$m=\begin{cases}-1 & \text{if } x'=x_l,\\ +1 & \text{if } x'=x_r,\end{cases} \tag{A.6}$$

where we have used the source-receiver reciprocity relation $G^{\pm}(x_A, x_B) = G^{\pm}(x_B, x_A)$ for the acoustic Green's function (Wapenaar and Fokkema, 2006).

APPENDIX B - DERIVATION OF THE NEWTON-MARCHENKO EQUATION

Inserting expression 2.15 into the left-hand side of equation 2.18, using the relation $u^+ = u_0 + u^+_{sc}$ in the right-hand side of 2.18, and then inserting 2.13 into the right-hand side, we get

$$\begin{aligned} & e^{+ik|x_A - x_B|} + \int dx'' G^+(x_A, x'') L^{'}(x'') e^{+ik|x'' - x_B|} \\ & + e^{-ik|x_A - x_B|} + \int dx'' G^-(x_A, x'') L^{'}(x'') e^{-ik|x'' - x_B|} \\ & \quad = u^-(+n, x_A) e^{-ikx_B} + u^+(+n, x_A) e^{+ikx_B} \\ & \quad + \frac{i}{2k} u^-(+n, x_A) \int dx'' e^{+ik|x_B - x''|} L^{'}(x'') u^+(-n, x'') \\ & \quad + \frac{i}{2k} u^-(-n, x_A) \int dx'' e^{+ik|x_B - x''|} L^{'}(x'') u^+(+n, x''). \end{aligned} \tag{B.1}$$

In this one-dimensional problem, we need to consider two different cases: 1) $x_B > x_A, x''$ and 2) $x_B < x_A, x''$. Without loss of generality, we choose $x_B > x_A, x''$, and hence obtain

$$\begin{aligned} & e^{+ikx_B} \left[e^{-ikx_A} + \int dx'' G^+(x_A, x'') L^{'}(x'') e^{-ikx''} \right] \\ & + e^{-ikx_B} \left[e^{ikx_A} + \int dx'' G^-(x_A, x'') L^{'}(x'') e^{+ikx''} \right] \\ & \quad = u^-(+1, x_A) e^{-ikx_B} + u^-(-1, x_A) e^{+ikx_B} \\ & \quad - \frac{i}{2k} u^-(+1, x_A) e^{+ikx_B} \int -dx'' e^{-ikx''} L^{'}(x'') u^+(-1, x'') \\ & \quad - \frac{i}{2k} u^-(-1, x_A) e^{+ikx_B} \int -dx'' e^{-ikx''} L^{'}(x'') u^+(+1, x''). \end{aligned} \tag{B.2}$$

The terms inside the brackets in the left-hand side correspond to $u^+(-1, x_A)$ and $u^-(+1, x_A)$, respectively; while the integrals in the right-hand side correspond to $f(+1, -1)$ and $f(+1, +1)$, respectively. We rewrite equation B.2 using 2.13, 2.14, and the relation $f(+n, +n') = f(-n', -n)$, to give

$$u^+(+1, x_A) - u^-(+1, x_A) = -\frac{i}{2k} \sum_{n=-1,1} u^-(n, x_A) f(n, x_B). \tag{B.3}$$

For the second case $x_B < x_A, x''$, the solution is

$$u^+(-1, x_A) - u^-(-1, x_A) = -\frac{i}{2k} \sum_{n=-1,1} u^-(n, x_A) f(n, -x_B). \tag{B.4}$$

APPENDIX C - GREEN'S FUNCTION RECONSTRUCTION AND THE OPTICAL THEOREM

In this appendix we derive the mathematics that shows the connection between the Green's function reconstruction equation and the optical theorem in one dimension. The expression for the Green's function reconstruction is

$$\frac{i}{2k}\left[G^{+}(x_A,x_B)-G^{-}(x_A,x_B)\right]=\sum_{x'=x_l,x_r}G^{+}(x_A,x')G^{-}(x_B,x'), \tag{C.1}$$

and the Green's function excited by a point source at x_s recorded at x_r is given by

$$G^{+}(x_r,x_s)=\underbrace{-\frac{i}{2k}e^{ik|x_s-x_r|}}_{Td}\underbrace{-\frac{i}{2k}e^{ik|x_s|}f(n,n')e^{ik|x_r|}}_{Ts}, \tag{C.2}$$

where $f(n,n')$ represents the scattering amplitude (Rodberg and Thaler, 1967), and n' and n represent the directions of the incident wave and the scattered wave, respectively. In the expression above, Td represents the wave traveling directly from the source to the receiver, and term Ts corresponds to the scattered wave that reaches the receivers after interacting with the scatterer. Considering the first configuration (Figure 2.19a), inserting equation C.2 into the right-hand side of equation C.1 we get

$$\begin{aligned}\sum_{x'=x_l,x_r}G^{+}(x_A,x')G^{-}(x_B,x')=\\ -\frac{i}{2k}\underbrace{\left[-\frac{i}{2k}e^{ik(x_B-x_A)}-\frac{i}{2k}e^{-ik(x_B+x_A)}f(-1,1)\right]}_{T1}\\ -\frac{i}{2k}\underbrace{\left[-\frac{i}{2k}e^{-ik(x_B-x_A)}-\frac{i}{2k}e^{ik(x_B+x_A)}f^{*}(-1,1)\right]}_{T2}\\ -\left(\frac{i}{2k}\right)\underbrace{\left(\frac{i}{2k}\right)e^{ik(x_B-x_A)}\left[\,f(-1,-1)+f^{*}(-1,-1)+|f(-1,-1)|^2+|f(-1,1)|^2\,\right]}_{T3}.\end{aligned} \tag{C.3}$$

The terms $T1$ and $T2$ correspond to $G^{+}(x_A, x_B)$ and $-G^{-}(x_A, x_B)$, respectively, while the term $T3$ represents the unphysical wave previously discussed in the Mathematical tour; hence, equation C.4 simplifies to

$$\begin{aligned}
&\sum_{x'=x_l,x_r} G^{+}(x_A, x')G^{-}(x_B, x') \qquad \text{(C.4)}\\
&\quad = \frac{i}{2k}\left[G(x_A, x_B) - G^{-}(x_A, x_B)\right]\\
&\quad - \left(\frac{i}{2k}\right)^2 e^{ik(x_B - x_A)}\left[\, f(-1,-1) + f^{*}(-1,-1) + |f(-1,-1)|^2 + |f(-1,1)|^2 \,\right].
\end{aligned}$$

For the right-end side of equation C.5 to be equal to the left-hand side of equation C.1, the expression between the square brackets in term $T3$ should vanish:

$$f(-1,-1) + f^{*}(-1,-1) = -|f(-1,-1)|^2 + |f(-1,1)|^2. \qquad \text{(C.5)}$$

Equation C.5 is the expression for the one-dimensional optical theorem (Hovakimian, 2005). The second configuration (Figure 2.19b) gives

$$\begin{aligned}
&\sum_{x'=x_l,x_r} G^{+}(x_A, x')G^{-}(x_B, x') \qquad \text{(C.6)}\\
&\quad = \frac{i}{2k}\left[G^{+}(x_A, x_B) - G^{-}(x_A, x_B)\right]\\
&\quad - \left(\frac{i}{2k}\right)^2 e^{ik(x_B + x_A)} \underbrace{\left[\, f(-1,1) + f^{*}(1,-1) + f(-1,-1)f^{*}(1,-1) + f(-1,1)f^{*}(1,1) \,\right]}_{T4}.
\end{aligned}$$

In this case, term $T4$ corresponds to the generalized optical theorem in one dimension (Hovakimian, 2005).

The connection between the Green's function reconstruction and the generalized optical theorem has not only a mathematical proof, but also a physical meaning. The cross-correlation of scattered waves in equation C.4 produces a *spurious* arrival (Snieder et al., 2008), i.e. an unphysical wave that is not predicted by the theory. In the first configuration shown in Figure 2.19a, such *spurious* arrival has the same arrival time as the direct wave, $t_B + t_A$, but its amplitude is not correct (see term $T3$ in equation C.4). In the second case

(Figure 2.19b), t_A and t_B correspond to the time that a wave takes to travel from the origin $x = 0$ to x_A and x_B, respectively. Here, the *spurious* arrival corresponds to a wave that arrives at time $t_B - t_A$ when no physical wave arrives; in fact it would arrive before the direct arrival at time $t_B + t_A$. But, since the ordinary and generalized optical theorem hold, the spurious arrival cancels in both cases.

APPENDIX D - STATIONARY-PHASE ANALYSIS

We use the method of stationary phase (Bleistein and Handelsman, 1975; Erdélyi, 1956) to evaluate equation 4.4, which is repeated here for convenience

$$p_0^-(\mathbf{x}_R,t) = \int_{-\infty}^{\infty} \left[R(\mathbf{x}_R,\mathbf{x},t) * p_0^+(\mathbf{x},t)\right]_{z=0} \mathrm{d}x, \tag{D.1}$$

with $z_R = 0$. In the frequency domain this equation reads

$$\hat{p}_0^-(\mathbf{x}_R,\omega) = \int_{-\infty}^{\infty} \left[\hat{R}(\mathbf{x}_R,\mathbf{x},\omega)\hat{p}_0^+(\mathbf{x},\omega)\right]_{z=0} \mathrm{d}x, \tag{D.2}$$

where the incident downgoing field $\hat{p}_0^+(\mathbf{x},\omega)$ is defined as $\hat{p}_0^+(\mathbf{x},\omega) = \{\hat{G}_0^d(\mathbf{x},\mathbf{x}_{VS},\omega)\hat{s}(\omega)\}^*$, with the superscript asterisk denoting complex conjugation. Using equation 4.1 and using the fact that $s(t)$ is symmetric, we have in the high-frequency regime

$$\hat{p}_0^+(\mathbf{x},\omega) = -j\omega \frac{\exp\{j(\omega|\mathbf{x}-\mathbf{x}_{VS}|/c + \mu\pi/4)\}}{\sqrt{8\pi|\omega||\mathbf{x}-\mathbf{x}_{VS}|/c}} \hat{s}(\omega), \tag{D.3}$$

with $\mu = \mathrm{sign}(\omega)$. For the reflection impulse response of the medium in Figure 4.1, we write

$$\hat{R}(\mathbf{x}_R,\mathbf{x},\omega) = \sum_{n=1}^{\infty} \hat{R}^{(n)}(\mathbf{x}_R,\mathbf{x},\omega), \tag{D.4}$$

where $\hat{R}^{(n)}$ represents the nth event of the reflection response. Using equation 4.3 we obtain the following high-frequency approximation

$$\hat{R}^{(n)}(\mathbf{x}_R,\mathbf{x},\omega) = \frac{A^{(n)} z_R^{(n)}}{|\mathbf{x}-\mathbf{x}_R^{(n)}|} \frac{j\omega}{c} \frac{\exp\{-j(\omega|\mathbf{x}-\mathbf{x}_R^{(n)}|/c + \mu\pi/4)\}}{\sqrt{2\pi|\omega||\mathbf{x}-\mathbf{x}_R^{(n)}|/c}}. \tag{D.5}$$

For $\hat{R}^{(1)}$, i.e. the primary response of the first reflector, $A^{(1)} = r_1$ and $\mathbf{x}_R^{(1)}$ is the mirror image of $\mathbf{x}_R$ with respect to the first reflector. For $\hat{R}^{(2)}$, the primary response of the second reflector, $A^{(2)} = \tau_1^- r_2 \tau_1^+$ and $\mathbf{x}_R^{(2)}$ is the mirror image of $\mathbf{x}_R$ in the second reflector. For $\hat{R}^{(3)}$, the first multiple, $A^{(3)} = -\tau_1^- r_2^2 r_1 \tau_1^+$ and $\mathbf{x}_R^{(3)}$ is the mirror image of $\mathbf{x}_R$ in the mirror image of the first reflector with respect to the second reflector, etc. For $\hat{R}^{(4)}$, the primary response of the third reflector, $A^{(4)} = \tau_1^- \tau_2^- r_3 \tau_2^+ \tau_1^+$ and $\mathbf{x}_R^{(4)}$ is the mirror image of $\mathbf{x}_R$ in the third

reflector.

First we consider the response of the first reflector. Figure D.1a shows a number of rays of $R^{(1)}(\mathbf{x}_R, \mathbf{x}, t)$, leaving different sources at the surface, reflecting at the first reflector, and arriving at one and the same receiver at $\mathbf{x}_R$. According to equation D.1, these reflection impulse responses are convolved with the initial incident field, of which the rays are also shown in Figure D.1a (these are the rays that converge at $\mathbf{x}_{VS}$). This convolution product is stationary for the source at $x_0^{(1)}$, where the rays of the incident field and of the reflection impulse response have the same direction. Figure D.1b shows a number of such stationary rays for different receiver positions. With simple geometrical arguments it follows that these rays cross each other at the mirror image of the virtual source with respect to the first reflector, i.e., at $\mathbf{x}_{VS}^{(1)} = (-196, 128)$. The traveltimes of the convolution product are given by the lengths of the rays from $\mathbf{x}_{VS}^{(1)}$ to the surface, divided by the velocity. Hence, it is as if the response of the first reflector to the initial incident field originates from a source at $\mathbf{x}_{VS}^{(1)}$ (this is confirmed below). Similarly, the response of the second reflector to the initial incident field apparently originates from a mirror image of the virtual source in the second reflector, i.e., at $\mathbf{x}_{VS}^{(2)} = (-84, 912)$. The multiple reflected responses to the initial incident field also apparently originate from mirror images of the virtual source, all located along the line $z = z_{VS} + x/a$, see Figure 4.1. For example, the first multiple apparently originates from $\mathbf{x}_{VS}^{(3)} = (28, 1696)$ (being the mirror image of $\mathbf{x}_{VS}$ in the mirror image of the first reflector with respect to the second reflector).

Equation D.2, with $\hat{p}_0^+(\mathbf{x}, \omega)$ and $\hat{R}(\mathbf{x}_R, \mathbf{x}, \omega)$ defined in equations D.3 $-$ D.5, can be written as

$$\hat{p}_0^-(\mathbf{x}_R, \omega) = \sum_{n=1}^{\infty} \mathcal{I}^{(n)}, \tag{D.6}$$

with

$$\mathcal{I}^{(n)} = \int_{-\infty}^{\infty} f(x) \exp\{jk\phi(x)\} \mathrm{d}x, \tag{D.7}$$

where $k = \omega/c$,

$$f(x) = \frac{|\omega| A^{(n)} z_R^{(n)} \hat{s}(\omega)}{4\pi l_{VS}^{1/2} \{l_R^{(n)}\}^{3/2}}, \quad \phi(x) = l_{VS} - l_R^{(n)}, \tag{D.8}$$

with

$$l_{VS}(x) = |\mathbf{x} - \mathbf{x}_{VS}| = \sqrt{(x - x_{VS})^2 + z_{VS}^2}, \tag{D.9}$$

$$l_R^{(n)}(x) = |\mathbf{x} - \mathbf{x}_R^{(n)}| = \sqrt{(x - x_R^{(n)})^2 + (z_R^{(n)})^2}. \tag{D.10}$$

According to the method of stationary phase (Bleistein and Handelsman, 1975; Erdélyi, 1956) we may approximate $\mathcal{I}^{(n)}$ for large $|k|$ by

$$\mathcal{I}^{(n)} \approx \sqrt{\frac{2\pi}{|k\phi''(x_0^{(n)})|}} f(x_0^{(n)}) \exp\{j(k\phi(x_0^{(n)}) + \mu\pi/4)\}, \tag{D.11}$$

where $x_0^{(n)}$ is the stationary point, i.e, $\phi'(x_0^{(n)}) = 0$. The derivatives of the phase are

$$\phi'(x) = \frac{x - x_{VS}}{l_{VS}} - \frac{x - x_R^{(n)}}{l_R^{(n)}}, \tag{D.12}$$

$$\phi''(x) = \frac{z_{VS}^2}{l_{VS}^3} - \frac{(z_R^{(n)})^2}{\{l_R^{(n)}\}^3}. \tag{D.13}$$

The point $x_0^{(1)}$ depicted in Figure D.1c obeys

$$\frac{x_0^{(1)} - x_{VS}}{z_{VS}} = \frac{x_0^{(1)} - x_R^{(1)}}{z_R^{(1)}}. \tag{D.14}$$

Generalized for $x_0^{(n)}$, this gives

$$x_0^{(n)} = \frac{x_{VS} z_R^{(n)} - x_R^{(n)} z_{VS}}{z_R^{(n)} - z_{VS}}. \tag{D.15}$$

Substituting this for x into equation D.12 gives $\phi'(x_0^{(n)}) = 0$, hence, $x_0^{(n)}$ is indeed the stationary point of $\phi(x)$. According to equations D.9 and D.10 we have

$$l_{VS}(x_0^{(n)}) = \frac{z_{VS}}{z_R^{(n)} - z_{VS}} |\mathbf{x}_R^{(n)} - \mathbf{x}_{VS}|, \tag{D.16}$$

$$l_R^{(n)}(x_0^{(n)}) = \frac{z_R^{(n)}}{z_R^{(n)} - z_{VS}} |\mathbf{x}_R^{(n)} - \mathbf{x}_{VS}|. \tag{D.17}$$

Above we defined $\mathbf{x}_{VS}^{(n)}$ as a mirror image of $\mathbf{x}_{VS}$, obtained in the same way as $\mathbf{x}_R^{(n)}$ is obtained by mirroring $\mathbf{x}_R$. This implies that

$$|\mathbf{x}_R^{(n)} - \mathbf{x}_{VS}| = |\mathbf{x}_R - \mathbf{x}_{VS}^{(n)}|. \tag{D.18}$$

This is illustrated for $n = 1$ in Figure D.1c. Hence, equation D.11 gives (for large $|k|$)

$$\mathcal{I}^{(n)} \approx j\omega A^{(n)} \frac{\exp\{-j(\omega|\mathbf{x}_R - \mathbf{x}_{VS}^{(n)}|/c + \mu\pi/4)\}}{\sqrt{8\pi|\omega||\mathbf{x}_R - \mathbf{x}_{VS}^{(n)}|/c}} \hat{s}(\omega). \tag{D.19}$$

Hence,

$$\hat{p}_0^-(\mathbf{x}_R, \omega) = \sum_{n=1}^{\infty} \mathcal{I}^{(n)} = \sum_{n=1}^{\infty} A^{(n)} \hat{G}_0^d(\mathbf{x}_R, \mathbf{x}_{VS}^{(n)}, \omega)\hat{s}(\omega), \tag{D.20}$$

with $\hat{G}_0^d(\mathbf{x}_R, \mathbf{x}_{VS}^{(n)}, \omega)$ as defined in equation 4.1, but with the source at $\mathbf{x}_{VS}^{(n)}$. In the time domain this becomes

$$p_0^-(\mathbf{x}_R, t) = \sum_{n=1}^{\infty} A^{(n)} G_0^d(\mathbf{x}_R, \mathbf{x}_{VS}^{(n)}, t) * s(t), \tag{D.21}$$

see Figure 4.4 for $t > 0$.

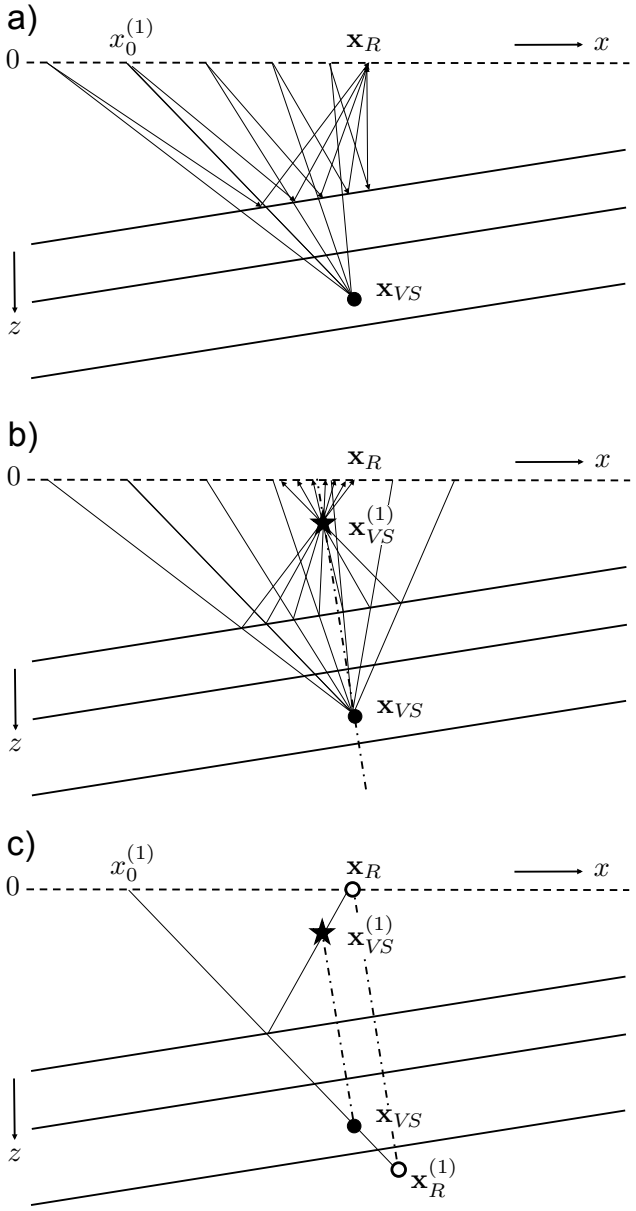

Figure D.1: Stationary-phase analysis of equation D.1. a) Analysis of the response of the first reflector for a fixed receiver at $\mathbf{x}_R$. The stationary point is denoted by $x_0^{(1)}$. b) Stationary rays, like the one in a), for different receivers. The response of the first reflector (indicated by the label B in Figure 4.4) seems to originate from $\mathbf{x}_{VS}^{(1)}$. c) Geometry underlying equations D.14 and D.18.

APPENDIX E - RELATIONSHIP BETWEEN PRESSURE-NORMALIZED REFLECTION AND TRANSMISSION RESPONSES

In this appendix, we derive a Green's function representation of the correlation-type for one-way (down- and up-going) fields and a relationship between pressure-normalized reflection and transmission responses measured on the top and bottom boundaries. We start from a two-way reciprocity theorem of the correlation-type:

$$\begin{aligned}\int_{\partial\mathbb{D}_0} \Big\{[G_3^{p,f}(\mathbf{x}_0,\mathbf{x}_0'',\omega)]^* G_3^{v,q}(\mathbf{x}_0,\mathbf{x}_0''',\omega) + [G_{3,3}^{v,f}(\mathbf{x}_0,\mathbf{x}_0'',\omega)]^* G^{p,q}(\mathbf{x}_0,\mathbf{x}_0''',\omega)\Big\}\,\mathrm{d}^2\mathbf{x}_0 \qquad \text{(E.1)}\\ = \int_{\partial\mathbb{D}_m} \Big\{[G_3^{p,f}(\mathbf{x}_m,\mathbf{x}_0'',\omega)]^* G_3^{v,q}(\mathbf{x}_m,\mathbf{x}_0''',\omega) + [G_{3,3}^{v,f}(\mathbf{x}_m,\mathbf{x}_0'',\omega)]^* G^{p,q}(\mathbf{x}_m,\mathbf{x}_0''',\omega)\Big\}\,\mathrm{d}^2\mathbf{x}_m,\end{aligned}$$

where the superscripts p and v characterize the Green's function as a pressure or velocity, respectively; and $\mathbf{x}_0'' = (\mathbf{x}_H'', x_{3,0} - \epsilon)$ and $\mathbf{x}_0''' = (\mathbf{x}_H''', x_{3,0} - \epsilon)$ with $\epsilon \to 0$. The superscripts q and f specify if the source is a point source of volume injection rate (monopole) or a point source of force (dipole), respectively. The subscript 3 indicates the vertical component of the velocity or the vertical component of the point source force. We then rewrite $G_{3,3}^{v,f}(\mathbf{x},\mathbf{x}_0'',\omega)$ as

$$G_{3,3}^{v,f}(\mathbf{x},\mathbf{x}_0'',\omega) = -\frac{1}{j\omega\rho(\mathbf{x})}\frac{\partial G_3^{p,f}(\mathbf{x},\mathbf{x}_0'',\omega)}{\partial x_3} + \frac{1}{j\omega\rho(\mathbf{x})}\delta(\mathbf{x}-\mathbf{x}_0''), \qquad \text{(E.2)}$$

and insert it into equation E.1 to obtain

$$\begin{aligned}\int_{\partial\mathbb{D}_0} \Bigg\{&[G_3^{p,f}(\mathbf{x}_0,\mathbf{x}_0'',\omega)]^* G_3^{v,q}(\mathbf{x}_0,\mathbf{x}_0''',\omega) \qquad \text{(E.3)}\\ &+\frac{1}{j\omega\rho(\mathbf{x}_0)}\left[\frac{\partial G_3^{p,f}(\mathbf{x}_0,\mathbf{x}_0'',\omega)}{\partial x_{3,0}}\right]^* G^{p,q}(\mathbf{x}_0,\mathbf{x}_0''',\omega)\Bigg\}\mathrm{d}^2\mathbf{x}_0\\ = \int_{\partial\mathbb{D}_m} \Bigg\{&[G_3^{p,f}(\mathbf{x}_m,\mathbf{x}_0'',\omega)]^* G_3^{v,q}(\mathbf{x}_m,\mathbf{x}_0''',\omega)\\ &+\frac{1}{j\omega\rho(\mathbf{x}_m)}\left[\frac{\partial G_3^{p,f}(\mathbf{x}_m,\mathbf{x}_0'',\omega)}{\partial x_{3,m}}\right]^* G^{p,q}(\mathbf{x}_m,\mathbf{x}_0''',\omega)\Bigg\}\mathrm{d}^2\mathbf{x}_m.\end{aligned}$$

Now, we focus on $\partial\mathbb{D}_0$ and the result for $\partial\mathbb{D}_m$ follows from a similar reasoning. The half-spaces above $\partial\mathbb{D}_0$ and below $\partial\mathbb{D}_m$ are homogeneous; hence the medium parameters at $\partial\mathbb{D}_0$ and $\partial\mathbb{D}_m$ are laterally invariant and we will use this property in the following. We define the two-dimensional spatial Fourier transform of a space-dependent function as $a(\chi,\mathbf{x}',\omega) = \int_{-\infty}^{+\infty}\int_{-\infty}^{+\infty} a(\mathbf{x},\mathbf{x}',\omega)\exp(k_1x_1)\exp(k_2x_2)\mathrm{d}x_1\mathrm{d}x_2$, where $\chi \equiv (k_1,k_2,x_3)$. To keep a simple notation, we use the same symbol for the space-dependent function and its spatial Fourier transform. We use $G = G^+ + G^-$ and apply Parseval's theorem (Wapenaar and Berkhout, 1989, equation B-27) to equation E.3, this gives

$$\left(\frac{1}{2\pi}\right)^2 \int_{\partial\mathbb{D}_0} \Big\{([G_3^{p,f+}(\chi_0,\mathbf{x}_0'',\omega)]^* + [G_3^{p,f-}(\chi_0,\mathbf{x}_0'',\omega)]^*)[G_3^{v,q+}(\chi_0,\mathbf{x}_0''',\omega) + G_3^{v,q-}(\chi_0,\mathbf{x}_0''',\omega)] \tag{E.4}$$
$$+\frac{1}{j\omega\rho(x_{3,0})}(jk_3[G_3^{p,f+}(\chi_0,\mathbf{x}_0'',\omega)]^* - jk_3[G_3^{p,f-}(\chi_0,\mathbf{x}_0'',\omega)]^*)[G^{p,q+}(\chi_0,\mathbf{x}_0''',\omega) + G^{p,q-}(\chi_0,\mathbf{x}_0''',\omega)]\Big\}\,\mathrm{d}^2\chi_0,$$

where $\chi_0 \equiv (k_1,k_2,x_3)$, $k_3 = \sqrt{k^2-k_1^2-k_2^2}$, $k = \dfrac{\omega}{c(x_{3,0})}$, and $\left(\frac{\partial G^\pm}{\partial x_3}\right)^* = \pm jk_3(G^\pm)^*$ (Wapenaar and Berkhout, 1989, equation B-29c). Additionally, we assume that k_3 is real-valued and ignore the evanescent waves. We reorder the terms in expression E.4 and obtain

$$\left(\frac{1}{2\pi}\right)^2 \int_{\partial\mathbb{D}_0} \Big\{([G_3^{p,f+}(\chi_0,\mathbf{x}_0'',\omega)]^* + [G_3^{p,f-}(\chi_0,\mathbf{x}_0'',\omega)]^*)[G_3^{v,q+}(\chi_0,\mathbf{x}_0''',\omega) + G_3^{v,q-}(\chi_0,\mathbf{x}_0''',\omega)] \tag{E.5}$$
$$+([G_3^{p,f+}(\chi_0,\mathbf{x}_0'',\omega)]^* - [G_3^{p,f-}(\chi_0,\mathbf{x}_0'',\omega)]^*)\frac{1}{j\omega\rho(x_{3,0})}[jk_3G^{p,q+}(\chi_0,\mathbf{x}_0''',\omega) + jk_3G^{p,q-}(\chi_0,\mathbf{x}_0''',\omega)]\Big\}\,\mathrm{d}^2\chi_0.$$

Then, we use $\mp jk_3(G^\pm)^* = \frac{\partial G^\pm}{\partial x_3}$ (Wapenaar and Berkhout, 1989, equation B-29b) and apply Parsevel's theorem to expression E.5, yielding

$$\int_{\partial\mathbb{D}_0} \Big\{([G_3^{p,f+}(\mathbf{x}_0,\mathbf{x}_0'',\omega)]^* + [G_3^{p,f-}(\mathbf{x}_0,\mathbf{x}_0'',\omega)]^*)[G_3^{v,q+}(\mathbf{x}_0,\mathbf{x}_0''',\omega) + G_3^{v,q-}(\mathbf{x}_0,\mathbf{x}_0''',\omega)] \tag{E.6}$$
$$+([G_3^{p,f+}(\mathbf{x}_0,\mathbf{x}_0'',\omega)]^* - [G_3^{p,f-}(\mathbf{x}_0,\mathbf{x}_0'',\omega)]^*)\frac{1}{j\omega\rho(\mathbf{x}_0)}[-\frac{\partial G^{p,q+}(\mathbf{x}_0,\mathbf{x}_0''',\omega)}{\partial x_{3,0}} + \frac{\partial G^{p,q-}(\mathbf{x}_0,\mathbf{x}_0''',\omega)}{\partial x_{3,0}}]\Big\}\,\mathrm{d}^2\mathbf{x}_0.$$

Using the relation

$$G_3^{v,q}(\mathbf{x},\mathbf{x}_0''',\omega) = -\frac{1}{j\omega\rho(\mathbf{x})}\frac{\partial G^{p,q}(\mathbf{x},\mathbf{x}_0''',\omega)}{\partial x_3}, \tag{E.7}$$

we rewrite expression E.6 as

$$\int_{\partial\mathbb{D}_0} \Big\{([G_3^{p,f+}(\mathbf{x}_0,\mathbf{x}_0'',\omega)]^* + [G_3^{p,f-}(\mathbf{x}_0,\mathbf{x}_0'',\omega)]^*)[G_3^{v,q+}(\mathbf{x}_0,\mathbf{x}_0''',\omega) + G_3^{v,q-}(\mathbf{x}_0,\mathbf{x}_0''',\omega)] \tag{E.8}$$
$$+([G_3^{p,f+}(\mathbf{x}_0,\mathbf{x}_0'',\omega)]^* - [G_3^{p,f-}(\mathbf{x}_0,\mathbf{x}_0'',\omega)]^*)[G_3^{v,q+}(\mathbf{x}_0,\mathbf{x}_0''',\omega) - G_3^{v,q-}(\mathbf{x}_0,\mathbf{x}_0''',\omega)]\Big\}\,\mathrm{d}^2\mathbf{x}_0.$$

In expression E.8, the terms containing Green's functions propagating in the same directions (e.g. $[G_3^{p,f+}]^* G_3^{v,q-}$) cancel; hence we obtain

$$2\int_{\partial\mathbb{D}_0}\Big\{[G_3^{p,f+}(\mathbf{x}_0,\mathbf{x}_0'',\omega)]^* G_3^{v,q+}(\mathbf{x}_0,\mathbf{x}_0''',\omega)+[G_3^{p,f-}(\mathbf{x}_0,\mathbf{x}_0'',\omega)]^* G_3^{v,q-}(\mathbf{x}_0,\mathbf{x}_0''',\omega)\Big\}\,\mathrm{d}^2\mathbf{x}_0 \quad \text{(E.9)}$$
$$=2\int_{\partial\mathbb{D}_m}\Big\{[G_3^{p,f+}(\mathbf{x}_m,\mathbf{x}_0'',\omega)]^* G_3^{v,q+}(\mathbf{x}_m,\mathbf{x}_0''',\omega)+[G_3^{p,f-}(\mathbf{x}_m,\mathbf{x}_0'',\omega)]^* G_3^{v,q-}(\mathbf{x}_m,\mathbf{x}_0''',\omega)\Big\}\,\mathrm{d}^2\mathbf{x}_m,$$

where we assumed that the evanescent waves can be neglected. This is a one-way reciprocity theorem of the correlation-type.

We define two acoustic states that will be used in the one-way reciprocity theorem, defined by equation E.9, to derive a relationship between the pressure-normalized reflection and transmission responses measured on $\partial\mathbb{D}_0$ and $\partial\mathbb{D}_m$. Both states are defined in the actual medium between the boundaries $\partial\mathbb{D}_0$ and $\partial\mathbb{D}_m$, as in Figure 5.1. We choose an impulsive point source of volume injection rate at $\mathbf{x}_0'''$, just above $\partial\mathbb{D}_0$, and define state A1 as

$$\mathbf{x}\in\partial\mathbb{D}_0=\begin{cases}2G_3^{v,q+}(\mathbf{x}_0,\mathbf{x}_0''',\omega)=\delta(\mathbf{x}_H-\mathbf{x}_H'''),\\ 2G_3^{v,q-}(\mathbf{x}_0,\mathbf{x}_0''',\omega)=-R(\mathbf{x}_0''',\mathbf{x}_0,\omega),\end{cases} \quad \text{(E.10)}$$

$$\mathbf{x}\in\partial\mathbb{D}_m=\begin{cases}2G_3^{v,q+}(\mathbf{x}_m,\mathbf{x}_0''',\omega)=T(\mathbf{x}_0''',\mathbf{x}_m,\omega),\\ 2G_3^{v,q-}(\mathbf{x}_m,\mathbf{x}_0''',\omega)=0.\end{cases} \quad \text{(E.11)}$$

For state B1, we choose a point source of force at $\mathbf{x}_0''$, just above $\partial\mathbb{D}_0$:

$$\mathbf{x}\in\partial\mathbb{D}_0=\begin{cases}2G_3^{p,f+}(\mathbf{x}_0,\mathbf{x}_0'',\omega)=\delta(\mathbf{x}_H-\mathbf{x}_H''),\\ 2G_3^{p,f-}(\mathbf{x}_0,\mathbf{x}_0'',\omega)=R(\mathbf{x}_0,\mathbf{x}_0'',\omega),\end{cases} \quad \text{(E.12)}$$

$$\mathbf{x}\in\partial\mathbb{D}_m=\begin{cases}2G_3^{p,f+}(\mathbf{x}_m,\mathbf{x}_0'',\omega)=T(\mathbf{x}_m,\mathbf{x}_0'',\omega),\\ 2G_3^{p,f-}(\mathbf{x}_0,\mathbf{x}_0'',\omega)=0.\end{cases} \quad \text{(E.13)}$$

Now, we plug the expressions of states A1 and B1 into equation E.9 and obtain

$$\int_{\partial\mathbb{D}_m}[T(\mathbf{x}_m,\mathbf{x}_0'',\omega)]^* T(\mathbf{x}_0''',\mathbf{x}_m,\omega)\mathrm{d}^2\mathbf{x}_m \quad \text{(E.14)}$$
$$=\delta(\mathbf{x}_H''-\mathbf{x}_H'')-\int_{\partial\mathbb{D}_0}[R(\mathbf{x}_0,\mathbf{x}_0'',\omega)]^* R(\mathbf{x}_0''',\mathbf{x}_0,\omega)\mathrm{d}^2\mathbf{x}_0. \quad \text{(E.15)}$$

This is the pressure-normalized version of equation (20) in Wapenaar et al. (2004).